Time domain Astronomy at Low Radio Frequencies (< 100 MHz): Instrumentation and Observations

(Corrected Copy)

A Thesis
Submitted for the Degree of
Doctor of Philosophy (Technology)

Submitted by
BANE KSHITIJ SUHAS TRUPTI

Department of Applied Optics & Photonics
University of Calcutta

2024

To my parents

Abstract

Exploration of the transient Universe is an exciting and fast-emerging area within radio astronomy. Radio transient sources can be defined as a class of objects that emit radio waves in the form of bursts, flares, or pulses from short durations (less than a few seconds) to long durations (greater than a few seconds). These include Pulsars, FRBs, GRBs, Flaring Stars, Sun, etc. Transient phenomena are likely locations of explosive or dynamic events, and they offer tremendous potential to uncover new physics and astrophysics. In addition, short-duration transients are powerful probes of intervening media owing to dispersion, scattering, and Faraday rotation that modify the signals. However, observations of such transients at low radio frequencies is largely uncharted territory due to various practical limitations.

A pulsar is a highly magnetized, rapidly rotating neutron star emitting electromagnetic radiation beams. Weighing more than our Sun, yet only about 20 km in diameter, these incredibly dense objects produce radio beams that sweep the sky like a lighthouse. They are detectable at radio frequencies through the beam of coherent radio emission from their magnetosphere whenever they intersect our line of sight. The first pulsar was observed at a low frequency of $\sim$ 81.5 MHz. However, much of our present knowledge about pulsars has come primarily from radio observations at frequencies $>$300 MHz. The primary reasons for this are: the emission from pulsars at low frequencies is more affected by dispersion and scattering during their propagation through the interstellar medium (ISM) as compared with higher frequencies, the comparatively intense synchrotron emission from the Galactic background and the Radio Frequency Interference (RFI).

Pulsar observations at frequencies $\leq$100 MHz are necessary for understanding the emission mechanism and characteristics of the pulse profile as a function of frequency, which are still being examined. For example, many pulsars exhibit a turnover in the spectrum close to 100 MHz. Therefore, extending their spectra toward lower radio frequencies is of great interest. Low-frequency observations can also help in studying the ISM as the propagation effects of ISM are more prominent at low radio frequencies. Fast Radio Bursts (FRBs) are still eluding astronomers about their origin. Recently, FRBs have been detected at 120 MHz and 111 MHz. This suggests that detecting them at even lower frequencies might be possible. For this, continuous monitoring of the sky at low frequencies is essential.

Considering this, we have set up a radio telescope in the Gauribidanur Observatory (named as GAuribidanur Pulsar System- GAPS) for dedicated observations of pulsars and other astrophysical transients in the frequency range of 50 to 80 MHz. Its purpose is to observe and understand the characteristics of known pulsars and potentially search for FRBs at these frequencies if they should occur. This observing facility is a dedicated instrument with wide sky coverage, large bandwidth, and high time resolution, which are important for observing fast transients. The thesis involved developing the prototype system and its subsequent upgrades, testing and characterizing the system, and observing targeted Pulsars.

Contents

List of Publications

Refereed Journal Articles

1. *Prototype for pulsar observations at low radio frequencies using log-periodic dipole antennas*
   Kshitij S. Bane, Indrajit V. Barve, G. V. S. Gireesh, C. Kathiravan, R. Ramesh, J. Astron. Telesc. Instrum. Syst. 8(1) 017001 (2022)
   `https://doi.org/10.1117/1.JATIS.8.1.017001`

2. *Initial results from multi-beam observations of pulsars and solar transient with the digital beamformer for the Gauribidanur pulsar system*
   Kshitij S. Bane, Indrajit V. Barve, G. V. S. Gireesh, C. Kathiravan, R. Ramesh, J. Astron. Telesc. Instrum. Syst. 10(1) 014001 (2023)
   `https://doi.org/10.1117/1.JATIS.10.1.014001`

3. *1-bit raw voltage recording system for dedicated observations of transients at low radio frequencies*
   Kshitij S. Bane, Indrajit V. Barve, G. V. S. Gireesh, C. Kathiravan, R. Ramesh, The Astrophysical Journal Supplement Series, 272, 27 (2024)
   `https://iopscience.iop.org/article/10.3847/1538-4365/ad4296`

Conference proceedings

1. *A High Spectral and Temporal Resolution ROACH-based Digital Back-end for Low Radio Frequency Spectro-Polarimetry*
   URSI Asia-Pacific Radio Science Conference (AP-RASC), March 2019.
   doi: `10.23919/URSIAP-RASC.2019.8738638`
   `https://ieeexplore.ieee.org/document/8738638`

2. *Instrumentation for observations of Pulsars at Low Radio Frequencies*
   38th Meeting of The Astronomical Society of India, February 2020.
   doi: `10.13140/RG.2.2.16075.13607`
   `https://www.researchgate.net/publication/341071185_Instrumentation_for_observations_of_Pulsars_at_Low_Radio_Frequencies`

3. *A new facility for Pulsar observations at low radio frequencies*
   40th Meeting of The Astronomical Society of India, March 2022.
   doi: `10.13140/RG.2.2.31069.08162`
   `https://www.researchgate.net/publication/360699527_A_new_facility_for_Pulsar_observations_at_low_radio_frequencies`

4. *Gauribidanur Pulsar System*
   URSI Regional Conference on Radio Science (URSI-RCRS), December 2022.
   doi: `10.23919/URSI-RCRS56822.2022.10118458`
   `https://ieeexplore.ieee.org/document/10118458`

5. *Gauribidanur Pulsar System: A prototype software-based binary radio telescope for transient surveys*
   4th URSI Atlantic Radio Science Conference (AT-RASC), May 2024.
   doi: `10.46620/URSIATRASC24/OPXN3842`
   `https://www.researchgate.net/publication/381902612_Gauribidanur_Pulsar_System_A_prototype_software-based_binary_radio_telescope_for_transient_surveys`

6. *Observing Pulsars and Transients at Low Radio frequencies using 1-bit digitization*
   6th URSI Regional Conference on Radio Science (URSI-RCRS), Bhimtal, October 2024
   doi: `10.46620/URSI_RSRC24/0665QRI6714`
   `https://www.researchgate.net/publication/387305635_Observing_Pulsars_and_Transients_at_Low_Radio_frequencies_using_1-bit_digitization`

Presentations

Oral

1. *Development of radio antenna array and receiver system for observations of Pulsars at Low Radio Frequencies* at Young Astronomers' Meet, Kodaikanal Solar Observatory, September 2019.

2. *A new instrument for observations of Transients at Low Radio frequencies at Gauribidanur observatory- Initial results and future possibilities* at In-house meeting, Indian Institute of Astrophysics, Bangalore, June 2021.

3. *Gauribidanur Pulsar System* at Aus-NZ Orange Pulsar meeting, November 2022 (Online).

4. *Gauribidanur Pulsar System* at the URSI Regional Conference on Radio Science (URSI-RCRS), IIT Indore, December 2022.

5. *Gauribidanur Pulsar System* at BGS Student Seminar, Indian Institute of Astrophysics, Bangalore, January 2023.

6. *Multi-beam observations with the GAuribidanur Pulsar System (GAPS)* at the 42nd Meeting of The Astronomical Society of India, IISc Bangalore, February 2024.

7. *The GAuribidanur Pulsar System (GAPS)* at Young Astronomers' Meet, CHRIST (Deemed to be University), Bangalore, March 2024.

8. *Gauribidanur Pulsar System: A prototype software-based binary radio telescope for transient surveys* at the 4th URSI Atlantic Radio Science Meeting (AT-RASC), Gran Canaria, May 2024.

9. *Observing Pulsars and Transients at Low Radio frequencies using 1-bit digitization* at the 6th URSI Regional Conference on Radio Science (URSI-RCRS), Bhimtal, October 2024.
   (Young Scientist Award)

Posters

1. *Instrumentation for observations of Pulsars at Low Radio Frequencies* at the 38th Meeting of The Astronomical Society of India, IISER Tirupati, February 2020.

2. *A new facility for Pulsar observations at low radio frequencies* at the 340th Meeting of The Astronomical Society of India, IIT Roorkee, March 2022.
   (Best poster award in Instrumentation category)

3. *Gauribidanur Pulsar System* at Young Astronomers' Meet, ARIES, Nainital, November 2022 (Online).

List of Figures

List of Tables

Chapter 1

Introduction

1.1 Pulsars

Pulsars - one of the most fascinating objects in the Universe. They are incredibly dense, highly magnetized, immensely energetic, rapidly rotating Neutron stars. They beam radiation along their magnetic axis that sweeps the sky like a lighthouse and are detectable through radio pulses whenever the beams cross our line of sight. The first pulsar was detected in 1967 by Jocelyn Bell and Antony Hewsih (Hewish *et al.*, 1968). Since their discovery, about 3000 pulsars have been discovered in our Galaxy. With densities of $\sim 10^{14}$ g cm^{-3} and magnetic field strengths of $\sim 10^{14}$ to $\sim 10^{15}$ gauss, they are the laboratories of extreme physical conditions. Pulsars provide a wealth of information about neutron star physics, general relativity, gravitational waves, galactic gravitational potential and magnetic field, interstellar medium, celestial mechanics, planetary physics, and even cosmology (Lorimer and Kramer, 2004).

Figure 1.1 shows a basic model of a pulsar as a rotating, magnetized neutron star. The rotational and magnetic axes are not aligned. The coherent emission mechanism produces radio frequency radiation that comes out in two beams, one from each pole of the magnetosphere. We see these rotating radiation beams whenever they intersect our line of sight with the pulsar, much like a lighthouse on the seashore.

1.1.1 Pulsar observational properties

1.1.1.1 Period

The time interval between consecutive pulses is called the pulsar's Period. From the first pulsar detection itself, it was noticed that pulsar periods are extremely regular. Though rotational periods of individual pulsars are astonishingly stable, the periods vary from a few milliseconds to seconds for different pulsars. The fastest rotating pulsar is PSR J1748-2446ad with a period of 1.4 ms (Hessels *et al.*, 2006), and the slowest one is PSR J0250+5854 with a period of 23.5 s (Tan *et al.*, 2018).

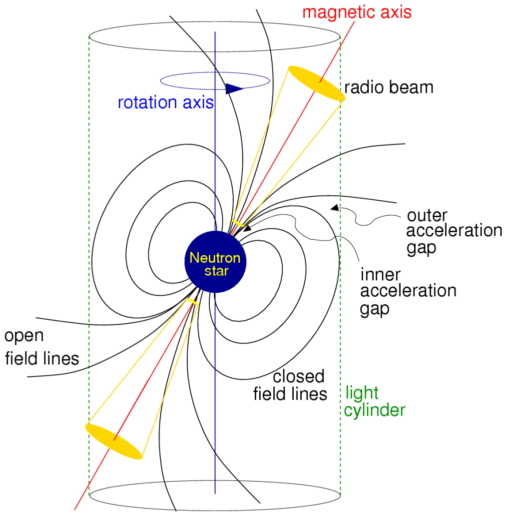

Figure 1.1: Basic pulsar model (Credits: NRAO)

The radio emission from a pulsar causes a small loss in its rotational kinetic energy, resulting in a decrease in its rate of rotation or an increase in the period over time. So, apart from the spin period (P), the period derivative or the spin-down rate ($\dot{P}$) is also an important observational property of pulsars. For typical pulsars, the value of $\dot{P}$ is of the order of $10^{-15}\,\mathrm{s/s}$. On the basis of P and $\dot{P}$, pulsars are generally classified into two categories: normal pulsars ($P > 30\,\mathrm{ms}$ and $\dot{P} \sim 10^{-15}\,\mathrm{s/s}$) and millisecond pulsars ($P < 30\,\mathrm{ms}$ and $\dot{P} \sim 10^{-20}\,\mathrm{s/s}$).

Figure 1.2 shows the famous P-$\dot{P}$ diagram. The diagram is generated using `ppdot_plane_plot.py` script from PRESTO[*]. It shows the known pulsar population according to their spin period and spin-down rate. Much like the Hertzsprung–Russell diagram that tracks the evolution of stars, P-$\dot{P}$ diagram shows the lives of pulsars. Around the center of the plot, we see a big cluster of normal pulsars, while the millisecond pulsars (MSPs) are at the bottom left corner. The diagram also encodes various pulsar properties that depend on observed P and $\dot{P}$: Characteristic age ($\tau \propto P/\dot{P}$), the magnetic field strength ($B \propto \sqrt{P\dot{P}}$), and the spin-down luminosity ($\dot{E} \propto \dot{P}/P^3$) indicated by the contour lines in the diagram. Young pulsars, often associated with supernova remnants (SNRs), start at the upper region of the diagram. As they evolve, they spin down until their rotation rate is too slow to power the radio emission mechanism and become too faint to be detected. The region towards the bottom right of the plot is called the "Death Valley," where no pulsar is seen. MSPs are usually old pulsars with lower magnetic field strength than normal ones and very rapid spin periods. They evolve from binary systems as they are recycled by the mass transfer

---

[*] https://github.com/scottransom/presto

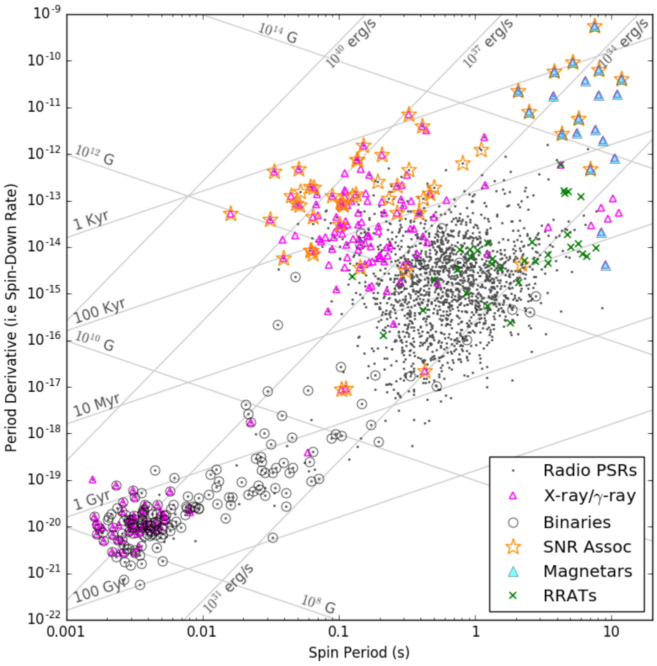

Figure 1.2: P-$\dot{P}$ diagram

from their companion stars. There are some other interesting groups of objects in the diagram, like Magnetars, which have tremendous magnetic fields, and RRATs (Rotating Radio Transients), which emit transient pulses instead of continuous pulse trains.

1.1.1.2 Integrated pulse profile

When hundreds or thousands of pulses from a pulsar are added together, we obtain something called the 'Integrated pulse profile.' The individual pulses vary in intensity and shape, but the integrated profiles are stable for a given pulsar. The integrated pulse profile is a unique feature of a pulsar and can be thought of as a "fingerprint" of the pulsar, giving information about the emission beam geometry, viewing angle, etc.

Figure 1.3 shows integrated profiles of a sample of 12 pulsars at 1.4 GHz. It can be seen that these integrated profiles show a wide variety of shapes, from simple profiles with single components to complex profiles with multiple components. The duty cycles are usually of the order of a few percent. Some pulsars exhibit an interesting phenomenon called 'Mode changing' where the pulsar has more than one stable pulse profile and abruptly shifts between these profiles (Hankins and Rickett, 1975). Some pulsars also show 'Nulling' where no emission is detected during some interval from the

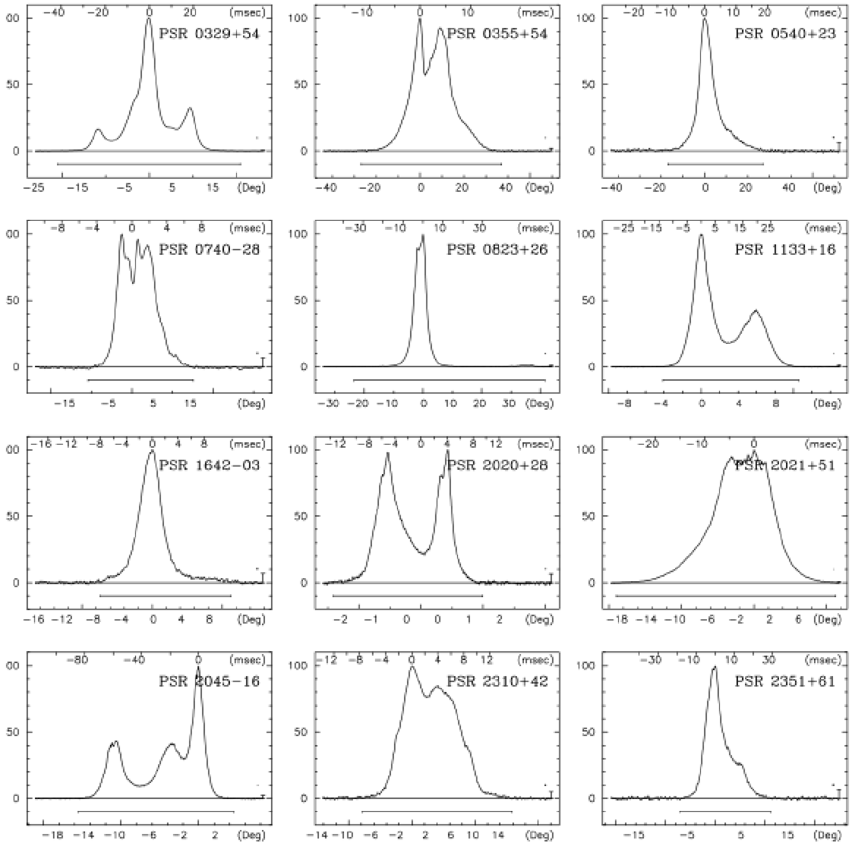

Figure 1.3: Integrated pulse profiles of some pulsars at 1.4 GHz. Figure taken from Seiradakis and Wielebinski (2004)

pulsar (Backer, 1970). The integrated profiles also vary in their shapes according to the observing frequency. This is because the radio emission mechanism emits different frequencies at different heights from the pulsar surface. This is called Radius to Frequency Mapping (Cordes, 1978; Thorsett, 1992). Usually, the pulse width and the separation between components increase towards the lower radio frequencies (Hankins and Rickett, 1986). An example of profile evolution with frequency from 1400 MHz down to 30 MHz is shown in Figure 1.4.

1.1.1.3 Flux densities and spectra

Pulsars are considered to be weak radio sources in general. Flux densities are measured in the unit of Jansky (Jy), where 1 Jy= 10^{-26} W m^{-2} Hz^{-1} (Lorimer and Kramer, 2004). The typical flux densities of pulsars are below 1 Jy at radio wavelengths[†]. Flux densities of pulsars are measured as mean flux densities, which is the measured integrated pulse intensity of the profile averaged over the pulse period. The mean

---

[†] https://www.atnf.csiro.au/research/pulsar/psrcat/

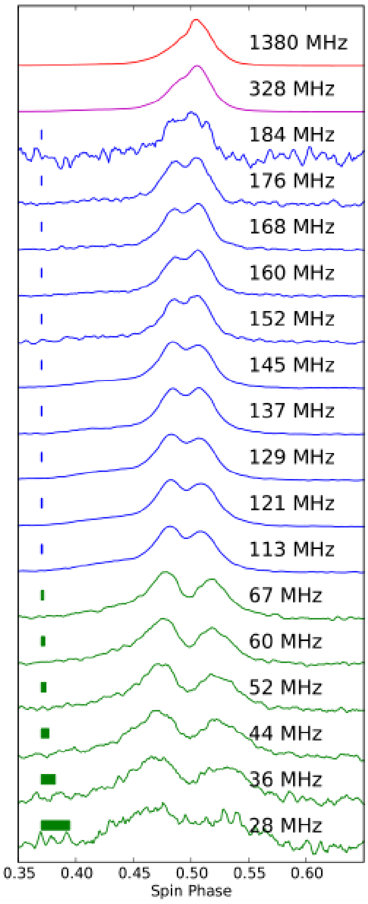

Figure 1.4: Example of pulsar profile evolution for PSR B0950+08. Figure taken from Pilia *et al.* (2016)

flux density of pulsars has a strong inverse relation with the observing frequency i.e., the mean flux density ($S(\nu)$) decreases with increasing observing frequency (ν). Most pulsars follow a steep spectrum, which can be represented by a first-order power law:

$$S(\nu) \propto \nu^{\alpha} \tag{1.1}$$

where α is the spectral index. The spectral indices lie in the range of -1 to -4 and have an average value of -1.41 (Bates, Lorimer, and Verbiest, 2013). Some pulsars show a broken spectrum with two different spectral indices at low and high radio frequencies. For some pulsars, there is complete turnover where the spectral index flips from negative to positive at a certain frequency. This is called “spectral turnover”. The mean flux density starts decreasing instead of increasing as the observing frequency decreases below the turnover frequency. This turnover usually happens at a frequency of around 100-300 MHz. Figure 1.5 shows some examples of pulsar spectra.

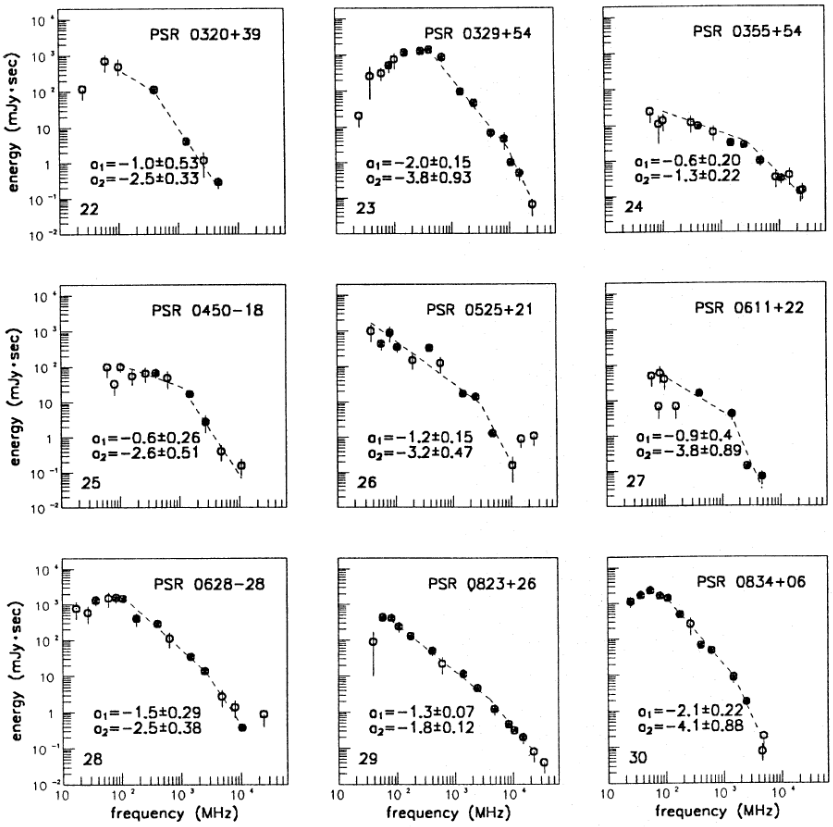

Figure 1.5: Spectra of a few pulsars. Figure taken from Malofeev *et al.* (1994)

1.1.2 Effects of Interstellar medium

Signals traveling from pulsars to the Earth interact with the intervening Interstellar Medium (ISM). ISM is a diffuse mixture of gas, dust, ions, and electrons that fills the empty space between the stars in our Galaxy. The ionized plasma produces various effects on the pulsar signal traveling through it. These include dispersion, scattering, initiation, and Faraday rotation. Many of these effects are observable only in the case of pulsed signals. Hence, pulsars are considered significant probes for studying the properties of the ISM. However, studies of the intrinsic properties of radiation from pulsars become difficult in the presence of these propagation effects.

1.1.2.1 Dispersion

The free electrons in the cold, ionized plasma of ISM give it a frequency-dependent refractive index. The refractive index is given by

$$\mu = \sqrt{1-\left(\frac{f_p}{f}\right)^2} \tag{1.2}$$

where f is the observing frequency and f_p is the plasma frequency given by

$$f_p^2 = \frac{e^2 n_e}{\pi m_e} \tag{1.3}$$

Here n_e is the electron density of the plasma, e is the charge of an electron, and m is the mass of an electron. For ISM, $n_e \sim 0.03cm^{-3}$ (Lorimer and Kramer, 2004). So $f_p \simeq 1.5kHz$ and wave will not propagate when $f < f_p$. The group velocity of a propagating wave is given by

$$v_g = c\mu \tag{1.4}$$

where c is the speed of the light.

From equation 1.2 $\mu < 1$. So, in ISM, the group velocity of radio waves is less than the speed of light and is a function of wave frequency. In the observation band, the pulse at a higher frequency will arrive earlier than at a lower frequency. The propagation of a radio signal of frequency f along a path of distance d will be delayed in time with respect to a signal of infinite frequency by an amount

$$t = \left(\int_0^d \frac{\mathrm{d}l}{v_g} \right) - \frac{d}{c}. \tag{1.5}$$

Using $v_g = c\mu$ and $f >> f_p$, we get

$$t \simeq \mathrm{D} \times \frac{DM}{f^2}, \tag{1.6}$$

where D is the Dispersion constant given by

$$D = \frac{e^2}{2\pi m_e c} \simeq 4.15 \times 10^3 \, \mathrm{MHz}^2 \, \mathrm{pc}^{-1} \, \mathrm{cm}^3 \, \mathrm{s}. \tag{1.7}$$

And DM is the Dispersion measure, i.e., integrated free electron density along the line of sight given by

$$DM = \int_0^d n_e \mathrm{d}l \tag{1.8}$$

and is expressed in units of pc-cm^{-3}.

So, the delay between two frequencies f_1 and f_2 in MHz is given by

$$\Delta t \simeq 4.15 \times 10^6 \times (f_1^{-2} - f_2^{-2}) \times DM \text{ ms}. \tag{1.9}$$

Figure 1.6 shows an example of dispersed pulse observed from Pulsar J1800+5034. It can be seen that the pulse arrives earlier in the higher frequency of the observation band than the lower frequency. The "de-dispersed" band-integrated pulse profile is shown at the top of the figure. Though the dispersion effect makes searching for pulsar signals difficult, it helps to distinguish between signals from celestial sources and the

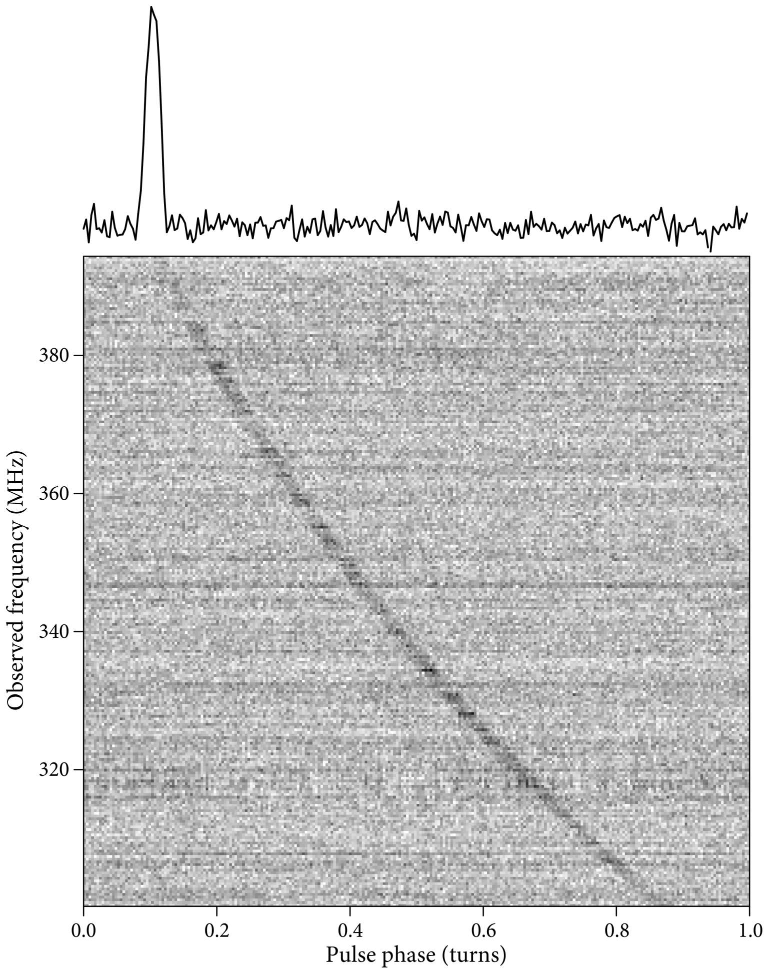

Figure 1.6: Example of pulse dispersion. Credits: NRAO

locally generated radio frequency, as the latter is not generally dispersed. It also gives a means to determine distances to pulsars. By measuring the pulse arrival time at two or more different frequencies, the DM along the line of sight can be determined. Then, the distance to the pulsar can be estimated using the DM and considering a model for galactic electron density (see, e.g. Taylor and Cordes, 1993). Conversely, if distances to pulsars are already known by some other methods, then the DM can be used to make a model of the Galactic electron density distribution (e.g., the NE2001 model by Cordes and Lazio, 2002).

1.1.2.2 Scattering

The irregularities in the electron density along the line of sight of the pulsar cause scatter broadening of the pulse profile. Due to the fluctuations in the electron density of ISM, the pulsar signal undergoes multipath propagation, which causes stretching of the integrated pulse. The effects of the scattering can be described by the Thin Screen model (Scheuer, 1968). Although the irregular medium extends through the whole propagation path, in the thin screen model, it is assumed that all of the scattering occurs midway between the pulsar and the observer by an infinitely thin region- the scattering screen. As the pulsar signal travels through the ISM, it is scattered because of these fluctuations through an angle θ, which is assumed to follow a Gaussian probability distribution:

$$I(\theta) \propto exp\Big(\frac{-\theta^2}{\theta_d^2}\Big) 2\pi\theta \mathrm{d}\theta, \tag{1.10}$$

where θ_d is the angular radius of the scatter-broadened image of a point source.

$$\theta_d \approx \frac{e^2}{2\pi m_e} \frac{\Delta n_e}{\sqrt{a}} \frac{\sqrt{d}}{f^2} \tag{1.11}$$

where d is the distance of the pulsar from Earth, a is the characteristic length scale of irregularities, Δn_e is the RMS change in the electron density, and f is the observing frequency. The geometric time delay between the rays received at an angle of θ and direct rays is

$$\Delta t(\theta) = \frac{\theta^2 d}{c} \tag{1.12}$$

As a result, the scattered radiation arrives slightly later than the unaltered radiation. This causes time smearing of the pulse. As the scattering angle follows a Gaussian distribution, the pulse shape is effectively convoluted with a truncated exponential, introducing an exponential tail in the time domain. The observed intensity as a function of time is given by

$$I(t) \propto e^{-\Delta t/\tau_{sc}} \tag{1.13}$$

where τ_{sc} is the scatter-broadening time scale given by

$$\tau_{sc} = \frac{\theta_d^2 d}{c} \tag{1.14}$$

So,

$$\tau_{sc} \propto \frac{\Delta n_e^2}{a} d^2 f^{-4}. \tag{1.15}$$

A sharp pulse is observed as a one-sided exponential. From the equation 1.15, it can be seen that the scattering effects have a strong dependence on the observing frequency. The lower the frequency, the longer the tail of exponential. Figure 1.7 illustrates this where the increasing effect of scatter broadening at lower frequencies is seen. Note that the analysis shown here assumes isotropic Gaussian distribution for the density fluctuations, which yield $\tau_{sc} \propto f^{-4}$. If Kolmogorov distribution is assumed, it will have a dependence of $\tau_{sc} \propto f^{-4.4}$ (Geyer and Karastergiou, 2016). τ_{sc} is correlated with the Dispersion measure (DM) also (Bhat *et al.*, 2004). Pulsars having high DMs show large scattering tails at low frequencies (Malov and Malofeev,

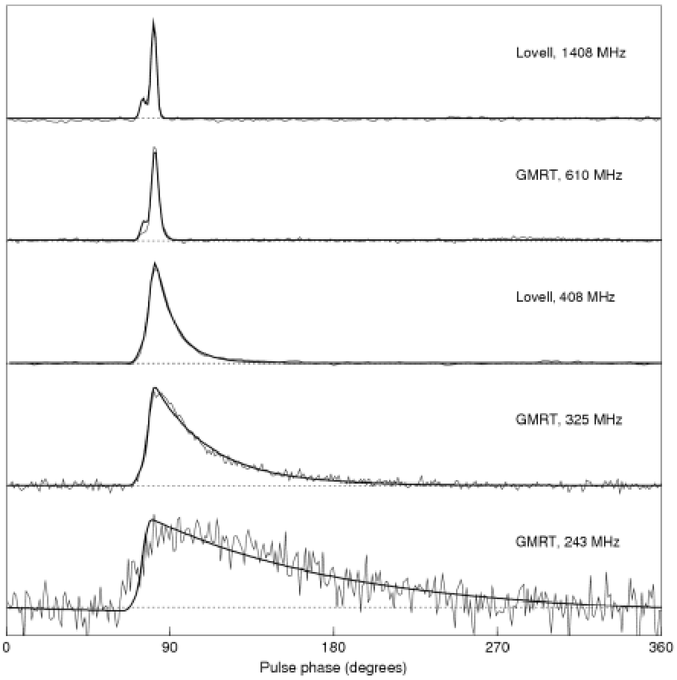

Figure 1.7: Pulse profiles of Pulsar B1831-03 at five different frequencies. Figure taken from (Lorimer and Kramer, 2004)

2010; Krishnakumar *et al.*, 2015).

1.1.2.3 Scintillation

Optical scintillation is familiar to us as the twinkling of stars. Similarly, scintillation is observed at radio wavelengths due to the intervening medium's irregularities. The ISM is highly turbulent and inhomogeneous. The propagating pulsar signal undergoes phase modulations due to these irregularities, which cause variations in the observed intensity (see for an overview Narayan, 1992). Similar effects are observed in the passage of radio waves through the Earth's ionosphere. This phenomenon was soon recognized after the discovery of pulsars as a slow fading pattern of radio signals by Lyne and Rickett (1968). The basic analysis of scintillation was presented by Scheuer (1968) in which the turbulent ISM is modeled as a thin screen of irregularities midway between the Earth and the Pulsar, as shown in figure 1.8. The signals received over time τ_{sc} show a phase variation $\Delta\Phi \sim 2\pi f \tau_{sc}$. This produces an interference pattern on the observer's plane. Due to the relative motion between the pulsar, the medium, and the observer, this pattern moves over the observer, causing intensity variation over timescale Δt. The condition for interference to be constructive is

$$2\pi \Delta f \tau_{sc} \sim 1, \tag{1.16}$$

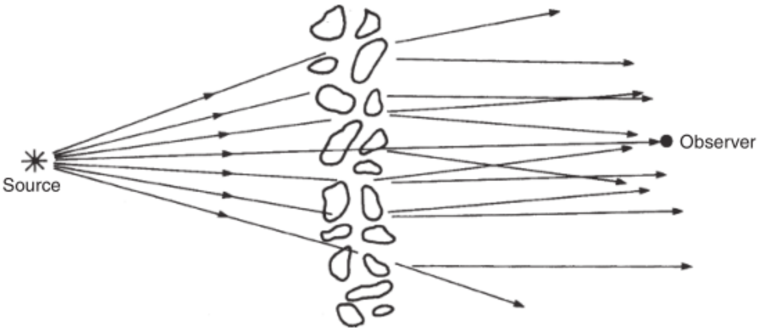

Figure 1.8: A thin-screen model of scintillation. Image taken from Lyne and Graham-Smith (2012)

where Δf is called Scintillation bandwidth.

$$\Delta f \propto \frac{1}{\tau_{sc}} \propto f^4 \tag{1.17}$$

The waves of frequencies outside this bandwidth will not contribute to the interference. Therefore, scintillation produces intensity variation in both time and frequency. Scintillation is used to investigate the interstellar medium and the velocities of pulsars (see, e.g. Bhat, Rao, and Gupta, 1999).

1.1.2.4 Faraday Rotation

Pulsar signals are highly linearly polarized (Lyne and Smith, 1968). The magnetic field of the Galaxy acts like a "Faraday screen," rotating the angle of linear polarization by an amount proportional to the line of sight component of the magnetic field weighted by the electron density. The rotation measure (RM) can be used to map out the large-scale structures of the Galactic magnetic field (Lyne, Smith, and Graham, 1971). Rotation Measure (RM) is defined as:

$$RM = \frac{e^3}{2\pi m_e^2 c^4} \int_0^d n_e B_{||} \mathrm{d}l \tag{1.18}$$

$B_{||}$ is the component of the plasma's magnetic field, which runs parallel to the line of sight. Then, the Faraday rotation is given by

$$\Delta\phi = RM\lambda^2 \text{ radians} \tag{1.19}$$

If we compare the equations 1.8 and 1.18, we get

$$\langle B_{||} \rangle = 1.23 \frac{RM}{DM} \tag{1.20}$$

Where $\langle B_{||} \rangle$ is the mean line-of-sight component of the magnetic field in $\mu{-}gauss$, RM in rad/m^2 and DM in pc/cm^3.

1.2 Pulsar signal processing techniques

While searching for pulsars, we look for their two signatures: their periodicity and their dispersion. As mentioned in the earlier section, pulsars have very stable periods. While searching for new pulsars, the periodic nature of its signals comes in handy. Data from a radio telescope is usually in the form of time series. So, one way to look for periodic signal signatures is the Fourier transform. Discrete Fourier Transform (DFT) can be used to determine the Fourier components $X(k)$ of a time series $x(n)$ having N points as

$$X(k) = \sum_{n=0}^{N-1} x(n) e^{-j2\pi \frac{kn}{N}} \tag{1.21}$$

It gives a power spectrum, which is power as a function of frequency. Any peak in the power spectrum corresponds to periodicity in the time series. Thus, to identify the presence of a pulsar signal in the data, the Fourier transform can be computed and searched for significant peaks in the power spectrum. Several harmonics in the spectral domain can be combined to increase the sensitivity of the search. This technique is called 'incoherent harmonic summing' (Taylor and Huguenin, 1969). Once the candidates are identified, the following two main processes are done to confirm pulsar detection.

1.2.1 Folding

As mentioned in the earlier section, pulsars are weak radio sources. For most of the pulsars, it is difficult to see their individual pulses against the background noise. So, the only way is to see the integrated profile, i.e., the averaged pulse profile. It is obtained through a process called 'Folding.' The time series data is divided into chunks of the size of the nominal period and then added together. For N such chunks added, the noise increases by $\sqrt{N}$ while the pulsar signal gets stronger N times. So, the overall signal-to-noise ratio (SNR) after adding N pulses improves by $\sqrt{N}$.

1.2.2 Dedispersion

In section 1.1.2.1, we saw that while traveling in the interstellar medium, pulsar signals undergo dispersion. So, the low-frequency signals are delayed compared to the high frequency. For a finite receiver bandwidth, this dispersion process broadens the pulse when combined across the observing band so that its signal-to-noise ratio (SNR) is reduced. If the dispersion delay over the observing band is larger than the pulsar period, the pulses at different frequencies smear together, making it difficult to detect the pulsar. Hence, it is vital to correct this effect dispersion. For this, a process called 'Dedispersion' is used. This can be done by one of the following two methods:

1.2.2.1 Incoherent dedispersion

In this method, the frequency band is divided into multiple sub-bands or channels, and appropriate time delays are applied to each channel so that the pulse received in each channel aligns. The time delays required for each frequency channel are calculated using the equation 1.9. The time delay Δt required for a particular frequency channel f_{chan} with respect to a reference frequency channel f_{ref} can be calculated as

$$\Delta t \simeq 4.15 \times 10^6 \times (f_{ref}^{-2} - f_{chan}^{-2}) \times DM \text{ ms.} \tag{1.22}$$

The appropriately delayed frequency channels can then be added together. If we assume a finite bandwidth $\Delta f = f_1 - f_2 << f_1, f_2$, about some central frequency f_o, then equation 1.9 can be rearranged as

$$\Delta t_{smear} \simeq 8.3 \times 10^6 \times DM \frac{\Delta f}{f_o^3} \text{ ms.} \tag{1.23}$$

Thus, for a frequency channel of width Δf around a central frequency f_o, the pulse will be smeared by an amount Δt_{smear}. So, in the incoherent dedispersion method, the dispersion delay within each frequency channel remains uncorrected. If the frequency channels are not narrow enough, then the intra-channel smearing of the pulse will still be dominant, especially at lower radio frequencies and higher DMs. Figure 1.9 illustrates the concept of incoherent dedispersion.

1.2.2.2 Coherent dedispersion

The effects of interstellar dispersion can be completely removed by using coherent dedispersion (Hankins and Rickett, 1975). Coherent dedispersion uses a filter to remove the dispersive delay before the data are converted from raw voltages to power. The filter has a transfer function, which is a complex conjugate of the transfer function representing dispersion in the interstellar medium. The original signal can be recovered from the received voltage signal by an inverse filtering operation. In this method, the dispersive delay is removed completely without the intra-channel smearing associated with the incoherent dedispersion method.

The time resolution achievable in this scheme is $1/B$, the maximum possible for a signal of bandwidth B. The practical resolution limit is then set by the maximum bandwidth that can be sampled without causing aliasing. The main drawback of coherent dedispersion is that practical realizations of this scheme are not easy as it is a highly compute-intensive operation. Generally, an incoherent dedispersion scheme is used when searching for new pulsars as a pulsar's DM is not known a prior. The

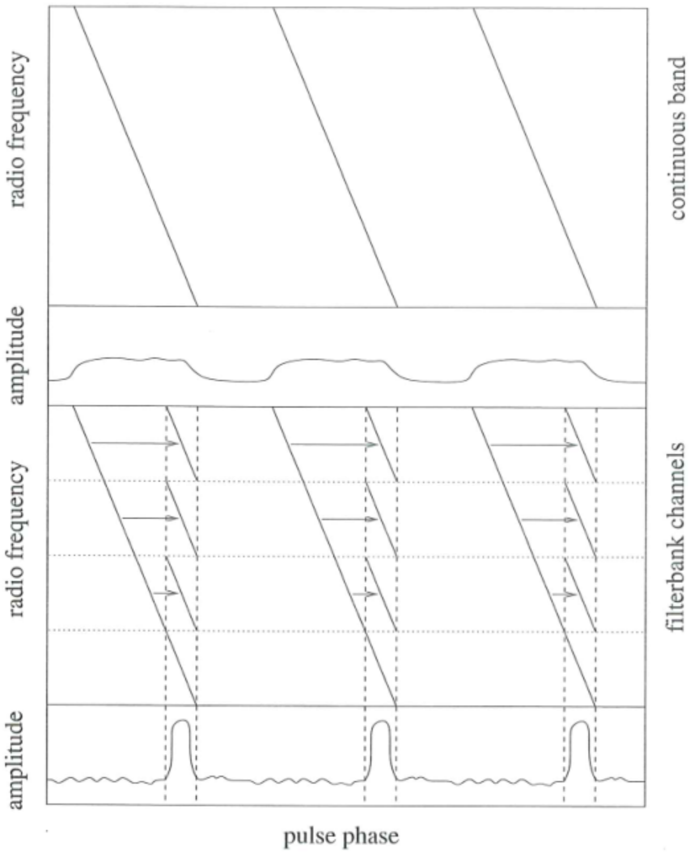

Figure 1.9: Incoherent dedispersion. Image taken from Lorimer and Kramer (2004)

data is divided into a number of sub-bands, which are then dedispersed using various trail DMs in a wide range. Coherent dedispersion is used for targeted observations when a pulsar's DM is known to a good accuracy.

1.3 Requirements for pulsar observations

Based on the discussion so far, there are some requirements to develop an instrument for pulsar observations.

1.3.1 Sensitivity considerations

Pulsar signals are buried in the noise contributed by the galactic background and receiver. Pulsar searches, therefore, require highly sensitive receivers. The minimum temperature a radio telescope can detect is limited by the fluctuations at the receiver output caused by the noise (Kraus, 1966). For a signal with bandwidth $\Delta\nu$ and the available number of polarizations N_p, the total number of independent data samples recorded over an integration time of τ is $N = N_p \Delta\nu\tau$. The system temperature (T_{sys})

is the total random noise power generated in the receiver while looking at the sky. System temperature can be generally expressed as

$$T_{sys} = T_{sky} + T_{rec} \tag{1.24}$$

T_{sky} is the contribution of the background sky, and T_{res} is the noise added by the receiver to the system, which represents the internal noise from the receiver components plus the unwanted noise from the antenna produced by ground radiation, atmospheric emission, ohmic losses, and other sources.

The minimum detectable temperature by a radio telescope is the *rms noise temperature* given by

$$\Delta T_{min} = \Delta T_{rms} = \frac{T_{sys}}{\sqrt{N}} = \frac{T_{sys}}{\sqrt{N_p \Delta\nu \tau}} \tag{1.25}$$

The system temperature can be reduced by increasing the integration time or the observation bandwidth. However, in practice, the integration time cannot be increased beyond the point where it distorts the true source profile and bandwidth cannot be made too wide without loss of some spectral details or of radio frequency interference (RFI).

In the presence of the source, the noise temperature in the antenna T_A is given by

$$T_A = \frac{A_e S_\nu}{2k} \tag{1.26}$$

where A_e is the effective collecting area of the radio telescope, S_ν is the flux density from the source, and k is the Boltzmann constant. The excess temperature on-source is T_A, so the signal-to-noise ratio (SNR) is

$$SNR = \frac{T_A}{\Delta T_{rms}} = \frac{A_e S_\nu \sqrt{N_p \Delta\nu \tau}}{2kT_{sys}} \tag{1.27}$$

The minimum detectable flux density is then

$$\Delta S_{min} = \frac{2kT_{sys}}{A_e \sqrt{N_p \Delta\nu \tau}} \ \mathrm{Wm^{-2}Hz^{-1}} \tag{1.28}$$

In terms of Janksy (Jy)

$$\Delta S_{min} = \frac{2kT_{sys}}{A_e \sqrt{N_p \Delta\nu \tau}} \ 10^{26}\mathrm{Jy} \tag{1.29}$$

The system equivalent flux density (SEFD) i.e., the flux density of the source that doubles the noise power of the system, is

$$SEFD = \frac{2kT_{sys}}{A_e} \ 10^{26}\mathrm{Jy} \tag{1.30}$$

In the case of pulsars, the detection limit is expressed in terms of the mean flux of the pulsar as

$$S_{mean} = SNR\frac{2kT_{sys}}{A_e\sqrt{N_p\Delta\nu\tau}}\sqrt{\frac{W}{P-W}} \tag{1.31}$$

where SNR is the signal-to-noise ratio limit required for detection, W and P are the width of the integrated profile and the pulse period, respectively (Vivekanand, Narayan, and Radhakrishnan, 1982; Bondonneau *et al.*, 2020).

From the above equation, it is clear that in order to have better sensitivity i.e., a lower value of the minimum detectable flux, we should have

- Larger collecting area
- Wider observation bandwidth
- Longer integration time
- Lower system (receiver) temperature

For observations with a radio telescope, optimal values of bandwidth and integration time are selected so as not to hamper the quality of observations. For e.g., longer integration time may dissolve the varying nature of a transient source, and longer bandwidth may cause loss of spectral signatures.

1.3.2 Phased array requirements

From the previous section, it is evident that pulsar observations benefit from the availability of large collecting areas. As pulsars are weak radio sources, array telescopes are used to increase the sensitivity. However, being compact sources of radiation, pulsars are essentially point sources even for the longest interferometer baseline. So instead of interferometric mode, the array telescopes are used in phased array mode (Thompson, Moran, and Swenson, 2017). In a phased array, the outputs from discrete antenna elements are combined to obtain a single, total power signal from the array. Because of this, the complicated hardware of the correlator required to measure the visibilities on all baselines is not needed. Figure 1.10 shows the basic difference between a correlator array and a phased array.

Phased array mode can be used in two ways: ‘Incoherent phased array’ where the signal from each antenna is put through a detector and the output from these is added to obtain the total signal, and ‘Coherent phased array’ where the voltage signal from each antenna is added, with appropriate phase shifts, and the summed output is put through a detector to obtain the total power signal. For an array of N antennas, the incoherently phased array gives an effective collecting area of $\sqrt{N}$ times that of a single antenna, while the coherent array gives an effective collecting area of

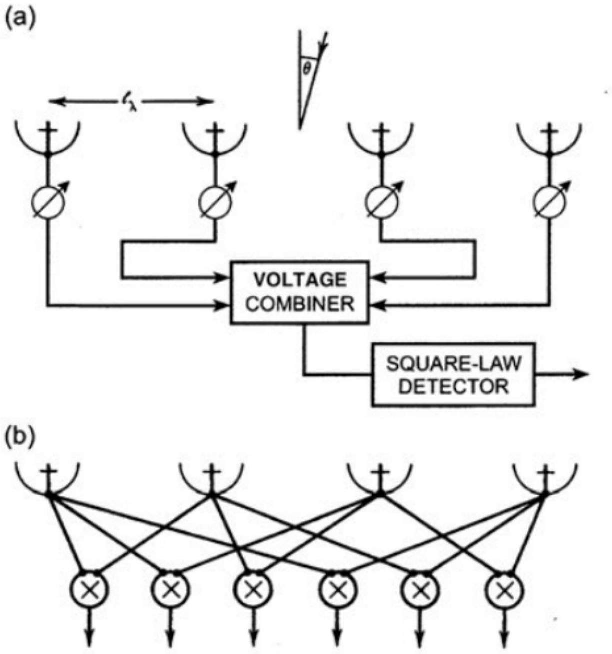

Figure 1.10: Simple four-element linear array connected as (a) a coherent phased array, (b) a correlator array. Image taken from Thompson, Moran, and Swenson (2017)

N times that of a single antenna[‡]. The angular resolution in case of the incoherent array is same as that of the single antenna and foe coherent array it is $\sim \lambda/D$, where D is the largest spacing between antennas in the array and λ is the wavelength of observation. In general, the coherent array mode is used for targeted observations of known pulsars, whereas the incoherent mode is used for surveys of pulsar search where the aim is to cover the maximum area of the sky in a given time.

1.3.3 Temporal and spectral resolution requirements

As mentioned in section 1.1.1.1, pulsars have very stable periods that range from a few seconds to milliseconds. Their pulse widths are only a fraction of their periods, typically less than 5% duty cycles. To study such pulses, data with fine time resolution is required. Time resolution in ranges of microseconds to milliseconds is ideal for pulsar studies. Thus, pulsar observation requires high sampling rates. High time resolution results in very high data rates and requires massive data storage and management systems. Also, pulsar spin-down rates ($\dot{P}$) can be measured using the Time of Arrival (ToA) measurements in 'Pulsar timing' studies (Manchester, 2017). This requires a very precise clock at the radio telescope.

In section 1.2.2 we saw that it is essential to correct for dispersion effects caused by

---

[‡] `http://www.ncra.tifr.res.in/ncra/gmrt/gmrt-users/low-frequency-radio-astronomy`

the interstellar medium on the received pulsar signals. And that requires breaking the observing frequency bands into narrow frequency channels to perform dedispersion. This can be done using a digital spectrometer where the incoming time series signal is divided into frequency channels using the Fourier transform. For pulsar observations, these frequency channels have to be very narrow, i.e., very high spectral resolution is required. If the channels are not narrow enough the detection suffers loss in sensitivity due to intra-channel smearing as per the equation 1.23. However, one cannot have infinitely narrow frequency channels. A frequency channel of width $\Delta\nu$ will provide independent samples only a time intervals of $1/\Delta\nu$. So, it will not be possible to achieve a time resolution better than that. An optimal choice for channel bandwidth is when $t_{smear} = 1/\Delta\nu$ (Deshpande, 1989). Using this and equation 1.23 gives an optimal channel bandwidth as (Ramkumar, Prabu, and Markendeyalu, 1994)

$$\Delta f_{opt} = (10^{-4}/9.1) \times \sqrt{f_o^3/DM} \tag{1.32}$$

where Δf_{opt} and central frequency f_o are in MHz and DM in pc/cm^3.

1.4 Pulsar observations at low radio frequencies

The first pulsar was detected at 81.5 MHz (Hewish *et al.*, 1968) more than 50 years ago. Since then, pulsars have been detected over the entire electromagnetic spectrum- from low radio frequencies (10 MHz, which is at the ionospheric cutoff, Hassall *et al.*, 2012) to high radio frequencies (87 ,GHz, Morris *et al.*, 1997), up to high energy Gamma ray photons (1.5 TeV, Ansoldi *et al.*, 2016). After the discovery, many of the initial studies on pulsars concentrated on low radio frequencies $<$ 300 MHz (Staelin and Reifenstein, 1968; Cole, 1969; Rankin *et al.*, 1970) which played a crucial role in the development of pulsar science (Taylor and Manchester, 1977; Taylor and Stinebring, 1986). However, since then, the majority of the pulsars have been discovered and studied at frequencies in the range 300–2000 MHz (Stappers *et al.*, 2011). Much of our knowledge and understanding of pulsar emission properties come from the above frequency range. In particular, observations below 100 MHz are rare. Out of the total pulsar population (~3000)[§], only 83 have been detected below 100 MHz (Bondonneau *et al.*, 2020). Properties of pulsar emission at radio frequencies below 100 MHz have remained relatively uncharted and unexplored. The major reasons for these include high levels of galactic background emission and the propagation effects of ISM, which are stronger at lower radio frequencies and spectral turn-over, causing low flux densities. These effects conspire to make observations below 100 MHz challenging.

[§] `https://www.atnf.csiro.au/research/pulsar/psrcat/`

1.4.1 Challenges for low radio frequencies observations

1.4.1.1 Galactic background

The galactic background emission, which is predominantly high because of the non-thermal Synchrotron emission as Cosmic rays move in the Galactic magnetic field, has a strong frequency dependence with steep spectra ($\propto \nu^{-2.55}$ Lawson *et al.*, 1987). The background emission increases significantly at low radio frequencies. For e.g., the average sky temperature at 34.5 MHz is 10,000 K (Dwarakanath and UdayaShankar, 1990), and at 60 MHz, sky temperatures reach ∼8,500 K in the galactic plane (Bondonneau *et al.*, 2020). This significantly increases the system temperature (T_{sys}) and, as it was seen in section 1.3.1, decreases the sensitivity of the radio telescope. This makes the detection of pulsars at low radio frequencies difficult as their signal are buried deeply in the noise, especially the ones in the Galactic plane. Note that most of the pulsars from the known pulsar population are located within 5° of the galactic plane (Stappers *et al.*, 2011).

1.4.1.2 Propagation effects

We saw in section 1.1.2 that the ISM causes pulse smearing due to dispersion and scattering. These effects have strong frequency dependence and can scale steeply as ν^{-2} and ν^{-4} respectively and are therefore most prominent at low frequencies. The effects of dispersion can be corrected using a dedispersion scheme. Incoherent dedispersion leaves intra-channel smearing and is limited by the sampling rate (section 1.3.3). Coherent dedispersion can fully correct the dispersion effects but is computationally very expensive and is used in only limited cases (e.g. Popov *et al.*, 2006; Karuppusamy, Stappers, and Serylak, 2011).

Even with the correction of dispersion effects, the scattering effects still remain. Pulsars become undetectable once the scatter broadening exceeds the pulsar period. The scattering timescales are correlated with DM (Bhat *et al.*, 2004) and beyond certain DM pulsars become undetectable. For e.g., in Bondonneau *et al.* (2020), there was no detection beyond DM of ∼57 pc/cm^3 in the frequency range 25–80 MHz.

Scintillation effects may also lead to non-detectability at low frequencies, causing apparent fluxes of pulsars to vary by a factor of ∼2–3 (Gupta, Rickett, and Coles, 1993; Bhat, Rao, and Gupta, 1999) and thus making them appear fainter than their true fluxes.

The ionosphere of the Earth also plays an important role in observations, contributing additional time and frequency-dependent phase delays to the incoming signals (Stappers *et al.*, 2011).

1.4.1.3 Pulsar spectral evolution

As discussed in section 1.1.1.3, pulsars are very weak radio sources and exhibit a very steep spectrum with an average spectral index of -1.4. They often peak and turn over at frequencies between 100 MHz to 200 MHz (Malofeev *et al.*, 1994). So, below 100 MHz, the flux densities of pulsars become too low, and they get buried in the strong Galactic background.

Also, the pulse widths of pulsars increase at lower radio frequencies (Malov and Malofeev, 2010). That reduces the peak flux density, resulting in poor signal-to-noise ratios.

1.4.1.4 Radio Frequency Interference

All low radio frequency observations are affected by interference from terrestrial sources. Radio Frequency Interference (RFI) reduces the sensitivity of a radio telescope and produces artifacts in the observed data. Spurious RFI signals are especially a problem in the searches for transients. Strong RFI signals can mask the dispersed radio pulse from pulsars. Persistent RFI signals raise the detection threshold, reducing sensitivity to weaker celestial signals. The FM broadcast band (88-108 MHz) essentially makes this band unusable for radio astronomy. RFI is broadly classified into two categories: 1) Broadband RFI, characterized by short time duration bursts from spark-like events, e.g., lightning, corona discharge in power lines, automobile ignition, etc. It causes an increase in the power level of the entire observing band 2) Narrowband RFI, which usually comes from transmissions from communication systems, e.g. TV broadcast transmitters, cell phone base stations, aircrafts, satellites, etc. (Ford and Buch, 2014). RFI can even mimic the dispersive nature of an astronomical pulse in the case of a swept-frequency signal. Identifying such RFI signals and filtering them is a big challenge in radio astronomy. Various mitigation techniques can be used to remove RFI (Buch, 2019).

1.4.2 Importance of low radio frequencies observations

Despite the challenges mentioned above, low-frequency observations of pulsars give a tremendous amount of information and are very useful. They can provide vital insights into the physics of the emission mechanism of pulsars and also the properties of the ISM.

It is currently accepted that the radio component of pulsar spectra is generated by coherent processes in the relativistic plasma of the pulsar magnetosphere (Lyne and Graham-Smith, 2012). But, despite decades of study, the exact mechanisms of the pulsar radio emission still remain unclear. Observations below 100 MHz can help investigate this problem as many interesting phenomena happen around at low radio frequencies, e.g., spectral turnover (Sieber, 1973), rapid profile evolution (Phillips and Wolszczan, 1992; Bhat *et al.*, 2004; Pilia *et al.*, 2016), etc. The frequency dependence of the average pulse profiles of most pulsars is complex. Their pulse shapes and widths change with frequency. Generally, the widths of integrated profiles become wider with lower observing frequencies (see, e.g., Johnston *et al.*, 2008). This can be explained by the radius-to-frequency model (RFM) (Cordes, 1978). Low-frequency emission originates in the higher altitudes of the pulsar magnetosphere. Therefore, pulsars observed at low frequencies give insight into their emission geometry. For e.g., using low-frequency observations Hassall *et al.* (2012) were able to put strong constraints on the height of radio emission. However, this simple picture is not the full story, as evidenced by morphological characteristics of polarized pulsar emission profiles (Rankin, 1993). There are cases where a simple profile at low frequencies becomes multi-component at higher frequencies (Kramer, 1994) and vice-versa (Izvekova, Malofeev, and Shitov, 1989). Different parts of the pulse profile can have different spectra, too (Malov and Malofeev, 2010). So, it is important to study pulsar integrated profiles at different frequencies and compare low-frequency observations with high-frequency ones to truly understand their beam geometry and emission mechanism. Also, studying spectral turnover, which is still not fully understood (Bilous *et al.*, 2020), will allow us to gain a better understanding of their enigmatic radio emission mechanism.

Pulsars are ideal probes for studying ISM. As the effects of ISM, which include dispersion, scattering, scintillation, and Faraday rotation are more prominent at low frequencies, it can be used to precisely measure properties of ISM like electron density and magnetic field (see, e.g., Stovall *et al.*, 2015) Temporal variations of the dispersion measures and scattering timescales can be monitored with very high precision to study the distribution of ionized plasma in the ISM. For e.g., the scattering tails can be studied to determine the distances and thickness of scattering screens (Rickett *et al.*, 2009). Pulsar timing is difficult at low frequencies as the required super-high precision is hindered by the ISM effects. However, low-frequency observations have the potential to better characterize the effects of ISM, which can be used for high-precision timing data at high frequencies (Hessels *et al.*, 2014).

1.4.3 Existing low frequency telescopes

In the past couple of decades, many radio telescopes have been developed around the world, operating at low frequencies. Following are some of the prominent radio telescopes which operate below 100 MHz: the Long Wavelength Array (LWA, New Mexico, 10-88 MHz, Ellingson *et al.*, 2009;), the Low-Frequency Array (LOFAR, the Netherlands, 10-240 MHz Stappers *et al.*, 2011; van Haarlem *et al.*, 2013), the Murchison Widefield Array (MWA, Australia, 70-300 MHz Steinberg *et al.*, 1971; Tremblay *et al.*, 2015), Ukrainian T-shaped radio telescope (UTR-2, Ukraine, 8-32 MHz Ryabov *et al.*, 2010), the Gauribidanur T telescope (GEETEE, India, 34.5 MHz Deshpande, Shevgaonkar, and Sastry, 1989). Note that besides MWA, all others are located in the Northern Hemisphere.

Multiple studies of pulsars at low radio frequencies have been conducted using these facilities. To name a few: LWA (Stovall *et al.*, 2015), LOFAR (Pilia *et al.*, 2016; Kondratiev *et al.*, 2016; Bilous *et al.*, 2016; Bilous *et al.*, 2020), LOFAR-FR606 (Bondonneau *et al.*, 2020), MWA (Xue *et al.*, 2017; Murphy *et al.*, 2017; Bhat *et al.*, 2004), GEETEE (Deshpande and Radhakrishnan, 1992), Pushchino (Malov and Malofeev, 2010), UTR-2 telescope (Zakharenko *et al.*, 2013), and EDA (Wayth *et al.*, 2017; Sokolowski *et al.*, 2021). These studies have contributed to multiple aspects of pulsar properties.

However, most of these telescopes work on a time-sharing basis, where time is allocated for particular observations based on the proposal. So, there is no continuous monitoring, which is required for transient searches. Thus, a dedicated telescope for observations of pulsars and other astrophysical transients at low radio frequencies can be beneficial.

1.5 The Gauribidanur Radio Observatory

Since 1976, the Gauribidanur Radio Observatory has been operated by the Indian Institute of Astrophysics (IIA), jointly with the Raman Research Institute (RRI). It is located about 100 km North of Bangalore, India (Longitude: 77.4° E; Latitude: 13.6° N). The main focus of the radio astronomy facilities at the Gauribidanur observatory is on the observations of the Sun. The following facilities are presently operated by IIA at the observatory:

- **Gauribidanur RAdio HeliograPH (GRAPH)**: GRAPH is a heliograph dedicated to imaging the solar corona simultaneously at multiple frequencies in the frequency range 40 - 150 MHz (Ramesh *et al.*, 1998). It's a "T" shaped radio interferometer consisting of 32 groups in East-West and 32 groups in North-South, with each group having 8 and 4 Log Periodic Dipole Antennas, respectively. The back-end is a 4096-channel digital correlator. The angular resolution is $3' \times 4'$ at 150 MHz, and the temporal resolution is 256 ms. The array is presently being augmented with orthogonal antennas in its N-S arm to facilitate Polarimetric imaging.

- **Gauribidanur LOw-frequency Solar Spectrograph (GLOSS)**: GLOSS is a high-resolution radio spectrograph used in conjunction with the GRAPH for obtaining the dynamic spectrum of the transient emission from the solar corona in the frequency range 40 - 500 MHz (Kishore *et al.*, 2014).

- **Gauribidanur Radio Interferometric Polarimeter (GRIP)**: GRIP is a one-dimensional radio telescope consisting of 40 antennas in E-W direction dedicated to observing the polarized radio flux from the entire solar corona in the frequency range 40 - 150 MHz (Ramesh *et al.*, 2008).

- **Gauribidanur RAdio Spectro-Polarimeter (GRASP)**: The primary aim of GRASP array is to observe the polarization properties of the non-thermal radio emission from the solar corona over the frequency range 50 - 500 MHz. Polarization observations are used to determine the magnetic field strength associated with sources that are responsible for the polarized radio emission.

1.6 Thesis outline

The thesis work involved the development of a new facility for dedicated observation of pulsars at low radio frequencies at the Gauribidanur observatory. During the course of the thesis, the Gauribidanur Pulsar System (GAPS) was developed and used for targeted observations of pulsars.

Chapter 2 includes the design and development of the Prototype system using Log-Periodic Dipole antennas. It describes the front-end and the back-end system with its components, the testing and characterization of the system, and targeted observations of Pulsars in the frequency range of 50 - 80 MHz.

Chapter 3 includes the upgrading of GAPS to a digital beam-forming system. Multiple simultaneous beams were formed and used to simultaneously observe a Pulsar and a solar burst. Such simultaneous observation gives an opportunity to calibrate the one using the other, which is demonstrated and described in Chapter 3.

Chapter 4 includes the description and results of the raw voltage recording system that was used to record 1-bit raw voltage streams from individual antennas. This allows multiple simultaneous beams to be formed in the sky in post-processing, covering a large field of view. The upgraded back-end system, the methods, and the results are described here.

Chapter 5 discusses the importance of transient observations at low radio frequency and Single pulse search efforts that were put in that regard.

Finally, Chapter 6 concludes the thesis with a summary of the work and future prospects.

Chapters 2 to 4 are as per the three publications that were published in refereed journals during the course of the thesis (Bane *et al.*, 2022, 2023, 2024). Some other relevant information related to the Gauribidanur Pulsar System is included in the appendices.

Chapter 2
The prototype system

Prototype for pulsar observations at low radio frequencies using log-periodic dipole antennas
Kshitij S. Bane, Indrajit V. Barve, G. V. S. Gireesh, C. Kathiravan, R. Ramesh,
2022, **J. Astron. Telesc. Instrum. Syst.**,8(1),017001.

2.1 Introduction

A pulsar is a neutron star, i.e. the ultra-dense core that remains after a massive star undergoes a supernova explosion. It spins at very rapid rates ranging from once in a few seconds to as much as ∼700 times per second. The strong magnetic fields ($\sim10^8-10^{14}$ G) created when the neutron star was formed and the star's rapid rotation results in a magnetosphere. The radio emission comes out in two beams, one from each pole of the magnetosphere. The observed emission is coherent, but the mechanism behind the coherence is still being debated. Due to misalignment of the magnetic and rotation axes, these rotating beams of radiation could be noticed whenever they intersect our line of sight to the pulsar, much like a lighthouse on the sea-shore. Each rotation of the pulsar thus produces a narrow pulse of radiation. The first pulsar was observed at a low frequency of ≈81.5 MHz (Hewish *et al.*, 1968). But, much of our present knowledge about pulsars have come primarily from radio observations at frequencies >300 MHz. The primary reason for this is that the emission from the pulsars at low frequencies are more affected by dispersion and scattering during their propagation through the interstellar medium (ISM) as compared to higher frequencies. While the delay in the arrival time of the pulses due to the dispersive properties of the ISM varies as ν^{-2} (where ν is the frequency of observation), the interstellar scattering changes as $\sim\nu^{-4}$ (see e.g.). The latter leads to broadening of the pulses as a result of which they overlap (Bhat *et al.*, 2004; Geyer *et al.*, 2017). It then becomes difficult to distinguish the maxima and minima in a pulse. The periodic nature of the signal is either subdued or nearly lost when the pulse broadening time becomes nearly comparable to the spin period of the pulsar (see e.g. Gupta *et al.*, 2016). The other reasons for the limited observations of pulsars at frequencies $\lesssim$100 MHz are the comparatively intense synchrotron emission from the Galactic background, and the radio frequency interference (RFI).

Pulsar observations at frequencies $\lesssim$100 MHz are necessary to understand the emission mechanism and the characteristics of the pulse profile as a function of frequency which are still being examined. For example, the radius-to-frequency mapping (RFM) effect in pulsars are most prominent at lower frequencies (Cordes, 1978; Thorsett, 1991). Many pulsars exhibit a turn-over in the spectrum close to $\approx$100 MHz (Malofeev *et al.*, 1994; Bilous *et al.*, 2016). Therefore the extension of their spectra towards lower radio frequencies is naturally of great interest. This is especially so for those pulsars whose intensity is increasing with decreasing frequency in the known part of their spectra. An understanding of the propagation of the low frequency radio waves in the ISM is also important. The ν^{-4} dependence of scattering in the ISM makes the dispersion effects more stronger at lower frequencies and hence it is easier to carry out better measurements of the dispersion measure (DM). Observations of pulsars at frequencies $\lesssim$100 MHz are currently carried out with LOFAR (Stappers *et al.*, 2011; Bilous *et al.*, 2020), UTR-2 telescope (Zakharenko *et al.*, 2013), MWA (Tingay *et al.*, 2013), LWA (Stovall *et al.*, 2015), and EDA (Wayth *et al.*, 2017; Sokolowski *et al.*, 2021) in the time sharing mode. Exploration of transient phenomena in the Universe is an exciting and rapidly growing area of radio astronomy. Considering these, we have set-up a radio telescope in the Gauribidanur observatory (Sastry, 1995; Ramesh, 2011) (Longitude: 77.4° E; Latitude: 13.6° N) for dedicated observations of pulsars in the frequency range 50 - 80 MHz. RFI in Gauribidanur is also minimal (Monstein, Ramesh, and Kathiravan, 2007; Hariharan *et al.*, 2016b; Mugundhan *et al.*, 2018). We propose to observe and understand the characteristics of the known pulsars and the repeating Fast Radio Bursts (FRBs) (Thornton *et al.*, 2013; Fedorova and Rodin, 2019; Pleunis *et al.*, 2021; Pastor-Marazuela *et al.*, 2021) at low frequencies. The observing facility described in the work is a dedicated instrument with wide sky coverage, large bandwidth, and high time resolution (see Sections 2 and 3) all of which are important for observations of fast transients (see e.g. Gupta *et al.*, 2016). In the rapidly developing field of study of the transient sky, FRBs are perhaps the most exciting objects of scrutiny at present. So there is potential for new observations (Maan, 2015).

2.2 The Antenna and Front-end Analog Receiver System

The basic signal reception element used in the present case is a Log Periodic Dipole Antenna (LPDA). It is a type of broadband directional antenna whose characteristics are nearly constant over its entire operating frequency range (Rumsey, 1957). We have set-up an array of 16 LPDAs on a north-south baseline with a spacing of 5 m between the adjacent antennas. They are combined as two groups with 8 LPDAs in each group (see Figure 2.1). The LPDAs used in the array are designed according to the formulations reported in the literature (Carrell, 1961). The characteristic impedance of the LPDA is ≈50 Ω. Its half-power beam widths (HPBW) as per calculations are ≈80° (E-plane) and ≈110°(H-plane). All the 16 LPDAs have been mounted with their H-plane in the east-west direction. The effective collecting area and gain of each LPDA is $\approx 0.4\lambda^2$ (where λ is the wavelength corresponding to the observing frequency) and ≈6.5 dBi (with respect to an isotropic radiator), respectively. The Voltage Standing Wave Ratio (VSWR) is <2 over the frequency range ≈40 - 440 MHz (Kishore *et al.*, 2014). The aforementioned effective collecting area and the HPBW of the LPDA are larger compared to that of the other similar frequency independent receiving elements like the inverted V-shaped dipoles and bowtie antennas, respectively, used elsewhere. Since the LPDAs are arranged on a north-south baseline, the combined response pattern of the array (16 LPDAs) is ≈110° in the east-west (hour angle) direction and ≈3° in the north-south (declination) direction for observations near the zenith at a typical frequency like 65 MHz. It is a fan-beam with the above resolution in declination. The width of the east-west response pattern is nearly independent of frequency. Being very wide, it helps to observe a radio source continuously for $\gtrsim$7 h. A RG58U coaxial cable connected to the feedpoint near the top of the LPDA is used to transmit the radio frequency (RF) signal incident on the LPDA to the input of a low-pass filter with 3 dB cut-off at ≈85 MHz, followed by a high-pass filter with 3 dB cut-off at ≈35 MHz and a wideband amplifier with an uniform gain ≈30 dB in the frequency range 35-85 MHz. The two filters and the amplifier are kept near the base of the LPDA to minimize the length of the RG58U cable and hence the transmission loss. The high- and low-pass filters help to attenuate the unwanted signal at frequencies $\lesssim$30 MHz and $\gtrsim$85 MHz. The filtered and amplified signal from each LPDA is then passed via a cable delay unit (see the following paragraph). Subsequently, they are combined using two sets of 8-way power combiner followed by again a high-pass filter, low-pass filter and wideband amplifier as mentioned above.

As the array is oriented in the north-south direction, RF signal coming from an astronomical source whose declination is different from the local zenith (≈14° N) will be incident on each LPDA in the array at different instances of time. So, in order to coherently combine the signal from the different LPDAs, there is provision to include cable of appropriate length in the signal path from each LPDA in the array to compensate the aforesaid time delay. This allows the response pattern ('beam') of the each group of eight LPDAs to be 'phased' towards any desired declination in the range ≈−26° S to ≈+54° N. The limits are due to the HPBW of the LPDA along its E-plane and the local latitude mentioned earlier. The step interval in the cable delay unit corresponds to an angle of ≈3°, and the maximum angle to which the 'beam' of

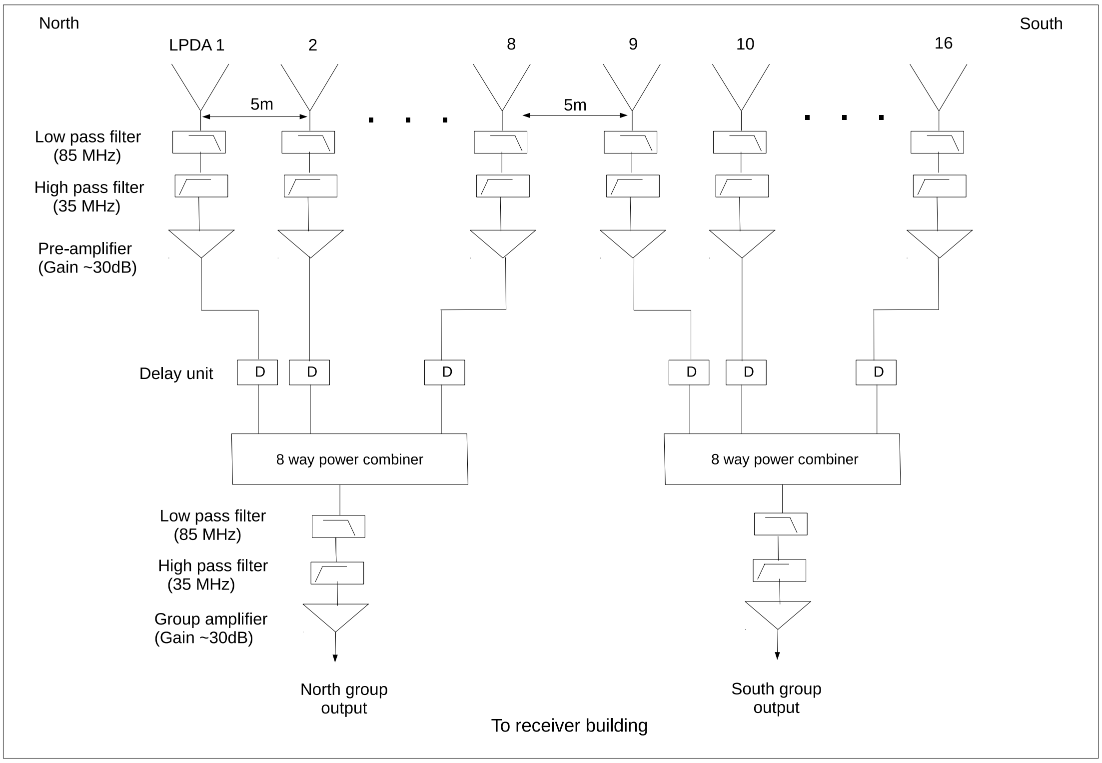

Figure 2.1: The array configuration and the front-end signal path.

the group of eight LPDAs could be 'phased' in the north-south direction is ≈45°. Note that the aforementioned minimum step interval in the delay unit results in a phasing error of ±1.5° (same as that for the 'beam' of the array in declination mentioned in the previous paragraph). It corresponds to a delay error of ±3 nsec for the total length of 35 m for the group of eight LPDAs (see Figure 2.1). We neglect this since it is small in general and also lesser than the minimum delay of ≈11 nsec that could be applied digitally in the present case (see Section 3). The combined output from each group of antennas are then transmitted to the receiver building (located ≈300 m away) via low-loss coaxial cables buried ≈1 m below the ground level to minimize possible diurnal variations in the characteristics of the cable. In order to compensate for the transmission losses during propagation, the RF signals from the two antenna groups are amplified in the receiver building. The outputs of the amplifiers are passed through 50 - 80 MHz bandpass filters to attenuate any spurious pick-up outside the band. Then the signals are fed to the input of the digital receiver.

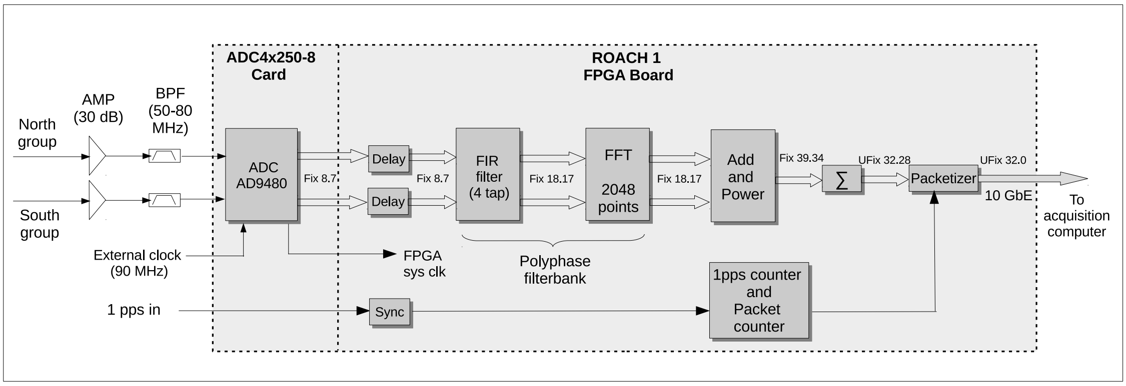

Figure 2.2: Schematic of the digital receiver system.

2.3 The Back-end Digital Receiver System

We have used a Field Programmable Gate Array (FPGA)* based digital spectrometer which converts the input voltage signal to its power spectrum using the Fast Fourier Transformation (FFT) technique. The spectrometer is implemented on Reconfigurable Open Architecture Computing Hardware (ROACH) from the Collaboration for Astronomy Signal Processing and Electronics Research (CASPER). The ROACH board hardware has Xilinx Virtex-5 FPGA†. Figure 2.2 shows the schematic of the digital receiver system used in the present case.

The RF signals corresponding to the two antenna groups in Figure 2.1 are connected to the input of an analog-to-digital converter (ADC). It is a quad-ADC containing four AD9480 ICs‡. We use two channels of the ADC for the present work. The ADC converts the input voltage to an 8-bit Fixed point number (Fix 8.7) between -1 and +1. Note that a linear relation between the input and output of the ADC for a large range of the input signal is important for any digital system. To check this in the present case, a broadband noise signal with provision to vary the input power level was connected to the input of the ADC. The output from the ADC were recorded for different levels of the input signal, and then processed offline to get the power spectrum using Fast Fourier Transformation (FFT). Figure 2.3 shows the results of the above test. The spectral power is linear for the input signal amplitude in the range $\approx$-42 dBm to $\approx$-4 dBm. This implies that the measured dynamic range (MDR) of the ADC is $\approx$38 dB. The effective number of bits (ENOB) = MDR/6.02 = 6.3 bits§. Note that for an 8-bit ADC, the expected dynamic range (EDR) and ENOB are $\approx 6.02 \times 8 = 48$ dB, and $\approx$7.3 bits¶, respectively. But these numbers are valid primarily for continuous

---

* https://www.xilinx.com/products/silicon-devices/fpga/what-is-an-fpga.html

† https://casper.astro.berkeley.edu/wiki/ROACH

‡ https://www.analog.com/en/products/ad9480.html

§ https://www.allaboutcircuits.com/technical-articles/understanding-the-dynamic-range-specificatio

¶ https://www.analog.com/media/en/technical-documentation/data-sheets/AD9480.pdf

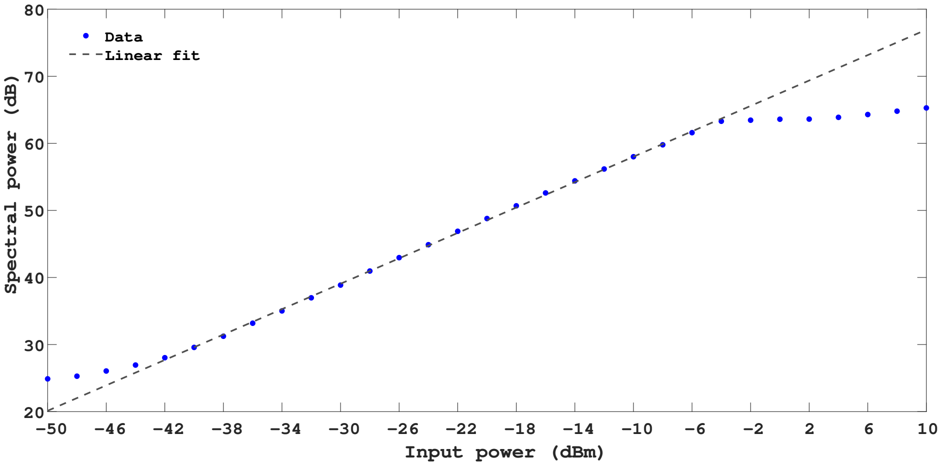

Figure 2.3: Results of the ADC linearity test.

wave (CW) signals at specific spot frequencies only.

We use a 90 MHz clock to sample the bandlimited RF signal of 50-80 MHz in the present case since the latter is in the 2nd Nyquist zone (45 - 90 MHz) of the aforementioned sampling frequency[‖]. Depending upon the declination of the source, appropriate delays are applied to the RF signal from either of the two groups in steps of 11.11 nsec to coherently combine the signals later. The corresponding delay error (i.e. ±5.5 nsec) limits the phasing of the north-south 'beam' of the array to ±2.3° with respect to the source declination. To obtain the power spectra of the RF voltage signals, the outputs from the delay units are processed using a combination of a finite impulse response (FIR) filter and FFT, together called a 'Polyphase filterbank' (PFB). Since the FFT is computed over finite number of samples, its response suffers from spectral leakage. But when a FIR filter with windowing function is used before the FFT, leakage into the adjacent spectral channels is considerably reduced (Price, 2018). In our design, a 4-tap FIR filter with Hamming window of 18-bit coefficients followed by 2048-points FFT is used. The latter has 1024 'positive' frequency bins. The total bandwidth sampled in the present case is 45 MHz as mentioned earlier. So, the frequency resolution is 43.945 kHz. To test the spectral leakage, CW signal at different frequencies (64.9 - 65.1 MHz in steps of 1 kHz) was fed to the input of the digital receiver in succession. An inspection of the test results (Figure 2.4) indicate that the isolation between adjacent frequency bins is ≈ -49 dB. The full-width at half-maximum (FWHM) of each frequency bin is ≈ 36 kHz. Note that the latter should have been ≈ 43.945 kHz as mentioned above. But due to the frequency response of the 4-tap PFB, the FWHM of each bin is reduced to ≈ 36 kHz. The isolation offered by a 4-Tap PFB (≈ 50 dB, see Figure 2.5) is sufficient for isolating spectral leakage.

[‖] `https://www.mikrocontroller.net/attachment/341426/Understanding_digital_signal_processing.pdf`

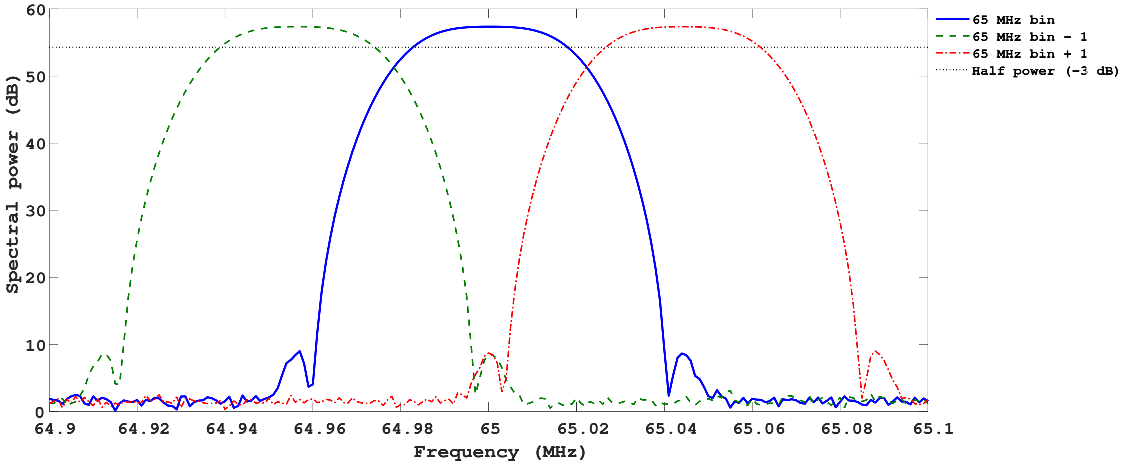

Figure 2.4: Spectral leakage test.

Note that increasing the number of taps in the PFB will improve the isolation. The main lobe response will be more flatter (see Figure 2.5 for a comparision between 4-tap and 8-tap PFBs). These are useful to carry out high precision timing studies of pulsars. But the possibilities of timing studies at low frequencies as in the present case are restricted since the pulse profiles are scatter broadened. Further, folded / average pulse profiles are only generated on most occassions. So a 4-tap PFB with Hamming window was used.

Note that the pulsar signal gets dispersed during its propogation through the ISM. The higher frequency components in the signal reach the observer earlier compared to the lower frequency components. Therefore the received signal needs to be de-dispersed to reconstruct the pulse. There are two types of de-dispersion methods: coherent and incoherent (Lorimer and Kramer, 2004). We use the incoherent de-dispersion technique as it is computationally easier[**]. The frequency resolution mentioned above allows finer correction for the dispersion, and also limits the possible leakage of the narrowband RFI to adjacent spectral channels. The PFB block output is 36-bit wide with 18-bit each for real and imaginary parts. The outputs corresponding to the two antenna groups are combined and squared to get the power spectrum (see Figure 2.6). The spectral data **are** then integrated for the desired duration. The output at this stage is 39-bit wide. The 10Gb Ethernet interface (see Figure 2.2) allows 64-bit data to be transmitted[††]. To facilitate the transfer, the aforementioned output is truncated to 32 bits by leaving 7 bits from the LSB (Least significant bit) and thereby making it easier to packetize the data in such a way that two data points are muxed together. Any degradation of the signal due to this trunca-

---

[**] http://www.ncra.tifr.res.in/ncra/gmrt/gmrt-users/low-frequency-radio-astronomy/ch17.pdf

[††] https://casper-toolflow.readthedocs.io/en/latest/src/blockdocs/Ten_GbE.html

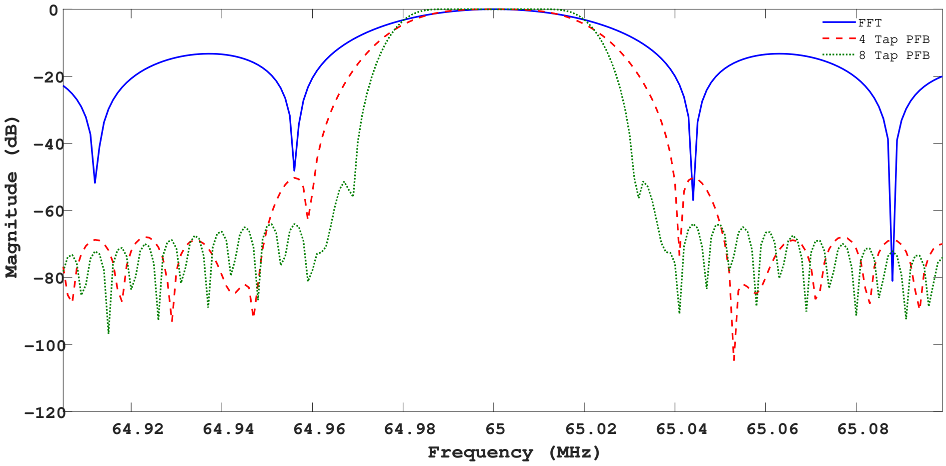

Figure 2.5: Spectral response of 4-tap and 8-tap PFB.

tion is expected to be minimal since the information content in the LSBs correspond primarily to noise fluctuations in the data only. The integrated output, which is now quantized to 32-bits unsigned number, is packetized with headers and sent to the data acquisition computer over 10 Gb Ethernet (see Figure 2.2). Each packet contains a standard UDP header, and custom header. The latter has observation details, 1 PPS (pulse per second) count, and a packet count. The 1 PPS signal is derived from a GPS clock (Trimble Thunderbolt E-GPS Disciplined clock)[‡‡] and given to the FPGA via the ADC card to generate the 1 PPS count. Packet count is a unique packet number assigned to each packet.

2.4 Data Processing Pipeline

The data acquired are first processed through a MATLAB based quick-look code for a quality check of the observation. The spectral response (see e.g. Figure 2.6) is plotted and inspected to ensure that the system performance was in order during the observation. The aforesaid code checks for any 'packet loss' that might have happened while writing the data to the hard disk of the acquisition computer. The 'packet loss' would give rise to gaps in the data stream which in turn affect the arrival times of the pulses leading to a lower signal-to-noise (S/N) for the observed pulsar. In extreme cases, it may not be possible to detect the pulsar when the data are folded. An unique number is assigned to each packet and the same is mentioned in the file header while writing the data. The packet number is used to assess 'packet loss'. If there are any, a new file is created by inserting zeros in the place of the lost packets to maintain continuity in the data stream. After the above processes, the data are converted

---

[‡‡] https://novotech.com/wp/wp-content/uploads/2022/11/Thunerbolt-E-GPS-Disciplined-Clock-Data-Sheet.pdf

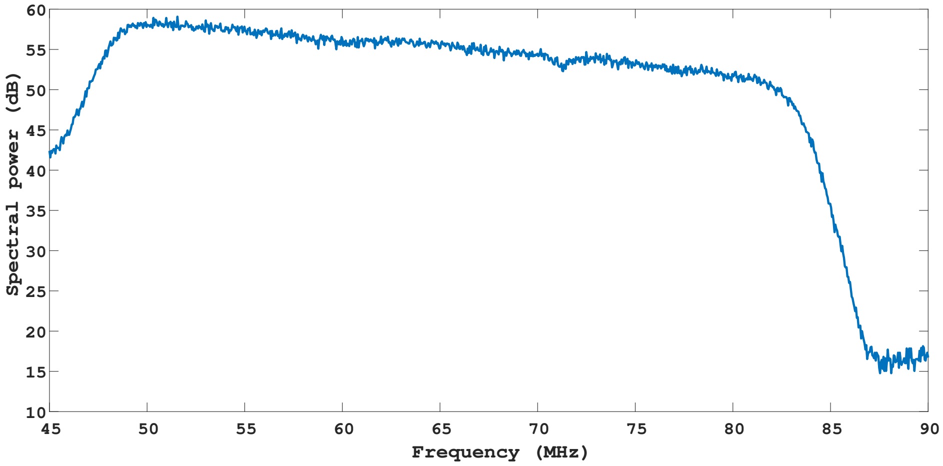

Figure 2.6: A sample power spectrum obtained from observations of the sky background.The amplitude variation (≈ 5 dB) across the 50 - 80 MHz range is due to a combination of the differential attenuation (as a function of frequency) in the coaxial cables used for the RF signal transmission, and the non-thermal spectral nature of the radio emission from the sky background. One could notice that RFI is very minimal as mentioned in Section 1.

to SIGPROC 'filterbank' format[§§] for further analysis using the Pulsar Search and Exploration Toolkit (PRESTO) (Ransom, 2011). The file is read using the 'readfile' tool and the meta-data are examined. RFI mitigation is performed using the 'rfifind' tool which searches for prominent RFI in the time-series as well as in the frequency domain, and creates 'mask' files. It also generates diagnostic files containing data statistics, identifies the time-domain statistical issues and marks them as RFI. The RFI 'masks' are used in the subsequent stages of data processing. Subsequently, the 'prepfold' tool is used to carry out folding and de-dispersion. It searches over a range of pulse periods and DM values to obtain the best fit for the corresponding parameters, i.e. the period and DM of the pulsar present in the observed data. Finally, the integrated pulse profile with the highest S/N is generated.

2.5 Trial Observations

We carried out observations of the sky background in the meridian transit mode to understand the characteristics of the antenna array and the receiver system. Figure 2.7 shows the observations carried out on 2021 June 30 at a typical frequency like 65 MHz. The bandwidth and integration time used were ≈ 30 MHz and ≈ 1 sec, respectively. The maximum in the observed emission was around ≈ 18^{h} Local Sidereal Time (LST) as expected (see e.g. Kraus, 1966; Kishore *et al.*, 2015). The duration of the observed profile (at the half maximum level) derived from the least squares fit is ≈ 9 h. This

---

[§§] `http://sigproc.sourceforge.net/sigproc.pdf`

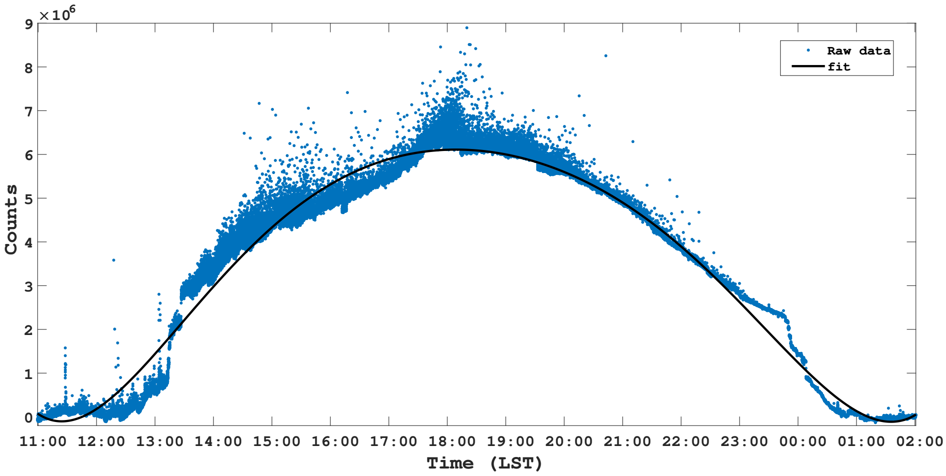

Figure 2.7: Observations of the sky background radiation with the pulsar array at 65 MHz with an integration time of ≈ 1 sec and bandwidth of ≈ 30 MHz. The source of peak emission at 18 LST is the galactic plane. RFI was very minimal during the observing period.

corresponds to an angular extent of ≈ 135°. Compared to this, the HPBW of the array pattern (in the east-west direction) is ≈ 110° (see Section 2). Note that the observed deflection in Figure 2.7 is primarily due to the intense patch of emission extending over the LST range ≈ 16 h - 21 h in any low frequency all-sky map (see e.g. Kraus, 1966; Dwarakanath and UdayaShankar, 1990). A convolution of the aforementioned region (angular extent ≈ 75°) with the array pattern (HPBW ≈ 110°) could give rise to ≈ 135° width for the observed profile (see e.g. Ramesh *et al.*, 2006, 2020).

Moving on to pulsar observations, we targeted the historical B1919+21 (J1921+2153) for our trial run. It is also located closer to the local zenith (≈ 14° N) in Gauribidanur. Some of the characteristics of this pulsar are (Bondonneau *et al.*, 2020): mean flux at 65 MHz ≈ 1.6 Jy, period = 1.337 sec, pulse width ≈ 0.104 sec, and DM ≈ 12.437 pc cm^{-3}. Note that the dispersive nature of the ISM causes smearing of the pulsar signal over a time $\mathrm{t_{smear}}$ which depends on the DM of the pulsar, frequency and bandwidth of observation (Issur, 2002). For the FWHM of the frequency bins mentioned earlier (≈ 36 kHz) and the frequency band of observation in the present case (i.e. 80 - 50 MHz), $\mathrm{t_{smear}}$ for B1919+21 will be in the range ≈ 5 - 34 msec. These values are well within the pulse period of B1919+21 (i.e. 1.337 sec). We observed the pulsar for a total duration of ≈ 2 h with an integration time of ≈ 4 msec. The north-south 'beam' of the array was 'phased' to the declination of the pulsar (21° N) for the observations (see Section 2). Figure 2.8 shows the results of our observations. The pulsar was detected with S/N ≈ 23. Comparing this with the mean flux of the pulsar, we find that the noise fluctuations should be ≈ 0.07 Jy. This is reasonably consistent with the estimated $\Delta \mathrm{S_{min}}$ (≈ 0.12 Jy) taking into consideration the above S/N and duty cycle (i.e. ratio of the width W of the pulse profile to its period P) of the pulsar to be ≈ 0.078

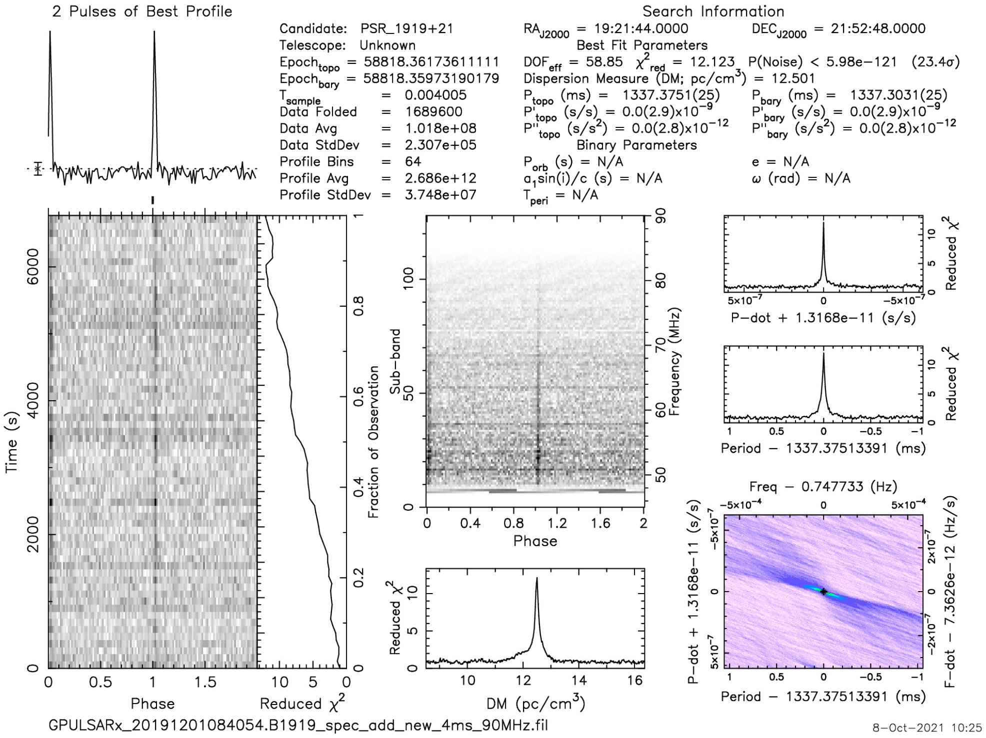

Figure 2.8: Observations of B1919+21 at 65 MHz with the pulsar array in the Gauribidanur observatory. The data were analysed using PRESTO. RFI was very minimal during the observing period. They were mitigated using the 'rfifind' tool in PRESTO (see Section 4).

(Bondonneau *et al.*, 2020). The other parameters used in the calculations are: total observing period ≈ 2 hr, $T_{sys} \approx 8500$ K at 65 MHz (Bondonneau *et al.*, 2020), bandwidth ≈ 30 MHz, and number of polarizations = 1. The above observational results from Figures 2.7 & 2.8 indicate that our observing system is well characterized. Note that for a total effective collecting area of ≈136 m^2 and an observing/integration period of ≈1 msec, the minimum detectable flux density of the system is ≈1 kJy. This is lower than the peak flux density (∼100 kJy) of the FRBs reported recently in the frequency range 400 - 800 MHz (The CHIME/FRB Collaboration, 2020). Assuming that the flux densities of the FRBs are expected to increase towards the lower frequencies (Keane *et al.*, 2016), similar detections as well as observations of giant pulses from the Crab nebula pulsar (Eftekhari *et al.*, 2016) are possible with our system. Subsequent to the detection of B1919+21, the pulsars B0950+08, B0834+06, and B1133+16 were also successfully observed with our system. The detection plots are shown in the Appendix E.

Further development is in progress to: (i) digitize the RF signal from individual antennas in the array. By applying different sets of delays while combining the signals, multiple beams can be formed to simultaneously observe different regions of the sky in declination. The array beam is already wide along RA (≈110°). By having several beams in declination (each ≈3° wide), a larger area of the sky can be monitored simultaneously. This can be useful for observations of FRBs; (ii) use Cross-polarized Log Periodic Dipoles (CLPD (Sasikumar Raja *et al.*, 2013)) and carry out polarization observations (see e.g. Noutsos *et al.*, 2015); (iii) use phase-coherent de-dispersion scheme with the DSPSR software package (Bhat *et al.*, 2018); (iv) increase the sampling frequency and thereby minimize the delay error relative to the source position (see Section 3); (v) use calibrated noise sources that can be switched into the signal path and/or routine observations of B1919+21 for calibration purposes. For polarization data, it is planned to use observations of radio transients from the Sun since some of them like type I bursts exhibit 100% circular polarization (McLean and Labrum, 1985).

2.6 Summary

We have presented the characteristics of the low frequency (50 - 80 MHz) observing system set up recently at the Gauribidanur observatory near Bangalore in India using Log Periodic Dipole Antennas (LPDAs), and the initial observations that were carried out. The LPDA offers several advantages, making it a popular choice for broadband applications. Its key strengths include wide frequency coverage, frequency-independent characteristics, and a relatively high directive gain. Additionally, LPDAs provide a large field of view and a significant effective collecting area, which are beneficial for applications requiring broadband sensitivity. However, at lower frequencies, LPDA designs become significantly larger, making their structural handling and mechanical support more challenging. The total collecting area of our array is smaller compared to the other radio telescopes like the LOFAR and LWA in the same frequency range but its large bandwidth (≈ 30 MHz), wide sky coverage (≈ 110°×80°), high spectral and temporal resolutions (≈ 36 kHz and 1 msec, respectively), geographical location (≈14° N), and the fact that the array is dedicated for time domain astronomy, are expected to be very useful to observe pulsars, radio bursts from the Sun (Ramesh *et al.*, 2003; Mugundhan, Hariharan, and Ramesh, 2017), and other high time resolution astrophysical phenomena like the FRBs. Due to the limited collecting area leading to low sensitivity, the Gauribidanur Pulsar System (GAPS), at present, can only observe high-fluence (bright) FRBs in the nearby universe. For example, to detect an FRB of duration 1 ms across 30 MHz bandwidth with SNR of ≈6 with the 16 antenna GAPS at 60 MHz, the flux of the burst has to be ≈5000 Jy.

Chapter 3

The mutltibeam system

Initial results from multi-beam observations of pulsars and solar transient with the digital beamformer for the Gauribidanur pulsar system
Kshitij S. Bane, Indrajit V. Barve, G. V. S. Gireesh, C. Kathiravan, R. Ramesh, 2023, **J. Astron. Telesc. Instrum. Syst.**,10(1) 014001.

3.1 Introduction

Multi-beam mode of observations in radio astronomy is a very useful technique since different regions of the sky covered by the primary 'beam' of the basic radio frequency (RF) signal receiving element (in either a single dish antenna or an array of dish/dipole antennas) could be observed simultaneously. This mode is particularly helpful for the study of transients like pulsars, Fast Radio Bursts (FRBs), etc. Low frequency dipole antennas have an inherent advantage in this connection since their primary signal receiving elements have comparatively larger field-of-view (FoV). Recent detections of FRBs at frequencies like ≈120 MHz (Pastor-Marazuela *et al.*, 2021) and ≈111 MHz (Pleunis *et al.*, 2021) suggest that they could be observable at frequencies <100 MHz also. Such observations are important to understand their spectral turn-over, scattering, etc. (Thorsett, 1991; Malofeev *et al.*, 1994; Bilous *et al.*, 2016; Zakharenko *et al.*, 2013; Karastergiou *et al.*, 2015; Geyer *et al.*, 2017; Bondonneau *et al.*, 2020; Sokolowski *et al.*, 2021). In the case of dipole antenna arrays at low frequencies, it is possible to digitize the signals from the individual antennas (see e.g. Taylor *et al.*, 2012). Any geometrical delays between the signals incident on the different antennas are digitally compensated in discrete steps of the reciprocal of the clock speed at which the signals are sampled. The response pattern ('beam') of the antenna array is effectively 'phased' (i.e. steered) to the desired region in the sky via this method. Such a digital beamforming setup reduces the hardware and hence the corresponding attenuation of the signal as compared to the analog beamformers where phase/delay cables controlled by diode switches are used to observe a particular direction of the sky at any given epoch (see e.g. Landecker, 1984; Ramesh *et al.*, 1998). Different lengths of phase/delay cables must be used in the latter to observe different regions of the sky. This introduces systematic gain variations. Furthermore, simultaneous observations are practically dificult. Once the beam is formed in a particular direction, observations will be restricted to that direction. But in a digital beamforming setup, where individual antenna signals are digitized and delays are applied in terms of delay units, multiple beams to simultaneously observe different directions could be formed (see e.g. Mol and Romein, 2011; Ng *et al.*, 2017). This can help in probing a large part of the sky at the same time, which is important in transient surveys.

The GAuribidanur Pulsar System (GAPS) is a recently commissioned prototype using log-periodic dipole antennas (LPDAs) for observations of the transients at low frequencies (Bane *et al.*, 2022). The antenna array has 16 Log-Periodic Dipole Antennas (LPDAs) arranged on a north-south baseline with spacing of 5 m between the adjacent antennas (Bane *et al.*, 2022). It was initially equipped with an analog beamformer network, but it has limitations as mentioned in the previous paragraph. These are common to any other similar analog hardware used elsewhere. Now, we have developed a digital beamformer unit for GAPS. Note that we used only 8 LPDAs in the GAPS for the present work since our aim is to understand the digital beamformer described in the present work for future use with the Gauribidanur RAdioheliograPH (GRAPH) which has 8 LPDAs per group (Ramesh, 2011; Ramesh *et al.*, 2014), and use GRAPH for dedicated observations of non-solar transients particularly during the local night time. Further, the analog-to-digital convertors available with us is limited to handle only up to 8 inputs. Note that the GRAPH is a T-shaped radio interferometer array consisting of 512 LPDAs. The individual arms of the array are oriented along the east-west and south directions. The effective collecting area of the array is ≈6400m^2 (at a typical frequency like 60 MHz) and the sky coverage is (≈8800 square degrees, independent of frequency). Both these parameters are significantly large, an important requisite for observations of non-solar transients. These characteristics, along with the prospects of dedicated and continuous observing period of ≈14 h everyday exclusively for non-solar transients suggests that GRAPH could be an useful instrument. Note that our plan is to upgrade and use GRAPH in the future for dedicated observations of the Sun from ≈7 AM (Indian Standard Time, IST) in the morning to ≈5 PM in the evening, and non-solar transients from ≈5 PM in the evening to ≈7 AM on the following day. This paper describes the prototype digital beamformer that we have developed for the GAPS subsequent to its commissioning, and the initial results based on simultaneous observations of a pulsar and transient radio burst emission from the solar corona. Such observations are important since it would help to calibrate the dynamic spectra of the latter and thereby infer the spectral index, emission mechanism, etc. which in some cases are still debated (see e.g. Ramesh *et al.*, 2013; Morosan *et al.*, 2016; Hariharan *et al.*, 2016; Vasanth *et al.*,

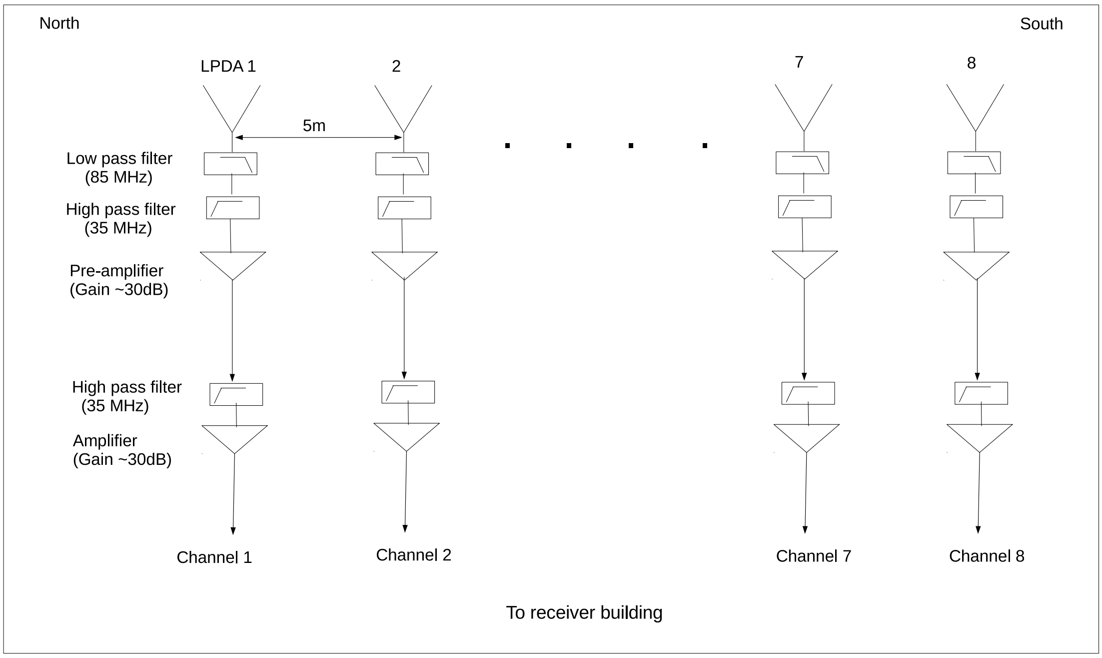

Figure 3.1: The array configuration for multibeam system

2019; Chhabra *et al.*, 2021; Liu *et al.*, 2022).

3.2 The Antenna and Front-end Analog Receiver System

The antennas used for this system are similar to the ones described in the Section 2.2. The 8 LPDAs are arranged on a north-south baseline with their H-plane in the east-west direction. The combined response pattern of the array is ≈110° in the east-west (hour angle) direction and ≈6° in the north-south (declination) direction for observations near the zenith at a typical frequency like 60 MHz. It is a fan-beam with the above resolution in declination. The width of the east-west response pattern is nearly independent of frequency. Being very wide, it helps to observe a radio source continuously for $\gtrsim$7 h. This is useful since mechanical steering is difficult for the dipole antennas used at low frequencies. LMR-200 coaxial cable[*] connected to the feedpoint near the top of the LPDA transmits the RF signal incident on the LPDA to the input of a low-pass filter with 3 dB cut-off at ≈85 MHz followed by a high-pass filter with 3 dB cut-off at ≈35 MHz, and then a wideband amplifier with an uniform gain ≈30 dB in the frequency range 35-85 MHz. The two filters and the amplifier are kept near the base of the LPDA to minimize the length of the LMR-200 cable and hence the transmission loss. The high- and low-pass filters help to attenuate the unwanted signal at frequencies $\lesssim$30 MHz and $\gtrsim$85 MHz which otherwise tends to saturate the

---

[*] https://timesmicrowave.com/wp-content/uploads/2022/06/lmr-200-datasheet.pdf

amplifier at times. The insertion losses of both the high-pass filter (HPF) and low-pass filter (LPF) are ∼0.1 dB each. Since the LPF and HPF are passive components, their contribution to the system's noise figure is equal to their insertion loss, i.e., 0.1 dB each. However, the low-noise amplifier (LNA) in our system has a noise figure of 3 dB, which is significantly larger and dominates the overall noise performance. Thus, while the insertion losses of the filters do have a minor effect on the system noise figure, their contribution is negligible compared to the LNA. The overall system noise figure remains largely dictated by the LNA's characteristics. The amplified output corresponding to each LPDA is then transmitted to a central cabin near the center of the array where they are again high-pass filtered and amplified. Note that the 2nd high-pass filter in the signal chain is to further suppress the local radio frequency inteference (RFI) at $\lesssim$30 MHz. The RF signals are then transferred to the receiver building (located ≈300 m away) independently via eight separate, low-loss LMR-400 coaxial cables[†] of identical RF characteristics. The lengths of all the cables are the same and they were also phase equalized. The cables are buried ≈1 m below the ground level to minimize possible diurnal variations in their characteristics.

3.3 The Back-end Digital Receiver System

In order to compensate for the transmission losses during propagation from the antenna end, the RF signal from each LPDA are once again amplified in the receiver building. Each amplifier in this stage is preceded by a surge protector to safeguard the digital receiver. Subsequent to amplification, the signal corresponding to each LPDA is passed through a bandpass filter to limit the frequency coverage to ≈50 - 70 MHz band. As the array is oriented in the north-south direction, the RF signal coming from an astronomical source with a declination that is different from the local zenith (≈14° N) will be incident on each LPDA in the array at different instances of time. So, to coherently combine the signal from the eight LPDAs, appropriate delay must be introduced in the required signal paths as mentioned in the previous section. This is done in the digital backend receiver. We have used a Field Programmable Gate Array (FPGA)[‡] based digital spectrometer which converts the input voltage signal to its power spectrum using the Fast Fourier Transformation (FFT) technique. The spectrometer is implemented on Reconfigurable Open Architecture Computing Hardware (ROACH) from the Collaboration for Astronomy Signal Processing and Electronics Research (CASPER). The ROACH board hardware has Xilinx Virtex-5 FPGA[§]. Here, several beams (up to ten beams for our system configuration) could be formed to simultaneously observe different regions in the sky based on the delay

---

[†] https://timesmicrowave.com/wp-content/uploads/2022/06/lmr-400-datasheet.pdf

[‡] https://www.xilinx.com/products/silicon-devices/fpga/what-is-an-fpga.html

[§] https://casper.astro.berkeley.edu/wiki/ROACH

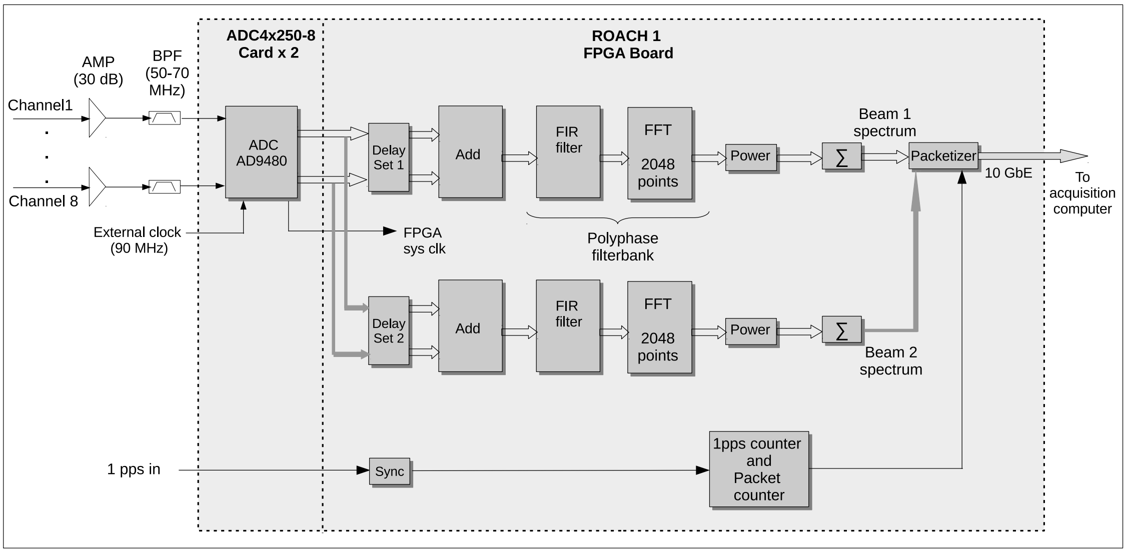

Figure 3.2: Schematic of the digital receiver multibeam system.

values applied to RF signals from the different antennas before combining them.

Figure 3.2 shows the schematic of the digital receiver system to form two simultaneous beams. The RF signals corresponding to the eight LPDAs in Figure 3.1 are connected to the input of two analog-to-digital converter (ADC) cards. These are quad-ADC boards, each containing four AD9480 ICs[¶]. The ADC converts the input voltage to an 8-bit Fixed point number (Fix 8.7) between -1 and +1. A 90 MHz clock is used to sample the bandlimited RF signal of ≈50 - 70 MHz band. The sampled band lies in the second Nyquist zone of 90 MHz sampling. Copies of sampled signals from the eight channels are generated and passed through two different sets of delay (one for each beam position) as shown in Figure 3.2. Depending on the declinations to which the different beams are pointed, delay values are calculated using the equation $\frac{d sin\theta}{c}$ (Kraus, 1966). Here d is the baseline distance between the reference LPDA for the delay calculations and the LPDA in whose signal path delay has to be introduced, c is the velocity of light, and θ is the angle between the source direction and the normal to the baseline. The minimum delay value that can be applied in the signal paths from each of the 8 LPDAs in the present case is ≈11.11 ns. Higher delay values are compensated by introducing multiple steps of 11.11 ns delay, as per the requirement. So, there can be a maximum uncompensated delay of $\Delta t = \pm 5.5$ ns. This applies for sources located at all declinations within the FoV of GAPS along the declination (i.e. ≈26° S - 54° N), except the local zenith (14° N) for which no delay compensation is needed. Note that similar to the maximum uncompensated delay, the minimum un-

---

[¶] https://www.analog.com/en/products/ad9480.html compensated delay also varies with the declination and it is a non-zero value. The uncompensated fractional delays give rise to phase errors ($2\pi f \Delta t$, where f is the frequency of observation) for LPDA 2 to LPDA 8 with respect to the reference LPDA 1 for the delay/phase calculations. For the aforesaid maximum possible delay error of $\approx\pm5.5$ ns, the differential phase error over the observing frequency band of 50 - 70 MHz in the present case is $\approx36°$. The different phase errors at different frequencies in the observing band can be corrected by applying phase gradients[‖] during signal processing. But we could not implement such a correction scheme in the present design due to limited resources on the FPGA board. So, there will be bandwidth decorrelation for declination angles other than $\approx14°$ N in view of this. For the 20 MHz bandwidth in the present case, the decorrelation will be in the range $\approx$0 - 2% depending on the value of Δt. The digitised voltages are added and processed using a Polyphase FilterBank (PFB) (Price, 2018). The PFB is a combination of Finite Impulse Response (FIR) filter and Fast Fourier Transformation (FFT). In our design, a 4-tap FIR filter with Hanning window of 18-bit coefficients followed by 2048-points FFT is used. The FFT gives 1024 'positive' frequency bins which give a frequency resolution of $\approx$43.945 kHz. The output of the PFBs are squared to obtain the power spectra which are then temporally integrated depending on the observational requirement. The integrated power spectra corresponding to the two beams are packetised together and transmitted to the data acquisition computer over 10 Gigabit ethernet. Figure 3.3 shows an example of the instantaneous power spectrum in the digitized band of $\approx$50 - 70 MHz. The data were obtained with an integration time of $\dot{a}pprox4$ msec for two different beam positions ($\approx26°$N and $\approx2°$N) in declination. The responses obtained indicate that the two different sub-units of the digital receiver chain (see Figure 3.2) are working satisfactorily.

3.4 Observations

We carried out trial observations of the sky background in the meridian transit mode with the two beams pointed at two different directions (declinations) of the sky to understand the characteristics of the antenna array and the receiver system. Figure 3.4 shows the results of the test at a typical frequency of 60 MHz when one beam was pointed to $\approx12°$ north of the local zenith and another one to $\approx12°$ south of the local zenith. The corresponding declinations are $\approx26°$N and $\approx2°$N, respectively. The bandwidth and integration time used were $\approx$0.1 MHz and $\approx$1 s, respectively. The observed deflection shown in Figure 3.4 is primarily due to the intense patch of emission from the Galactic plane that could be noticed in any low frequency all-sky map (see e.g. Kraus, 1966; Dwarakanath and UdayaShankar, 1990). The maximum in the observed

---

[‖] `http://www.ncra.tifr.res.in/ncra/gmrt/gmrt-users/low-frequency-radio-astronomy/ch17.pdf`

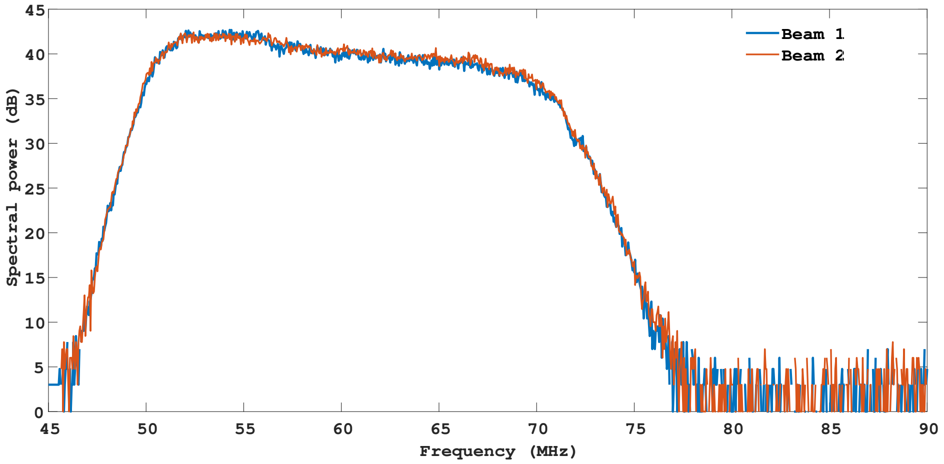

Figure 3.3: Sample power spectra obtained from observations of the sky background with two simultaneous beams pointed to ≈26°N and ≈2°N in declination (i.e. $\approx +12°$ to the north and south of the local zenith declination, respectively).

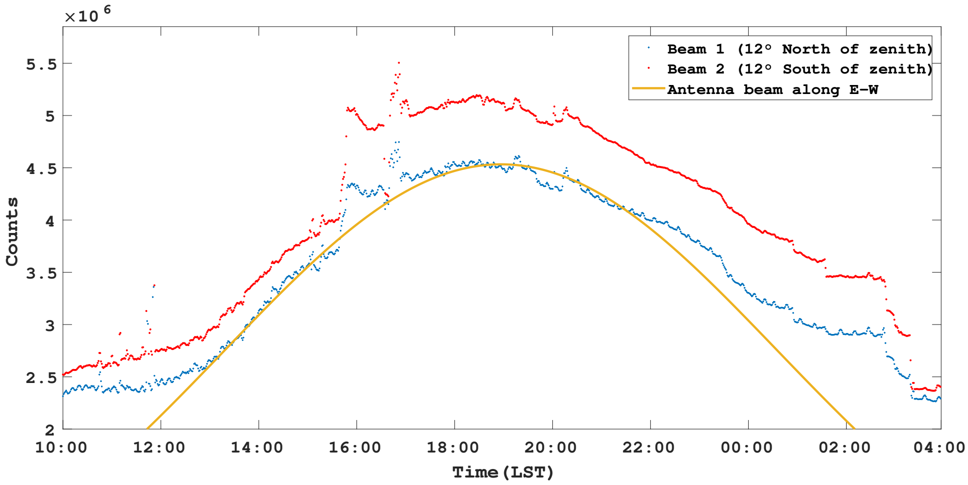

Figure 3.4: Observations of the Galactic plane at 60 MHz on 2022 August 13 with two simultaneous beams pointing at ≈26°N and ≈2°N in declination (i.e. $\approx +12°$ to the north and south of the local zenith declination, respectively). The sudden jumps in the observed amplitude counts near ≈15:00 and 03:00 LST are due to disruptions in the receiver power supply. The expected beam pattern is shown in 'orange' colour. It is scaled to the peak amplitude count of the 'blue' colour profile.

emission is around $\approx 18^{\mathrm{h}}$ Local Sidereal Time (LST) as expected (see e.g. Kraus, 1966) The beam pointing at ≈2°N declination shows ≈1.2 times higher amplitude count. A higher count is likely because it is closer to the Galactic center (declination ≈29° S) as compared to the other beam pointing at ≈26°N declination. We verified this by comparing the sky background temperatures in the two directions from the low frequency all-sky maps available in the literature and scaling them to 60 MHz using spectral index of -2.55 (Kraus, 1966; Haslam *et al.*, 1982; Marsh, 1992). Note that the two beams formed are symmetric about the local zenith in this case. So, any gain differences due to the primary antenna beam are expected to be very minimal. Both the observed profiles as well their HPBWs are consistent with the expected east-west beam pattern of the GAPS (shown in orange colour in Figure 3.4).

Figures 3.5 & 3.6 show the results of the simultaneous two-beam observations on 2022 December 7 when one of the beams was pointed in the direction of the pulsar B1919+21 (≈22°N declination), and the other beam was pointed in the direction of Sun whose declination was ≈23°S on that day (≈45° away from the pulsar B1919+21 in declination). The time profiles shown correspond to observations over the frequency range ≈62.5 - 65.0 MHz. The pulsar profile in Figure 3.5 was extracted after processing the data obtained over the full 50 - 70 MHz band using the standard PulsaR Exploration and Search TOolkit (PRESTO) (Ransom, 2011). Figure 3.7 shows the corresponding plot for the pulsar B1919+21. The SNR of the pulsar is ≈7. We had earlier reported similar detection of the pulsar B1919+21 with the previous version of GAPS. The SNR was ≈23 in that observations (Bane *et al.*, 2022). The reduced SNR in the present case is due to a combination of lesser collecting area (8 LPDAs as compared 16 LPDAs), and smaller bandwidth (20 MHz as compared to 35 MHz). The expected SNR with the above changes is ≈8.5. The aforementioned observed SNR (≈7) is in good agreement with this. This indicates that any errors due to the uncompensated fractional delays and/or phase gradients (see Section 3) are minimal in these observations. A type III radio burst from the Sun was reported around ≈08:48 UT (≈18:52 LST) that day[**], and we could observe the same with GAPS (see Figure 3.6). The event was independently observed with the solar radio spectrographs in Gauribidanur also (Kishore *et al.*, 2015; Kumari *et al.*, 2017). For the solar data observed with GAPS, we carried out single pulse search using PRESTO. A range of dispersion measure (DM) values from 0 - 20 $\mathrm{pc\,cm^{-3}}$ were applied in steps of 0.2 $\mathrm{pc\,cm^{-3}}$. The maximum SNR was obtained for DM ≈6.6 $\mathrm{pc\,cm^{-3}}$. Note that nearly equal DM (≈5.5 $\mathrm{pc\,cm^{-3}}$) was reported for the solar burst observed earlier with the Survey for Transient Astronomical Radio Emission 2 (STARE2) instrument in the frequency range ≈1.28 - 1.46 GHz (Bochenek *et al.*, 2020b).

The flux density of the pulsar B1919+21 at 65 MHz is ≈1.6 Jy (Bondonneau *et al.*, 2020). The SNR of the pulsar in the present observations (Figure 3.5) is ≈2.5. Note that this is for the average pulse profile over the frequency range ≈62.5 - 65 MHz and total observing period of 2 hrs. The corresponding SNR For the full observing bandwidth, i.e. 50 - 70 MHz, is ≈7. The ratio of the two SNR values is ≈2.8. This is consistent with the square root of of the ratio of the two bandwidths, i.e. $\sqrt{20/2.5}$, as expected. We would like to add that since the pulsar profile in Figure 3.5 is averaged over a longer integration time, its flux is assumed to be the mean value. Upon comparing the SNR of the solar burst in Figure 3.6 with that

---

[**] `https://ftp.swpc.noaa.gov/pub/warehouse/`

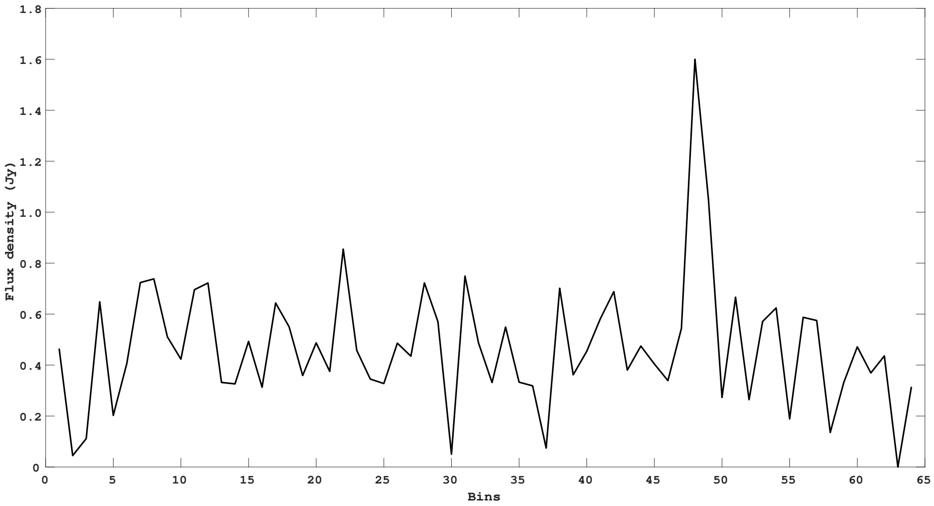

Figure 3.5: Observations of the pulsar B1919+21 (J1921+2153, in J2000 coordinates) with 8-elements GAPS on 2022 December 7 over the frequency interval ≈62.5 - 65.0 MHz using the digital beamformer network described in Section 3. The time profile is over one period of the pulsar, i.e. 1.337 sec.

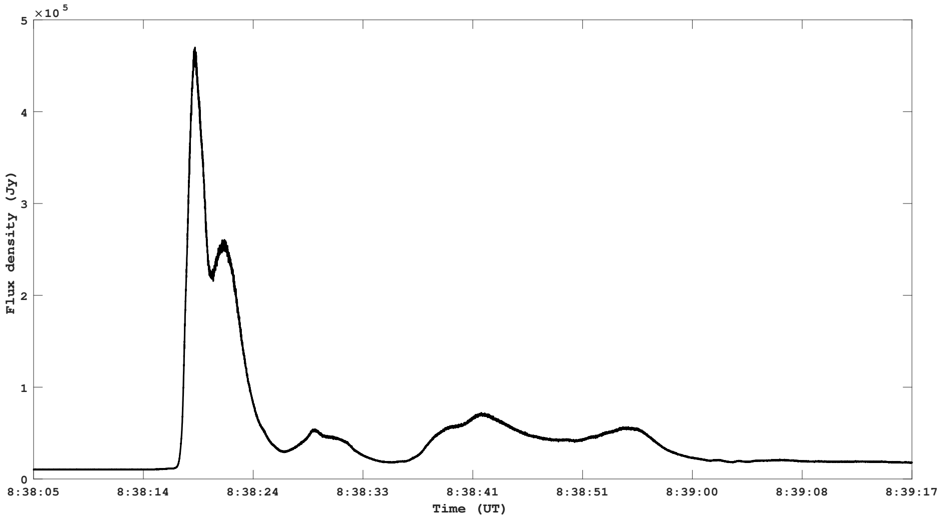

Figure 3.6: Time profile of the type III solar radio burst observed simultaneously along with the pulsar B1919+21 (see Figure 3.5) on 2022 December 7 over the frequency interval ≈62.5 - 65.0 MHz. The declination of Sun during the above epoch was ≈23°S as compared to ≈22°N for the pulsar. The Right Ascension (R.A.) of Sun was $\approx 16^{\mathrm{h}}54^{\mathrm{m}}$.

of the pulsar B1919+21 (after taking into consideration the number of folds and percentage of useful data in the case of the latter), we estimated the flux density of the type III solar burst in Figure 3.6 to be ≈4.7e5 Jy. This is consistent with the published values of the flux densities of the type III bursts from single frequency

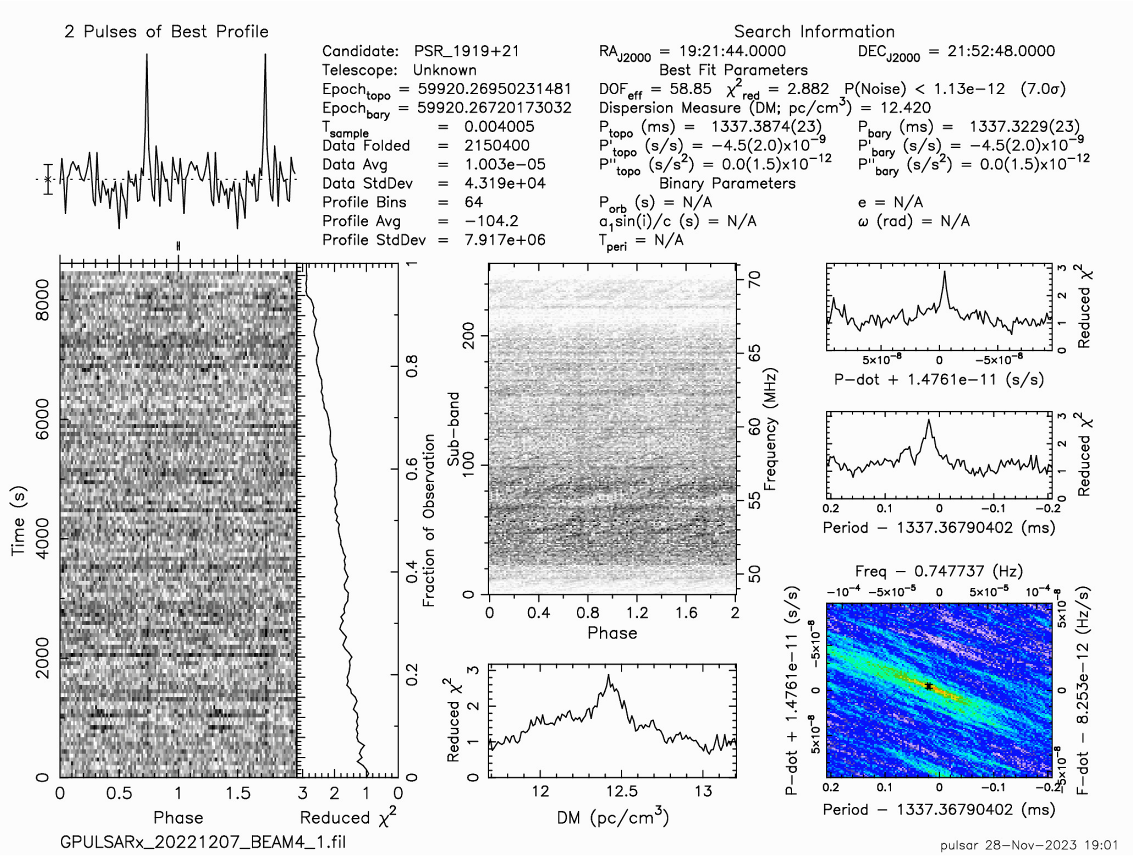

Candidate: PSR_1919+21

Telescope: Unknown

$\mathrm{Epoch_{topo}}$ = 59920.26950231481

$\mathrm{Epoch_{bary}}$ = 59920.26720173032

$\mathrm{T_{sample}}$ = 0.004005

Data Folded = 2150400

Data Avg = 1.003e−05

Data StdDev = 4.319e+04

Profile Bins = 64

Profile Avg = −104.2

Profile StdDev = 7.917e+06

Search Information

$\mathrm{RA_{J2000}}$ = 19:21:44.0000 $\mathrm{DEC_{J2000}}$ = 21:52:48.0000

Best Fit Parameters

$\mathrm{DOF_{eff}}$ = 58.85 χ^2_{red} = 2.882 P(Noise) < 1.13e−12 (7.0σ)

Dispersion Measure (DM; pc/cm^3) = 12.420

$\mathrm{P_{topo}}$ (ms) = 1337.3874(23) $\mathrm{P_{bary}}$ (ms) = 1337.3229(23)

$\mathrm{P'_{topo}}$ (s/s) = $-4.5(2.0)\times10^{-9}$ $\mathrm{P'_{bary}}$ (s/s) = $-4.5(2.0)\times10^{-9}$

$\mathrm{P''_{topo}}$ (s/s^2) = $0.0(1.5)\times10^{-12}$ $\mathrm{P''_{bary}}$ (s/s^2) = $0.0(1.5)\times10^{-12}$

Binary Parameters

$\mathrm{P_{orb}}$ (s) = N/A e = N/A

$a_1\sin(i)/c$ (s) = N/A ω (rad) = N/A

$\mathrm{T_{peri}}$ = N/A

Figure 3.7: Observations of the pulsar B1919+21 (J1921+2153)with GAPS on 7 December 2022 in the frequency range 50 - 70 MHz for a period of ≈2 h. The data were analyzed using PRESTO.

observations at nearby frequencies (Ramesh *et al.*, 2003, 2005). We carried out similar comparison over successive frequency bins in the entire frequency range (50 - 70 MHz) of observations also, and calculated the flux densities of the solar burst at different frequencies. The spectral index of the burst estimated from the above results is ≈-2.7. This is consistent with the mean spectral index of the type III bursts in the similar frequency range (Mugundhan *et al.*, 2018). Figure 3.8 shows the de-dispersed dynamic spectrum of the type III burst described above. It was obtained using PRESTO. Due to the better sensitivity of GAPS, faint emission beyond the main phase of the burst (indicated by the dotted lines in the upper panel of Figure 3.8) could be also clearly observed. Similar sensitive observations are expected to be useful in exploring hitherto rarely observed transient emission from the Sun at low frequencies (see e.g. Ramesh and Ebenezer, 2001; Sharma *et al.*, 2022; Kansabanik, Mondal, and Oberoi, 2023). We also carried out observations of the pulsars B0834+06 and B0950+08 in the simultaneous two-beam mode. The two pulsars are separated by ≈2° in declination. Two separate beams were formed towards the direction of the two pulsars so that the beam gains are equal and maximum in both the directions.

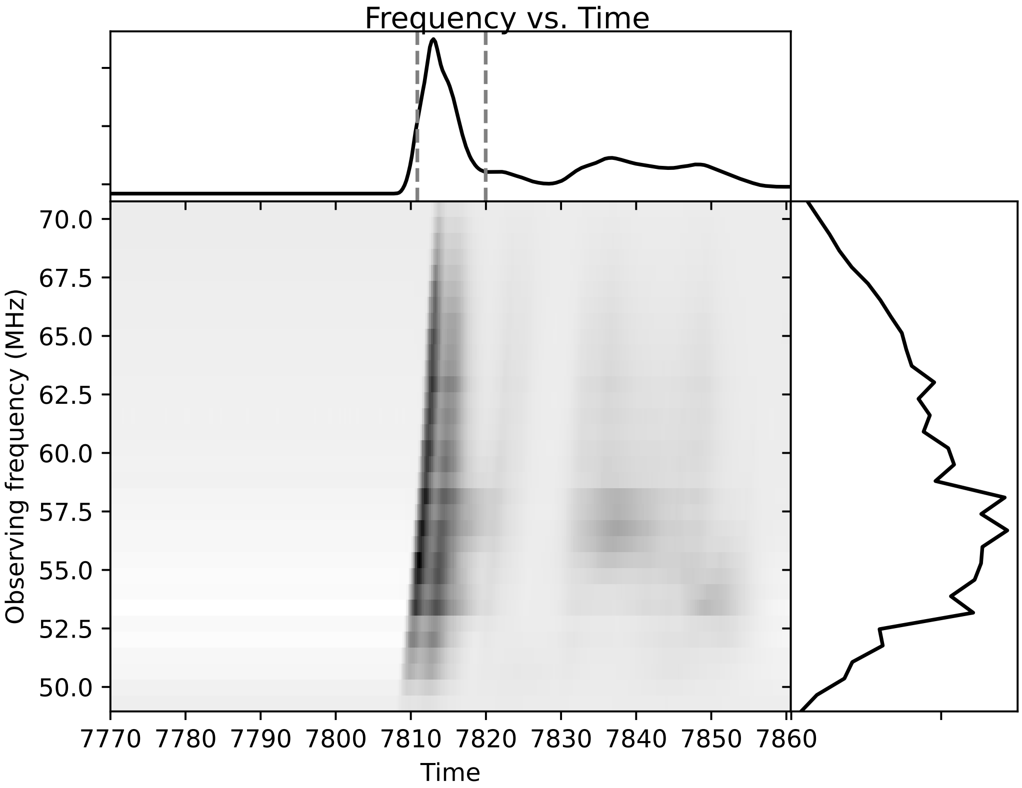

Figure 3.8: De-dispersed dynamic spectrum (50 - 70 MHz) corresponding to the solar radio burst in Figure 3.6. The DM used was ≈6.6 pc cm^{-3}. Time in the x-axis starts from ≈08:37:35 UT, and the interval is 10 sec. The upper panel show the spectrally averaged time profile of the burst. The right side panel shows the temporally averaged spectral profile of the burst. The dotted lines in the upper panel indicates the main phase of the burst.

The total duration of the observation was ≈5 h centered at ≈09:30 LST. The results are shown in Figures 3.9 & 3.10, respectively. The SNR values of the detected pulse profiles are ≈12 & 5, respectively. Their ratio (i.e. SNR of the pulsar B0834+06 to the SNR of the pulsar B0950+08 is ≈2.6. The corresponding ratio derived from the earlier observations is ≈2.2 (Bondonneau *et al.*, 2020). The reasonable consistency between the two estimates indicates that the digital beamformer in the present case is functioning satisfactorily despite the bandwidth decorrelation problem mentioned in Section 3. We would like to point out here that the heights of the components in the profile of the pulsar B0950+08 seem to be reversed when compared with observations at similar frequencies (see e.g. Bondonneau *et al.*, 2020). The possible reasons for this apparent difference could be: (i) 'noisy' average pulse profile of the pulsar B0950+08; (ii) fewer data points in the on-pulse profile. The time resolution in our observations is ≈4 ms whereas the average pulse width is ≈30 ms.

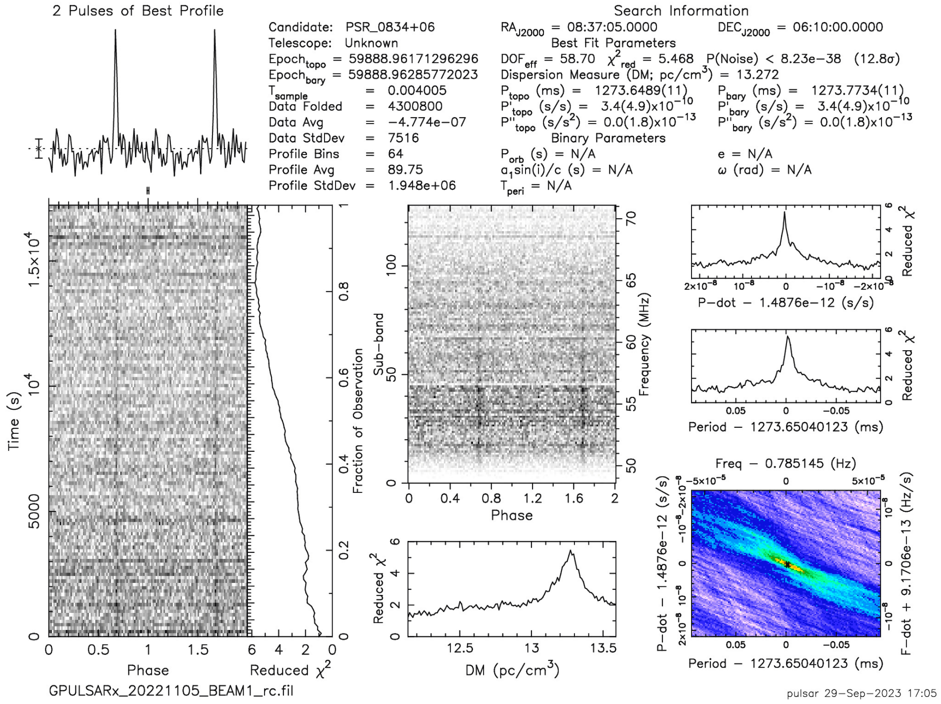

Figure 3.9: Observations of the pulsar B0834+06 (J0837+0610) with GAPS on 5 November 2022 in the frequency range 50 - 70 MHz for a period of ≈4 h.

Table 3.1: Parameters of the pulsars detected.

Pulsar	**Period (s)**	**DM (pc/cm^3)**	**Flux (Jy)** (Bondonneau *et al.*, 2020)
B1919+21	1.3373	12.420	1.6
B0834+06	1.2736	13.272	1.2
B0950+08	0.253	2.59	2.2

3.5 Summary

We have described the digital beamformer developed recently for the GAPS, and trial observations of two radio sources (Sun and a pulsar, located at different declinations in the sky) at the same time. Simultaneous observations of two pulsars have also been presented (see Table 1 for the parameters of the three pulsars reported in the presented work.) The wide sky coverage (≈110°×80°) of GAPS and the fact that the array is dedicated for time domain astronomy are very useful in this connection since simultaneous multi-beam observations of widely separated regions of the sky could be planned and carried out within a short interval of time. This is an essential

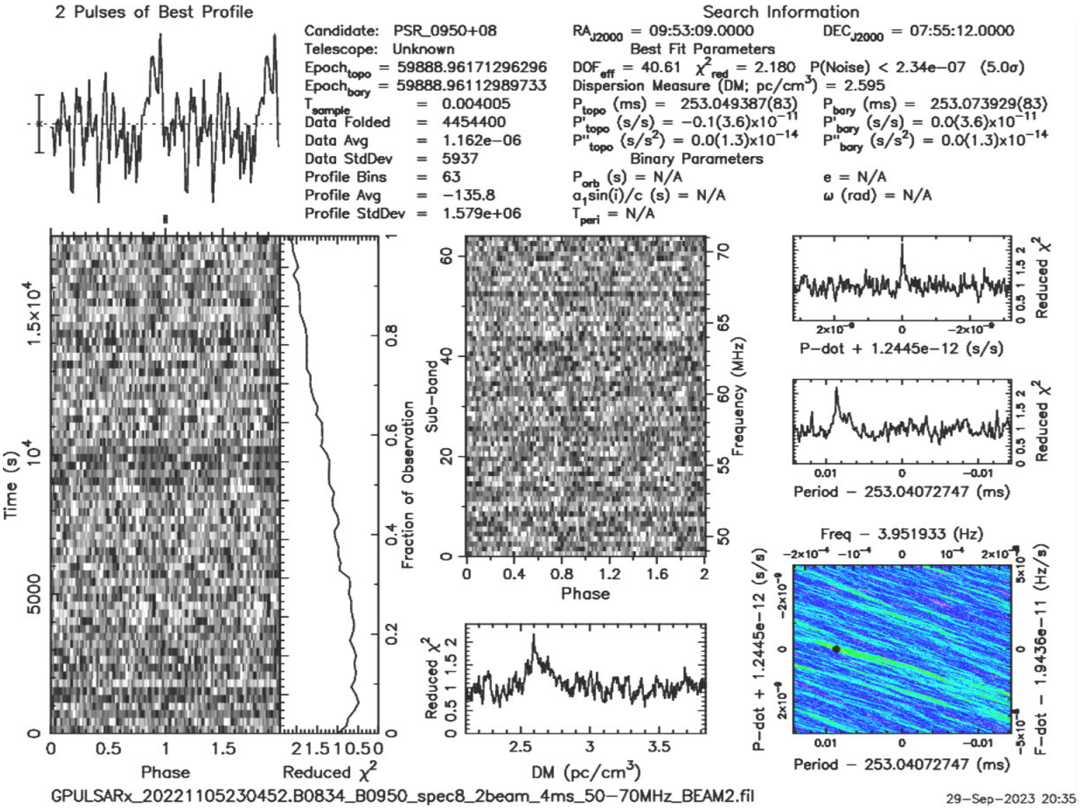

Figure 3.10: Observations of the pulsar B0950+08 (J0953+0755) with GAPS on 5 November 2022 in the frequency range 50 - 70 MHz for a period of ≈4 h.

requirement to record shortlived (∼ msec) astrophysical phenomena like the FRBs. Considering the expected rate of detectable FRBs (Champion *et al.*, 2016) and other short duration bursts, there is scope for new detections even with small and dedicated telescopes/antenna arrays (Saint-Hilaire, Benz, and Monstein, 2014; Bochenek *et al.*, 2020a) particularly with multi-beam observing capability. In the case of solar observations, the multi-beam observations are expected to be specifically useful to calibrate the spectra of radio bursts from the Sun in a relatively easier manner (for example, via simultaneous observations of a pulsar with known and established characteristics). The detection of the solar burst using the single pulse search mode in the present case indicates that our antenna/receiver systems and the data processing pipeline could also alternatively detect other bright transient emission like the FRBs also, should they occur. Currently work is in progress to save the digitized raw voltages from the individual antennas in the GAPS. It will help to observe/search any desired region of the sky (within the primary beam of the LPDA used in the array) in both real time as well as archival data unlike the present digital beamformer where appropriate delays are introduced in the signal path prior to the observations and that too for pre-determined locations in the sky. So any possible search for transients in different locations is difficult. This problem would not be there if the raw voltages from each antenna are independently digitized. But the data rate/volume is expected to be very high. So we intent to use limited number of bits. It is planned to use either or combination of these two techniques (i.e. digital beamformation as mentioned in the present work or the digitization of raw voltages with few bits) in the GRAPH so that it could be used for observations of non-solar transients during the night in addition to its continued operation as a dedicated solar observing instrument during the day.

Chapter 4

The raw voltage recording system

1-bit raw voltage recording system for dedicated observations of transients at low radio frequencies
Kshitij S. Bane, Indrajit V. Barve, G. V. S. Gireesh, C. Kathiravan, R. Ramesh, 2024, **ApJS** 272 27

4.1 Introduction

Latest advancements in commercial technology help to directly digitize the radio frequency (RF) signals in radio astronomy observations and record them as sampled voltages. Traditionally, a receiver architecture includes one or several mixer stages performing down-conversion from RF to an intermediate or baseband frequency, due to limited analog-to-digital (ADC) sampling rate. However, in pace with technology development, increased ADC performance allows for higher sampling rates. The higher the sampling rate, the higher the frequency that can be sampled for a correct read, thereby allowing sampling at either the observation frequency itself or a higher intermediate frequency. Accordingly, at a sufficiently high sample rate there would be no need for down-conversion. Eliminating the need of a mixer stage is advantageous, since mixers in practice raise system challenges, such as introducing frequency offsets. In addition to minimizing the number of analog components in the receiver system and thereby the associated amplitude/phase variations, the direct digitization offers more flexibility particularly in the efforts to search for radio transients at low frequencies where the individual dipole antennas have wider instantaneous sky coverage. For example, in the multi-beam setup where beams are formed on-board digital hardware like a FPGA, the number of beams is limited by the resources available on the FPGA. Also, once the beams are formed in certain directions, the observations are limited to the corresponding directions. On the contrary, if raw voltages from each antenna are recorded, any number of beams can be formed offline to probe any desired set of directions in the sky within the field-of-view (FoV) of the individual antenna. Therefore, it is advantageous to have a voltage recording capability. A high sampling rate and high resolution ADC accordingly approaches an accurate read of an incoming signal, seemingly preferable. However, the energy consumption at high sampling frequencies increases with the number of quantization levels*. Furthermore, the resulting data volumes and subsequent data processing/management will be enormous in such a system. One solution to these is to record fewer number of bits from analog-to-digital converters connected to each antenna element. Data rates and volumes can be significantly reduced if 1-bit (sign bit) digital receivers are employed. 1-bit digital correlators have been used in radio astronomy (see e.g. Weinreb, 1963; Udaya Shankar and Ravi Shankar, 1990; Nakajima *et al.*, 1994; Ebenezer *et al.*, 2001; Ramesh *et al.*, 2008; Zakharenko *et al.*, 2016). The present work describes a 1-bit raw voltage capture system that we have implemented in GAPS to demonstrate how such a system could be useful for observations of pulsars and other transients at low radio frequencies.

4.2 The antenna and analog receiver system

GAPS is a recently commissioned prototype using LPDAs for observations of the transients in the frequency range ≈50 - 80 MHz. The antenna array has 16 LPDAs arranged on a north-south baseline with spacing of 5 m between the adjacent antennas (Bane *et al.*, 2022). For the present work, we used only 8 LPDAs similar to the configuration as described in Section 3.2 of Chapter 3.

The array was initially equipped with an analog beamformer network (see Section 2.2) where phase/delay cables controlled by diode switches were used to observe a particular direction of the sky at any given epoch (see e.g. Landecker, 1984; Ramesh *et al.*, 1998). Different lengths of phase/delay cables must be used in the latter to observe different regions of the sky. This introduces systematic gain variations. Furthermore, simultaneous observations are practically difficult. Once the beam is formed in a particular direction, observations will be restricted to that direction. These are common to any other similar analog hardware used elsewhere. We used only eight LPDAs in GAPS for this study because our primary goal was to understand the digital beamformer described here. This understanding will be useful for future applications with the Gauribidanur Radioheliograph (GRAPH), which also employs eight LPDAs per group (Ramesh, 2011; Ramesh *et al.*, 2014). We plan to use GRAPH for dedicated observations of non-solar transients, particularly during local nighttime. Note that the GRAPH is a T-shaped radio interferometer array consisting of 512 LPDAs. The individual arms of the array are oriented along the east-west and south directions. The effective collecting area (A_e) of the array is ≈6400m^2 at a typical frequency like 60 MHz. The sky coverage is ≈8800 square degrees, independent of

---

*`https://github.com/bmurmann/ADC-survey`

frequency. Both these numbers are reasonably larger, an important requisite for observations of non-solar transients. For comparison, the fully completed NenuFAR in France is expected to have $A_e \approx 20000 m^2$ and sky coverage ≈100 square degrees, at 60 MHz[†]. The corresponding numbers for LOFAR which is currently operational are $A_e \approx 9600 m^2$ and sky coverage ≈19600 square degrees, at 60 MHz (van Haarlem *et al.*, 2013). The aforementioned characteristics of GRAPH, along with the prospects of dedicated and continuous observing period of ≈14 h every day exclusively for non-solar transients suggests that GRAPH could be an useful instrument. Additionally, the analog-to-digital converters available with us can also handle 8 inputs only.

4.3 The digital receiver system

Figure 4.1 shows the schematic of the 1-bit raw voltage recording receiver. The digital receiver is implemented on Reconfigurable Open Architecture Computing Hardware (ROACH) from the Collaboration for Astronomy Signal Processing and Electronics Research (CASPER). The ROACH board hardware has the Xilinx Virtex-5 FPGA[‡]. The RF signals from the each of the eight antennas pass through independent amplifier and bandpass filter of 50 - 70 MHz before being fed to ADCs. We have used two Quad-ADC cards, each containing four AD9480 ICs[§]. The signals are sampled at 90 MHz. A single clock is used to sample all the antennas. The sampled band lies in the second Nyquist zone of 90 MHz. The ADC converts the input voltage to a 8-bit Fixed point number (Fix 8.7) between -1 and +1. The sign bit from each of these numbers is separated. So we have 1-bit from each antenna channel. Therefore, the ADC output is an unsigned 8-bit number (UFix8.0) representing the input voltage from each of the 8 channels. Such 1024x8 8-bit numbers are packetized together and sent to the recording computer over 10 Gigabit Ethernet (10GbE). Note that 10GbE allows transmission of 64-bit numbers[¶]. So, one packet has 1024 64-bit numbers. This results in a data rate of ≈0.72 Gbits/s. This is much smaller compared to the the data rate of ≈5.6 Gbits/s which would have resulted if 8-bits were recorded from each antenna channel. To avoid packet losses while recording, the data is captured using n2disk program[‖] on a 32 GB RAM computer. Each packet also contains a user datagram protocol (UDP) header(58 bytes) and a custom header (80 bytes) that contain the observation details, 1 pulse per second (PPS) count, and a packet count. The 1 PPS signal is derived from a GPS clock[**] and given to the FPGA via the ADC card to generate the 1 PPS

[†] https://nenufar.obs-nancay.fr/en/astronomer/

[‡] https://casper.astro.berkeley.edu/wiki/ROACH

[§] https://www.analog.com/en/products/AD9480.html

[¶] https://casper-toolflow.readthedocs.io/en/latest/src/blockdocs/Ten_GbE.html

[‖] https://www.ntop.org/products/traffic-recording-replay/n2disk/

[**] https://novotech.com/wp/wp-content/uploads/2022/11/Thunerbolt-E-GPS-Disciplined-Clock-Data-Sheet pdf

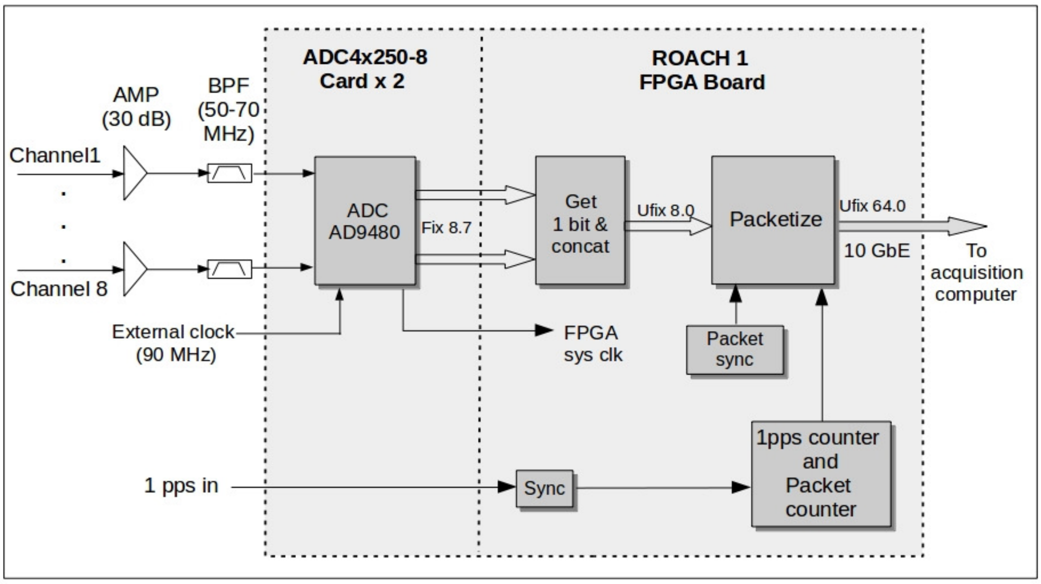

Figure 4.1: 1-bit raw voltage recording system used in the GAPS.

count. The packet-count is a unique packet number assigned to each packet. It is used to check for any packet losses. The recorded file contains a time series of 1-bit voltages from each antenna channel. Some of the characteristics are listed in Table 4.1.

4.4 Offline beam formation

Figure 4.2 shows the offline beamforming pipeline. First, the packets are unscrambled to get voltage time series of the individual antenna channels. Delays are applied to these time series according to the desired declination where the beam needs to be

Table 4.1: Characteristics of 8-element GAPS

Number of channels	8
Sampling rate	90 MSPS
Sampled bits	1
Observation band	45 - 90 MHz (50 - 70 MHz for the present work)
Beamforming	offline
FFT size	Variable (8192 for the present work)
Frequency resolution	10.98 kHz
Post-detection time resolution	Variable (min 91.02 μs for one spectrum)
Declination coverage	$-26.4°$ S to $+53.6°$ N

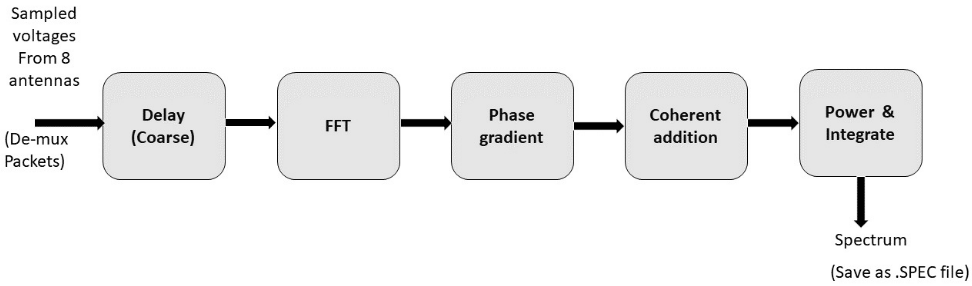

Figure 4.2: Offline beamforming pipeline used in the GAPS.

pointed. Note that the array is oriented in the north-south direction, so the beam forming is performed along the declination. Based on the declination, the geometric delays are calculated using the formula $t_j{=}d_j sin\theta/c$, where t_j is the delay required for j^{th} antenna at a distance of d_j from the reference antenna for the source at angle θ, and c is the velocity of light. The sampling interval (t_s) is 1/90 MHz = 11.11 ns. So, the time series are delayed by the closest integer multiple of 11.11 ns (i.e. mt_s, where m is an integer).

The uncompensated fractional delays ($\Delta t_j{=}t_j$ - mt_s) can be compensated by applying a phase gradient in the spectral domain, i.e. $\phi_{j,k}{=}2\pi F_k \Delta t_j$, where F_k is k^{th} frequency bin. The delayed voltage streams are Fourier transformed using FFT. Subsequently, the phase compensation is performed by multiplying the complex Fourier output by $e^{-i\phi_j}$. An 8192-point FFT is performed, resulting in 4096 positive frequency bins with a resolution of 10.986 kHz. The number of FFT points and hence the resolution can be changed depending on the requirement since the beamforming is performed offline. After the phase compensation, the individual spectrum from each antenna are added together, modulo-squared, and integrated according to the desired temporal resolution. Multiple beams pointing at different declinations can be formed by changing the delay and phase values. A '.SPEC' file is stored for each beam containing the corresponding power spectrum series. These are further processed using the standard PulsaR Exploration and Search TOolkit (PRESTO, Ransom, 2011).

4.5 Observations

The initial run of the new system was carried out on 2023 August 10 for ≈5 h, starting from ≈08:49 LST. Three beams pointing towards declinations 6.17° N, 7.92° N, and 15.85° N were formed offline from the raw voltage data recorded. The power spectrum series from these three beams were stored in three separate .SPEC files with time resolutions of 4 ms, 2 ms and 1 ms, respectively. The files were converted to SIGPROC ‘filterbank’ (.fil) format[††]. As first step, RFI excision was performed using *rficlean* (Maan, van Leeuwen, and Vohl, 2021) to mitigate strong periodic RFI. Subsequently we used *rfifind* from PRESTO, which searches for time and frequency domain RFI and creates mask files. This is followed by *prepfold* which is used to fold and dedisperse the data and detect pulsars. Three pulsars B0834+06 (J0837+0610), B0950+08 (J0953+0755) and B1133+16 (J1136+1551) were detected in the above three beams, respectively (see Figures 4.7 & 4.8). A solar event (a similar type III burst studied by Ramesh and Ebenezer, 2001) was also recorded during the observation at ≈11:03 LST. The declination of Sun was ≈15.7° N. A separate beam was formed pointing towards the above declination with time resolution of ≈10 ms. We carried out analysis with single pulse search pipeline developed using PRESTO routines. The maximum SNR was obtained for dispersion measured (DM) $\approx 13.2\,\mathrm{pc\,cm^{-3}}$. The de-dispersed dynamic spectra of the solar burst is shown in Figure 4.3. The burst was also noticed in the observations carried out with the other solar radio spectrographs in the Gauribidanur observatory. Figure 4.4 shows the dynamic spectra of the same burst as detected in the Gauribidanur Low-frequency Solar Spectrograph (GLOSS, Kishore *et al.*, 2014) and e-Callisto (Benz *et al.*, 2009). Table 4.2 compares the parameters of these different spectrographs with the GAPS system used for this solar observation. Note that the spectrum showed in the Figure 4.3 is de-dispersed and averaged in time and frequency. Figure 4.5 shows the original dynamic spectrum (before de-dispersion and averaging) observed with GAPS. Finer structures in the GAPS spectrum can be seen because of higher time and frequency resolution, better sensitivity and the ability to steer the beam in the direction of the source.

Table 4.2: Comparison between spectrographs of Gauribidanur

Instrument	GAPS	GLOSS	e-Callisto
No. of antennas	8	1	1
SEFD	0.4 MJy	3.2 MJy	3.2 MJy
Operating frequency	50-70 MHz	15-175 MHz	15-175 MHz
Frequency resolution	10.98 kHz	100 kHz	62.5 kHz
Time resolution	10 ms	143 ms	250 ms

To verify the performance of GAPS, we formed 41 beams covering the declination range from −26.3° S to +53.7° N in steps of 2° for the duration of the solar burst in Figure 4.3. Mean count during the solar burst at 60 MHz in each of the 41 beams were obtained. The count is maximum for the beam closest to the Sun’s declination. A Gaussian fit to the data points indicates HPBW ≈6° (see Figure 4.6), which matches with the predicted HPBW of the GAPS antenna array in the present case (see Section 4.2).

[††] http://sigproc.sourceforge.net/sigproc.pdf

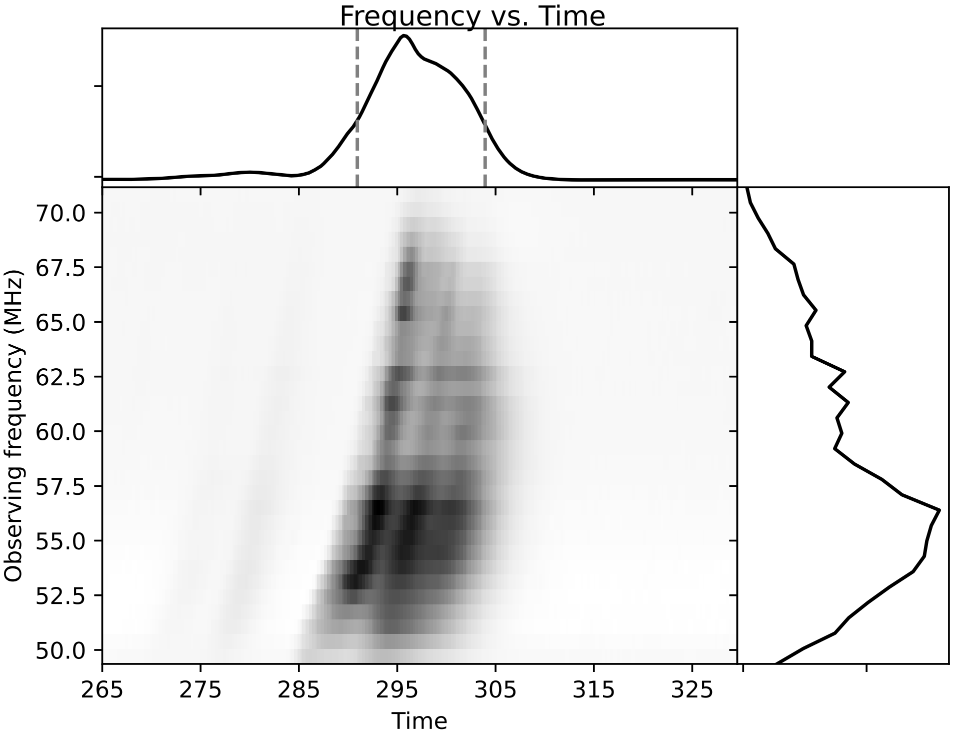

Figure 4.3: De-dispersed dynamic spectrum corresponding to the type III solar radio burst observed with the 8-element GAPS on 2023 August 10. The data was processed using the single pulse search pipeline developed using PRESTO. A range of dispersion measure (DM) values from 0 - 50 pc cm^{-3} were applied in steps of 0.2 . The maximum SNR was obtained for DM 13.2 pc cm^{-3}. The time in the x-axis starts from 11:02:30 LST, and the interval is 10 s. The upper panel shows the spectrally averaged time profile and the right panel shows the temporally averaged spectral profile of the burst.

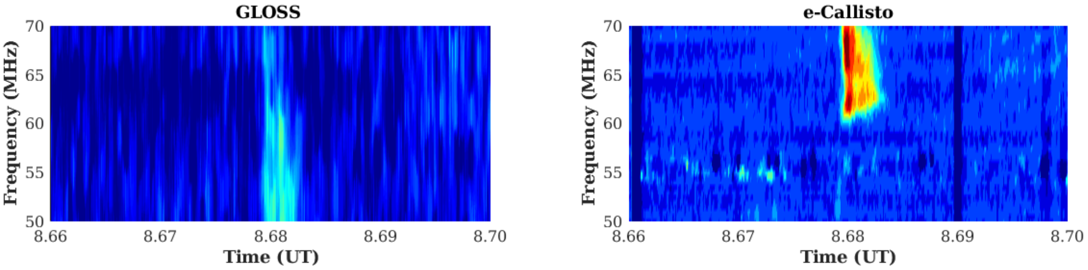

Figure 4.4: Dynamic spectra corresponding to the type III solar radio burst observed with GLOSS (left) and e-Callisto (right) on 2023 August 10. The spectra are zoomed in to 50-70 MHz to match the observing band of GAPS.

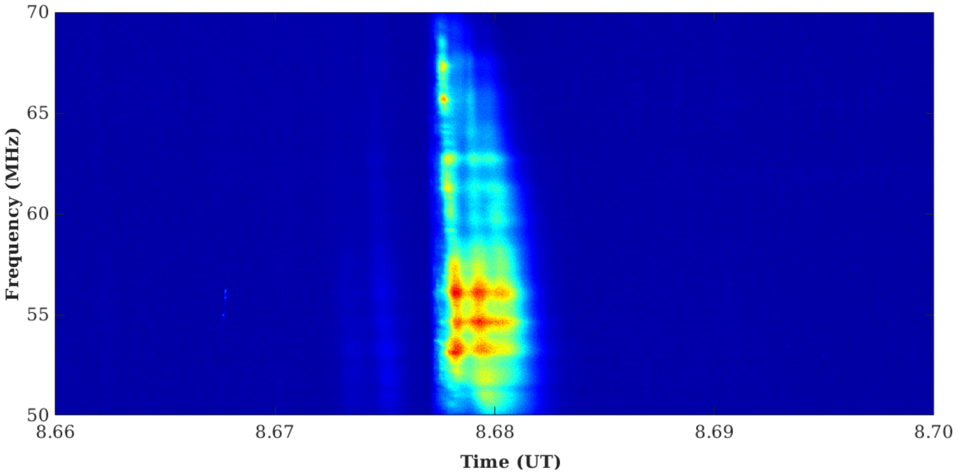

Figure 4.5: Original dynamic spectrum of a type III solar radio burst observed with the GAPS on 2023 August 10.

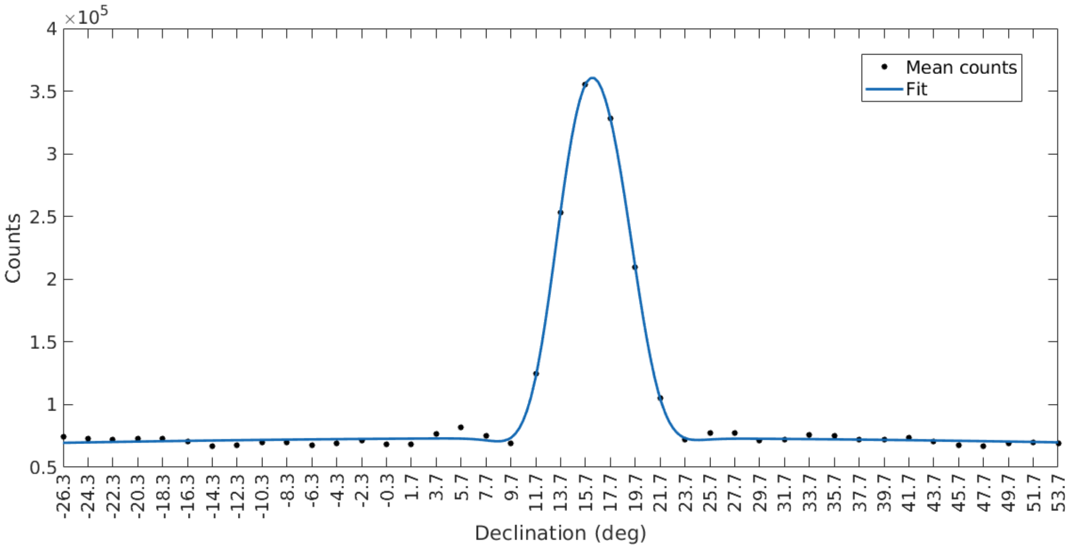

Figure 4.6: The declination beam of GAPS at 60 MHz obtained by using multiple beams formed during the solar observations in Figure 4.5.

On 2023 October 18, a 4 h observation run starting at ≈17:27 LST was carried out. A beam was formed pointing towards declination ≈21.88° N with 4 ms time resolution. Pulsar B1919+21 (J1921+2153) was detected in this data (see Figure 4.8). A subsequent observation for a period of ≈7.2 h was performed on 2023 October 21 starting at ≈06:36 LST. Pulsars B0834+06 (J0837+0610), B0919+06 (J0922+0638), B0950+08 (J0953+0755), B0943+10 (J0946+0951) and B1133+16 (J1136+1551) were detected using ≈6 h data around the transit of each pulsar (see Figure 4.8). Four beams were formed pointing towards declinations 6.17° N, 7.92° N, 9.86° N and 15.85° N with 1 ms resolution. Pulsars B0834+06 and B0919+06 were detected in the same beam.

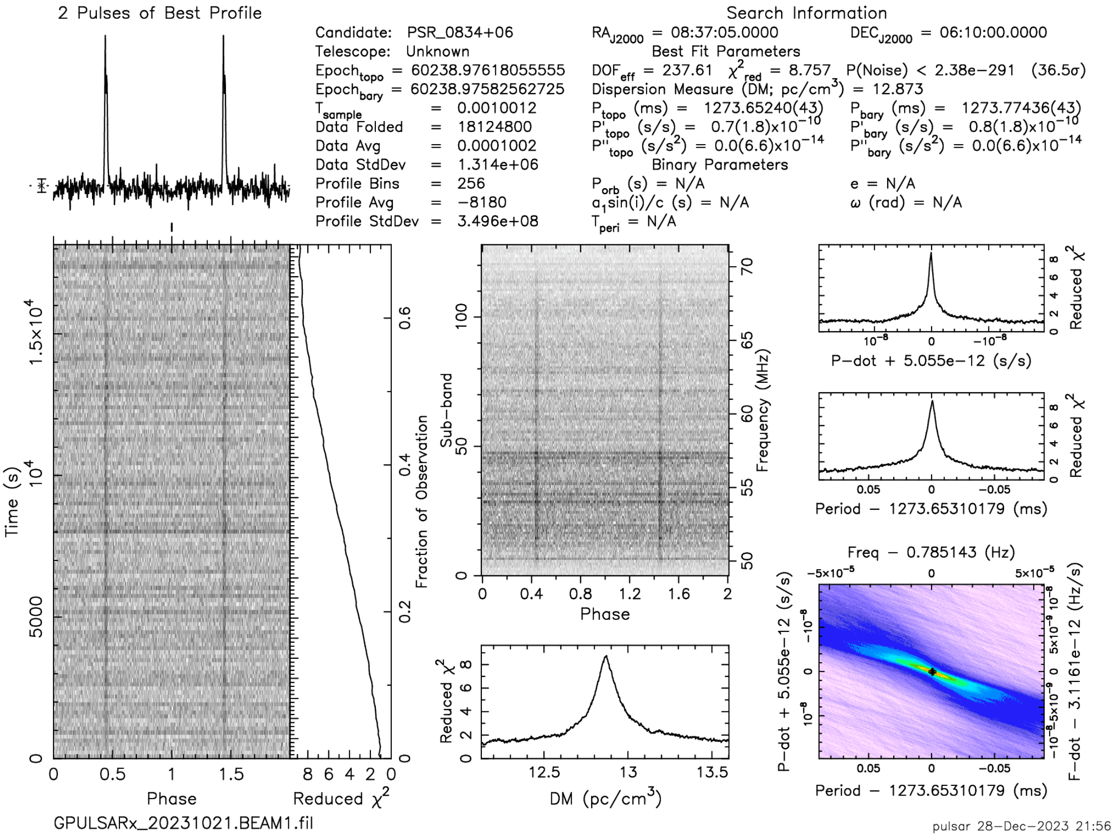

Figure 4.7: Observations of the pulsar B0834+06 (J0837+0610) on 2023 October 21 with GAPS in the frequency range of 50 to 70 MHz for a period of ≈4 h. 13385 pulses were added to get the average pulse profile. The data were analyzed using PRESTO.

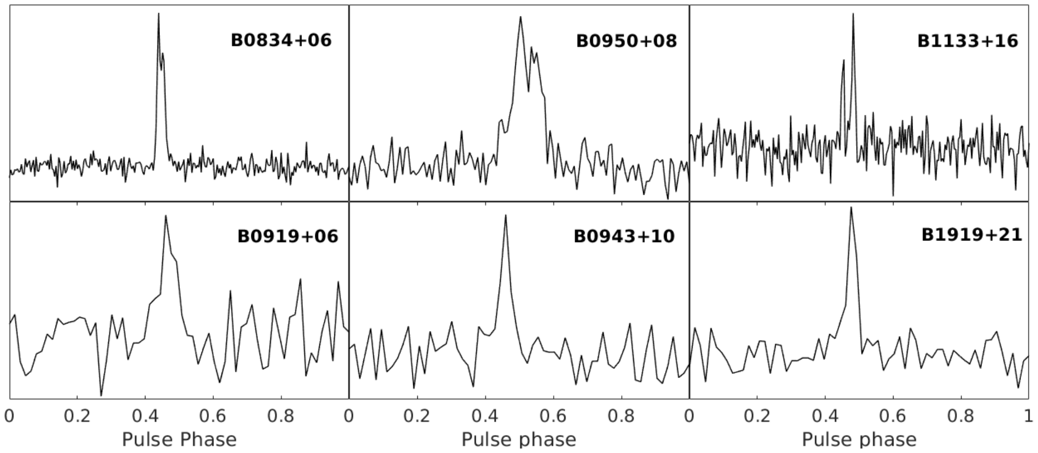

Figure 4.8: Average profiles of the pulsars observed with GAPS using 1-bit raw voltage recording system and offline beamformation. Details are available in Table 4.3. Individual pulsar detection plots available in Appendix E. Note that the y-axis markings are not mentioned here as they are arbitrary and different for each profile.

Table 4.3: Characteristics of the pulsars observed with GAPS using 1-bit raw voltage recording system (Numbers within the brackets are from Bondonneau *et al.* (2020))

Pulsar	Period (s)	DM (pc/cm^3)	Duty cycle (%)	SNR (folded)	Observing duration (h)	Pulses averaged
B0834+06	1.274±0.000043 (1.274)	12.873±0.05 (12.864)	6.4±0.8 (6.9)	36.5 (309)	6 (1)	13385
B0919+06	0.431±0.000016 (0.431)	27.330±0.02 (27.296)	14.4±0.8 (15.4)	6.0 (144)	6 (3)	58139
B0943+10	1.098±0.000069 (1.098)	15.348±0.02 (15.329)	12.9±0.8 (15.2)	6.3 (148)	6 (2.5)	18181
B0950+08	0.253±0.000050 (0.253)	2.965±0.05 (2.971)	15.3±0.8 (14.6)	24.6 (140)	6 (1)	67193
B1133+16	1.188±0.000023 (1.188)	4.848±0.03 (4.846)	12.7±0.8 (18.7)	8.4 (261)	6 (2)	16849
B1919+21	1.337±0.000017 (1.337)	12.420±0.02 (12.437)	7.8±0.8 (8.4)	12.5 (180)	4 (1)	11219

The estimated parameters of the different pulsars mentioned above are listed in Table 4.3. The corresponding numbers reported previously by Bondonneau *et al.* (2020) from online, multi-bit digitization observations elsewhere in nearly the same frequency range are mentioned within the brackets. The period & DM for each pulsar in the two cases agree well. The pulsar average profiles in Figure 4.8 also closely match with the average profiles at low frequencies reported in the literature (Malov and Malofeev, 2010; Hassall *et al.*, 2012; Zakharenko *et al.*, 2013; Stovall *et al.*, 2015;

Pilia *et al.*, 2016; Bilous *et al.*, 2020; Bondonneau *et al.*, 2020). Any minor differences are likely due to noisy detections in the present case. For example in the case of Bondonneau *et al.* (2020), the bandwidth and A_e used were higher than the present observations by factors of ≈2.75 & ≈10, respectively. Furthermore, 12-bit ADC was used in their observations. Its quantization efficiency is ≈(1/0.64) times higher than that of the 1-bit ADC used in the present observations (Thompson, Moran, and Swenson, 2017). The duration of observation for the respective pulsars in the two cases are also different. If we take into consideration all these factors, then the expected SNR for the pulsar B0834+06 in GAPS observations as compared to Bondonneau *et al.* (2020) is, $\frac{309*0.64}{10\sqrt{2.75/6}}\approx 30$. Compared to this, the observed SNR with 8-element GAPS is ≈36. Note that the duty cycle mentioned in Table 1 corresponds to the effective pulse width in pulse profiles at 50% of the highest peak intensity (i.e. w50).

4.6 Summary

We have presented a 1-bit raw voltage recording system for observations of pulsars at low radio frequencies. Other than reduction in the senstivity which could be partly compensated by the use of higher sampling rate (Van Vleck and Middleton, 1966; Burns and Yao, 1969; Thompson, Moran, and Swenson, 2017), the 1-bit quantization does not have an effect on the parameters of a pulsar like period, DM, etc. (see Table 4.3). Most of the modern low-frequency radio telescopes have multi-bit digital receivers which provide higher dynamic range (Taylor *et al.*, 2012; van Haarlem *et al.*, 2013; Prabu *et al.*, 2015; Reddy *et al.*, 2017; Zarka *et al.*, 2020; Girish *et al.*, 2023). However, in a relatively minimal RFI location like Gauribidanur (Monstein, Ramesh, and Kathiravan, 2007; Kishore *et al.*, 2015; Hariharan *et al.*, 2016b; Bane *et al.*, 2023), a lower dynamic range digital receiver can be used (see e.g. Zakharenko *et al.*, 2016). Our results indicate that in such circumstances the sensitivity to observe faint events within a short time interval depends largely on the effective collecting area and the observing bandwidth. It is well known that absolute flux measurments can be difficult in 1-bit receivers (Van Vleck and Middleton, 1966; Udaya Shankar and Ravi Shankar, 1990; Ramkumar, Prabu, and Markendeyalu, 1994; Ramesh, Sundara Rajan, and Sastry, 2006b; Stein, 2019). But in a wide-field multi-beam system where the primary requirement is to cover maximum area of the sky with high temporal and spectral resolution, such binary receiver systems can be beneficial. Overall, the 1-bit receiver offers flexibility, allowing multiple simultaneous beams in different directions, different integration times and frequency channel widths, and different filtering algorithms to be used. Further, the archival data can be stored in raw form with fewer resources and reprocessed in the future as per requirements. Reports indicate that 1-bit raw voltage recording had been used at higher frequencies also (Teng *et al.*, 2015). With the currently available technology, sampling rates upto ≈40 GHz can be achieved.

Chapter 5

Single pulse search

5.1 Introduction

Since the beginning of radio astronomy, transient phenomena have been a source of vast interest and continue to be a major frontier in the field. Radio transients come in the form of pulses, flares, or bursts and are likely to be associated with compact sources and explosive or dynamic events, thereby offering a unique opportunity to understand the physics of such extreme conditions. In addition, such short-duration pulses are a powerful probe for the intervening medium to study its properties. Therefore, exploration of such transient phenomena is one of the most rapidly growing fields in radio astronomy. Though compared to X-rays and γ-rays, searches for transient radio signals have seen only moderate success due to limited sensitivity and sky coverage. Radio transients can be of short durations (less than a few seconds, called Fast transients) or long duration (greater than a few seconds, called Slow transients). They can be of galactic or extra-galactic origin. Pulsars are the most common and perhaps most studied example of fast transients. There are other sources of radio transients like Jupiter, which emits radio flares at decameter wavelengths, radio flares from Brown dwarfs and various active stars, Solar bursts, Gamma-ray burst (GRB) afterglows, Soft Gamma-ray repeaters (SGRs), Rotating radio transients (RRATs), radio bursts from supernovae, bursts from the explosions of primordial black holes, emission from inspiraling neutron stars, etc. (see Cordes and McLaughlin, 2003, and references therein).

5.1.1 Fast Radio Bursts

The most fascinating transient phenomena in the Universe are the Fast Radio Bursts (FRBs). FRBs are subsecond radio flashes that are extremely bright and highly dispersed (Cordes and Chatterjee, 2019; Petroff, Hessels, and Lorimer, 2022). The first FRB was detected in 2007 (Lorimer *et al.*, 2007). Their physical origin is still debated with numerous theories (Platts *et al.*, 2019). Their short duration and high brightness indicate extremely energetic yet compact sources, and their high dispersion measures (300-3000 pc/cm^3) indicate extragalactic origin. There are some FRBs which repeat (Spitler *et al.*, 2016; CHIME/FRB Collaboration *et al.*, 2019a). Since their discovery, most of the FRBs have been observed at the high frequencies of ∼1 GHz, even up to 8 GHz (Gajjar *et al.*, 2018). The Canadian Hydrogen Intensity Mapping Experiment telescope (CHIME) has discovered many hundreds of FRBs in the frequency range 400-800 MHz (CHIME/FRB Collaboration *et al.*, 2019b) including many repeating FRBs (CHIME/FRB Collaboration *et al.*, 2023). The repeaters are typically wider in time but narrower in bandwidth compared to the one-offs and commonly show a complex time-frequency structure with downward drifting subbursts in frequency as time progresses, even after dedispersion- the so-called "sad trombone" effect (Hessels *et al.*, 2019). This suggests there might be at least two different types of FRBs.

Detection of FRBs at low radio frequencies is challenging. As discussed in Section 1.4.3 of Chapter 1, the increased galactic background temperature and the increased ferocious effects of the ISM make it difficult to observe such highly dispersed and smeared pulses at low frequencies. However, FRBs have been detected at low radio frequencies, for example, at 350 MHz (Parent *et al.*, 2020), 328 MHz (Pilia *et al.*, 2020), and 300 MHz (Chawla *et al.*, 2020). One of the most interesting FRBs is FRB 20180916B. It repeats with a period of 16.35 ± 0.15 days with a ∼5-day long activity window (CHIME/FRB Collaboration *et al.*, 2020). It has been localised to a nearby spiral galaxy (Marcote *et al.*, 2020) at a luminosity distance of ∼149 Mpc, which makes it the closest of any localised FRBs. Recently, chromatic activity from FRB 20180916B was detected down to low radio frequencies of 120 MHz (Pastor-Marazuela *et al.*, 2021) and 110 MHz (Pleunis *et al.*, 2021). These are the lowest frequency detections of an FRB so far and suggest that there might be a possibility to detect them at even lower frequencies, i.e., below 100 MHz. Observations of FRBs at low frequencies are important to see if there exists a turnover like pulsars or a cutoff, which can help in understanding their emission mechanisms. It can also offer an opportunity to constrain the properties of the circumburst environment (Ravi *et al.*, 2019). Thus, despite the challenges, there is an immense motivation for FRB observations at low radio frequencies. As the FRB population continues to grow (∼600 one-offs and 60 repeaters)*, it is extremely important to carry low-radio frequency surveys, especially targeting the repeaters. Recently, there was an extremely luminous (MJy level) FRB-like radio burst from the Galactic magnetar SGR J1935+2154 (Bochenek *et al.*, 2020a; The CHIME/FRB Collaboration, 2020). It shows a possible link between FRBs and Magnetars. So, monitoring of such Magnetars is also important.

Detecting such fast transients requires a time-domain signal processing of data sampled at high time and frequency resolutions. The computational needs are also

---

*`http://www.chime-frb.ca/catalog`

higher as a huge number of DM trails are required in a blind search scanning over a wide field in the sky. One way to test an instrument's capability to detect dispersed single pulses is by detecting the giant pulses from pulsars.

5.1.2 Giant pulses from pulsars

Pulsars were first discovered as single pulses on a chart recorder (Hewish *et al.*, 1968), followed by the Crab (B0531+21) pulsar detected through its giant pulses (Staelin and Reifenstein, 1968). Giant pulses (GPs) are pulses with strengths of 100 or even 1000 times the mean pulse intensity. Peak flux of $\sim 10^5$ Jy was recorded at 435 MHz for a duration of 100 μs by Hankins and Rickett (1975) in observations of Crab. Giant pulses have been detected from other pulsars as well: PSR B1937+21, B1821-24, B0540-69, B1112+50, B0031-07, B1957+20, B0950+08, B1237+25, etc. (Cognard *et al.*, 1996; Romani and Johnston, 2001; Johnston and Romani, 2003; Ershov and Kuzmin, 2003; Kuzmin, Ershov, and Losovsky, 2004; Joshi *et al.*, 2004; Smirnova, 2012; Kazantsev and Potapov, 2017). Giant pulses show a power-law nature of the pulse energy distribution (Gower and Argyle, 1972) and have narrower widths compared to the average pulse emission (Knight, 2007).

Crab giant pulses are broadband and are detected across the entire electromagnetic spectrum (Rankin *et al.*, 1970; Lundgren *et al.*, 1995; Hankins and Eilek, 2007; Karuppusamy, Stappers, and van Straten, 2010; Bhat *et al.*, 2007). Though studies of Crab GPs have mostly concentrated on frequencies above 100 MHz due to relatively stronger emission and availability of big radio telescopes, there have been some surveys below 100 MHz. Crab GPs have been detected at frequencies as low as 23 MHz (Popov *et al.*, 2006). Other low-frequency observations include: 20–84 MHz (Ellingson *et al.*, 2013; Eftekhari *et al.*, 2016), 32-80 MHz (Stappers *et al.*, 2011), 38 MHz (Deshpande, 2009), 40 and 60 MHz (Kuzmin *et al.*, 2002), 68.7 MHz (Bondonneau *et al.*, 2021), 111 MHz (Popov *et al.*, 2006), 116 MHz (Karuppusamy, Stappers, and Lee, 2012). Table 5.1 summarizes some Crab GP surveys below 100 MHz. Crab GPs exhibit peak flux densities in the order of 100 to 1000 Jy in these frequencies. It is observed that the mean spectral index of Crab GPs flattens from about -2.6 ± 0.5 at high-radio frequencies to about -0.7 ± 1.4 at low-radio frequencies (Meyers *et al.*, 2018), following a spectral turnover at ~100 MHz (Rankin, 1993). The nanosecond wide GPs at high frequencies are highly scattered at low frequencies; e.g., at 60 MHz, the scattering timescale is five times the spin period (~33 ms) of the pulsar (Bondonneau *et al.*, 2021). Kuzmin *et al.* (2002) determined the scatter broadening (τ_{sc}) to be ~140 ms at 60 MHz. The pulse widths of these GPs below 100 MHz range from 100 ms to a couple of seconds.

Table 5.1: Crab Giant pulse surveys below 100 MHz

Frequency	Telescope	Duration	Pulses detected	Peak flux	Ref.
23 MHz	UTR-2	12 hr	45	150 Jy	Popov *et al.* (2006)
38 MHz	ETA	14 hr	11	1 kJy	Deshpande (2009)
28-84 MHz	LWA	10 hr	33	1 kJy (60 MHz)	Ellingson *et al.* (2013)
28-84 MHz	LWA	73 hr	1458	585 Jy (60 MHz)	Eftekhari *et al.* (2016)

5.2 Single pulse search strategy

A single pulse search pipeline was developed to look for dispersed single pulses in GAPS data. The data processing for a single pulse search is essentially different from the one used for getting the average pulse from pulsars described in previous chapters, as it doesn't involve folding of the data. The strategy for single pulse search follows the basic steps outlined by Cordes and McLaughlin (2003); Bhat (2011). It involves dedispersion over trail DMs, matched filtering, and candidate selection. The pipeline was developed using algorithms available from PRESTO[†]. Figure 5.1 shows the basic steps of the pipeline.

Transient signals are characterized by two basic quantities: Dispersion measure (DM) and pulse width. So, searching for single pulses involves scanning over these two parameters. At present, only incoherent dedispersion is used in our system. First, the filterbank data (*.fil* file) of the observation is passed through two stages of RFI mitigation using `rficlean`[‡] and `rfifind` from PRESTO, the latter of which creates a

---

[†] https://github.com/scottransom/presto

[‡] https://github.com/ymaan4/RFIClean

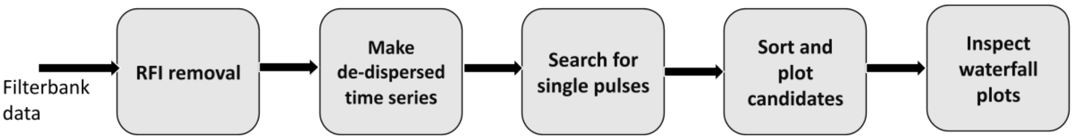

Figure 5.1: Single pulse search pipeline

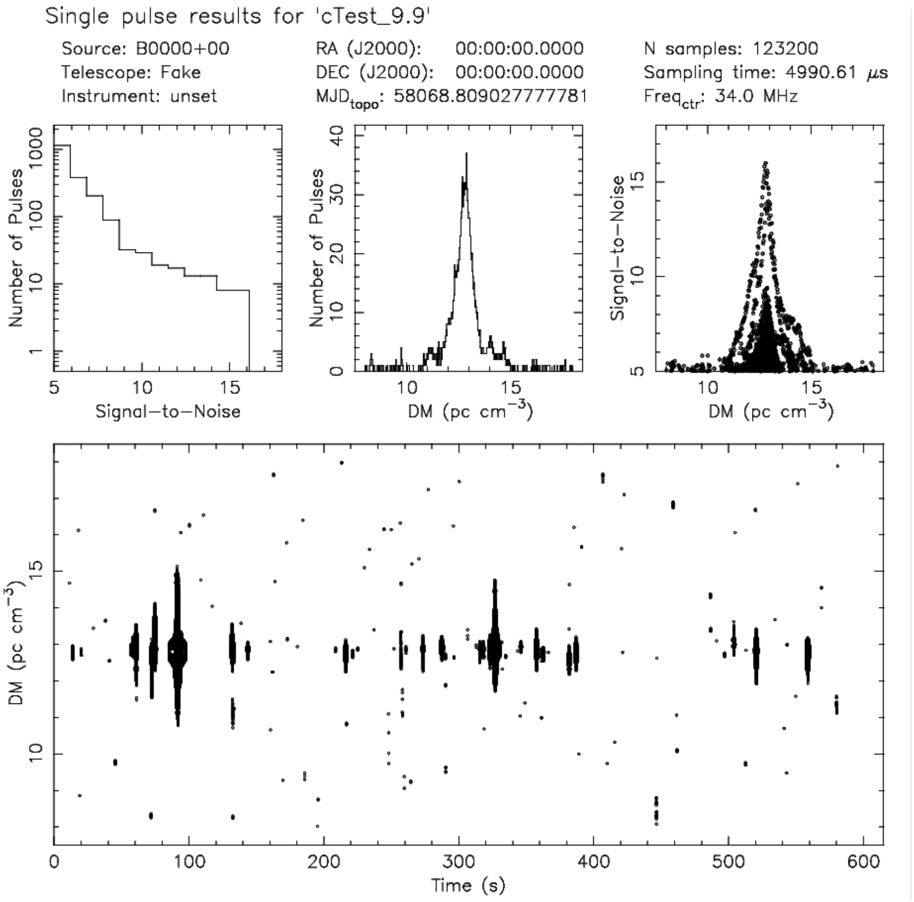

Figure 5.2: Single pulse search diagnostic plot for a test data

mask file, which will be used in subsequent stages. The first parameter to search over is DM. A DM range ($DM_l - DM_h$) and DM step (δDM) are selected. The data and trail DM values are passed to `prepdata` routine to generate de-dispersed time series at the different DM values. `prepdata` takes the filterbank data, applies a delay to each frequency channel as per the DM, and then averages over all frequency channels to generate a time series data. For each DM, it generates a *.dat* file, which has the time series data and an *.info* file, which has the information about the data. Then, each de-dispersed time series data is passed to `single_pulse_search.py` python code available from PRESTO to search for single pulses. This code uses *'matched-filtering'* to look for single pulses. The basic concept of matched filtering is that the highest detected Signal-to-Noise Ratio (SNR) is achieved when the effective sampling time of the time series is equal to the detected width of the pulse (Cordes and McLaughlin, 2003). As the width of the pulse is unknown, various widths need to be tried. The process of matched filtering involves convolving the data with different widths of the boxcar function, and significant candidates are filtered. The SNR threshold for filtering and the maximum width of the boxcar function can be selected here. It

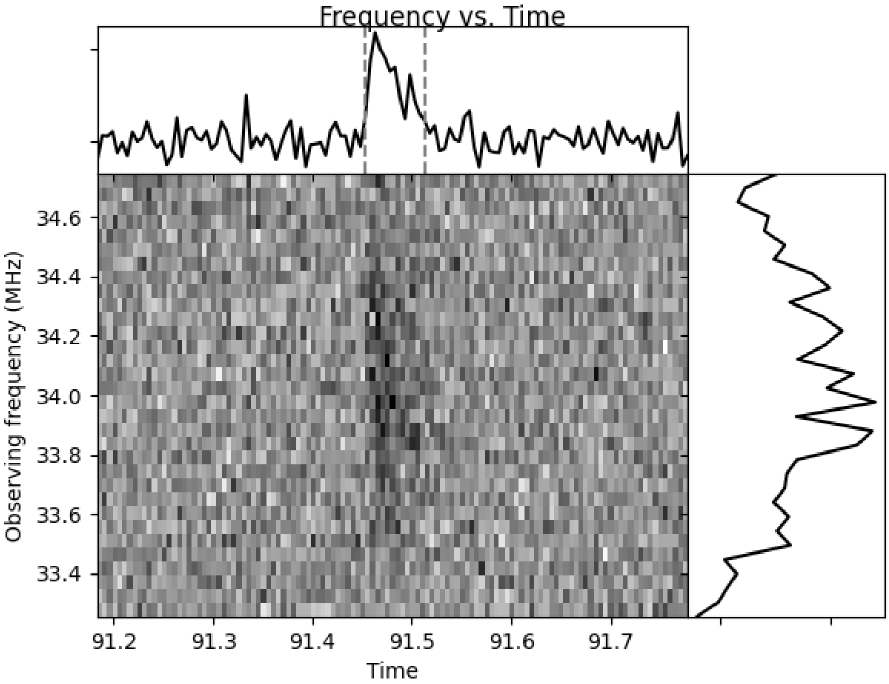

Figure 5.3: Waterfall plot for a single pulse detected in test data

generates a list of single pulse candidates for each time series and a 'diagnostic plot' as shown in Figure 5.2. The diagnostic plot has multiple panels, which are useful in recognizing true detections. For example, the signal-to-noise histogram will deviate from Gaussian in the presence of strong signals. In the case of a true astronomical signal, the plot of DM v/s signal-to-noise will show a peak at the true DM, and the strength will fall as we go away from this DM. In the scatter plot of time and DM, the density of events will be higher near the true DM. The sizes of the black circles in the time- DM plot (the bottom panel) are proportional to the peak SNRs i.e. higher the SNR, bigger the circle. In contrast, RFI will peak at zero DM and fall off as DM increases. Using the diagnostic plot and individual single pulse files created for each time series, the prominent candidates are sorted. The parameters of these candidates, i.e., DM, timestamp, and downsample factor, are then used to make a dynamic spectrum or the *'waterfall plot'* showing the de-dispersed pulse across the frequency channels. The waterfall plots are then manually inspected to identify true detections.

5.2.1 Testing the pipeline

To test the single pulse search pipeline, test data of the pulsar B0834+06 from GEETEE (courtesy of Dr. Yogesh Maan, NCRA) was used. It was a ~600 s data at the frequency of 34 MHz with a bandwidth of 1.5 MHz, 256 channels, and a time resolution of 166.35 µs. The data was passed through the single pulse search pipeline with a DM range of 8 to 18 and a DM step of 0.02. A good DM scheme can be found using the `DDplan.py` script from PRESTO. The result is shown in Figure 5.2. It can be seen that the signal strength tends to peak near the true DM $\approx 12.86\,pc/cm^3$ for PSR B0834+06. About 10 pulses were found above the 7 sigma level after sifting through all the candidates. The waterfall plot of the strongest pulse with a 16 sigma level and DM of 12.80 is shown in Figure 5.3.

The pipeline was used to detect solar bursts shown in Figure 3.8 in Chapter 3 and Figure 4.3 in Chapter 4.

5.3 Observations

During May-June 2021, observations were conducted using GAPS to see if we could detect any Giant pulses from the Crab pulsar (B0531+21). The prototype system described in Chapter 2 was used for these observations. The data was acquired with a time resolution of 1 ms. The on-board FFT was increased to 16384 points, giving 8192 frequency channels with a resolution of ~5.5 KHz in the band of 45-90 MHz, out of which 50-80 MHz band was useful. Each observation was 1 hr long, centered at the transit of the Crab pulsar. In total, ~30 hrs of useful data was acquired.

The data was processed using the single pulse search pipeline. For the search, a DM range of 40-70 pc/cm^3 with DM step (δDM) of 0.01 was used. This δDM was selected using the following approach. As per the equation 1.23, the smearing due to dispersion within a frequency channel Δf (MHz) is

$$\Delta t_{DM,\Delta f} \simeq 8.3 \times 10^6 \times DM \frac{\Delta f}{f_o^3} \text{ ms.} \tag{5.1}$$

Now, if δDM is the error in the DM value used for dedispersion, the pulse will be smeared across the observation bandwidth B (MHz), given by

$$\Delta t_{\Delta DM,B} \simeq 8.3 \times 10^6 \times \Delta DM \frac{B}{f_o^3} \text{ ms.} \tag{5.2}$$

The smearing due to the error in DM should not exceed the intra-channel smearing. So,

$$\Delta t_{\Delta DM,B} \leq \Delta t_{DM,\Delta f} \tag{5.3}$$

$$\Delta DM \leq DM \frac{\Delta f}{B}. \tag{5.4}$$

For Crab pulsar, $DM = 56.77\,pc/cm^3$ (Manchester *et al.*, 2005)[§]. For a 30 MHz

---

[§] https://www.atnf.csiro.au/research/pulsar/psrcat/

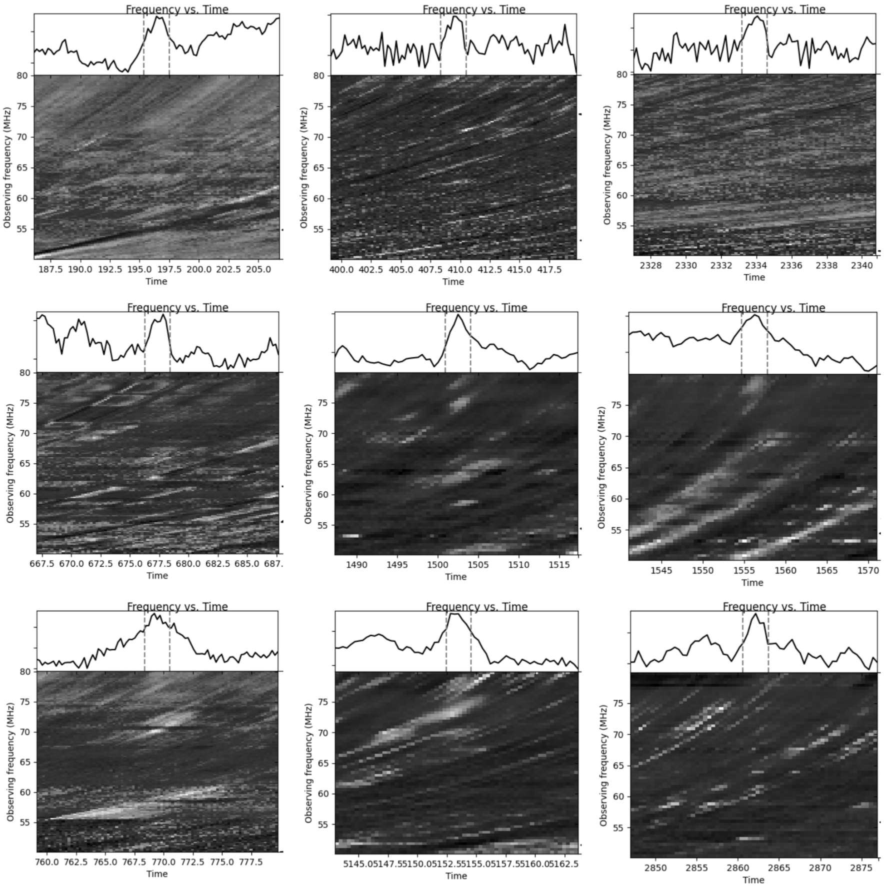

Figure 5.4: Giant pulse candidates detected by the single pulse search pipeline

bandwidth and channel width of 0.0055 MHz, $\Delta DM \leq 0.01$.

For each DM in the DM range used, a dedispersed time series is created. The time series is downsampled to 100 ms from 1 ms as the expected pulse width for Crab GPs in this frequency range is in the order of seconds. Each time series is then searched for single pulses using matched filtering. The threshold for single pulse SNR was used as 7, and the maximum pulse width for the search was set as 5-10 ms. Then, the single pulse events are grouped together as per their DM and SNR (sigma), and the best candidates are sifted. For each candidate, waterfall plots are made as per the timestamp and DM.

In our observation, a few single pulse candidates were found by the single pulse search pipeline with DM close to the DM of the Crab pulsar ($\sim 56.7, pc/cm^3$). Waterfall plots of some of those candidates are shown in Figure 5.4. However, on the visual inspection, none of these candidates were confirmed as giant pulses from the pulsar. Due to a lack of good SNR and a lack of satisfactory signatures across the observing band, these candidates were not considered giant pulses. We examine possible reasons for non-detection in the next section using simulations of single pulses.

5.4 Single pulse simulation

To test if the pipeline is sensitive to highly dispersed and scattered single pulses, such single pulses were simulated and injected into the data. Single pulses were simulated using the 'Simpulse' package[¶]. Simpulse is a C++/python library for simulating dispersed pulses. It takes parameters like Dispersion measure (DM), Spectral Index, frequency range, fluence, etc., and generates dispersed pulse as a 2-dimension matrix of frequency and time. These synthetic pulses can be added to sample data to test the data processing pipeline.

The same data acquired during the Crab pulsar observation campaign described in the previous section was used for this analysis. Synthetic pulses were generated using Simpulse with DM of 56.77 pc/cm^3 and SI of 2 following the values from references in the Section 5.1.2 to match with the giant pulses from the Crab pulsar. The dispersive delay between the pulse at 50 MHz and 80 MHz for the DM of 56.77 pc/cm^3 is ∼57.5 s. Hundreds of such pulses with varying fluences/signal-to-noise ratios (SNR) were injected into the test data. The test data was passed through the PRESTO-based Single pulse search pipeline described in Section 5.2. Single pulses were searched in the DM range of 40-70 pc/cm^3 with the step of 0.1 and SNR threshold of 8. A dynamic spectrum of the sample data with a strong dispersed pulse injected is shown in Figure 5.5. The waterfall plot of the same pulse detected by the single pulse search pipeline at the DM of 56.7 pc/cm^3, and SNR of ∼20 is shown in Figure 5.6.

A completeness analysis of the pipeline was carried out to determine how efficiently the pipeline detects pulses at different SNRs. Completeness is defined as the fraction of pulses detected in a given SNR to the total number of pulses injected in that SNR. Figure 5.7 shows the completeness fraction as a function of SNR. 50% completeness or detection efficiency is achieved for SNR of ∼10. Using the radiometric equation 1.29 for bandwidth of 30 MHz and duration of 100 ms gives the flux density for 10 sigma level for GAPS as ∼2000 Jy.

An approximate rate of occurrence of Crab giant pulses with this flux can be determined. The Flux of Crab pulsar at 74 MHz is ∼85 Jy (Rickett and Seiradakis, 1982). Taking a spectral index of ∼2 (Meyers *et al.*, 2018), the flux at 60 MHz is $\sim$ 55 Jy. The pulses from the Crab pulsar are distributed as $N = (500 \times 60)S^{-2.5}$, where N is the number of pulses per hour with pulse energy stronger than S (Argyle and Gower, 1972). So, at 60 MHz, Crab Giant pulses with a flux density of ∼2000 Jy, which is ∼36 times the average flux density at this frequency, will occur at the rate of ∼4 pulses/hour.

[¶] `https://github.com/kmsmith137/simpulse`

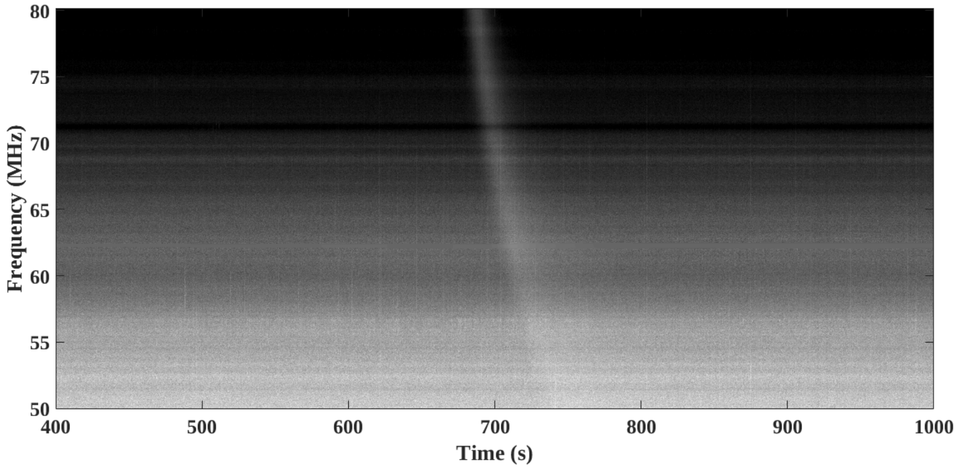

Figure 5.5: A dispersed pulse injected in the test data

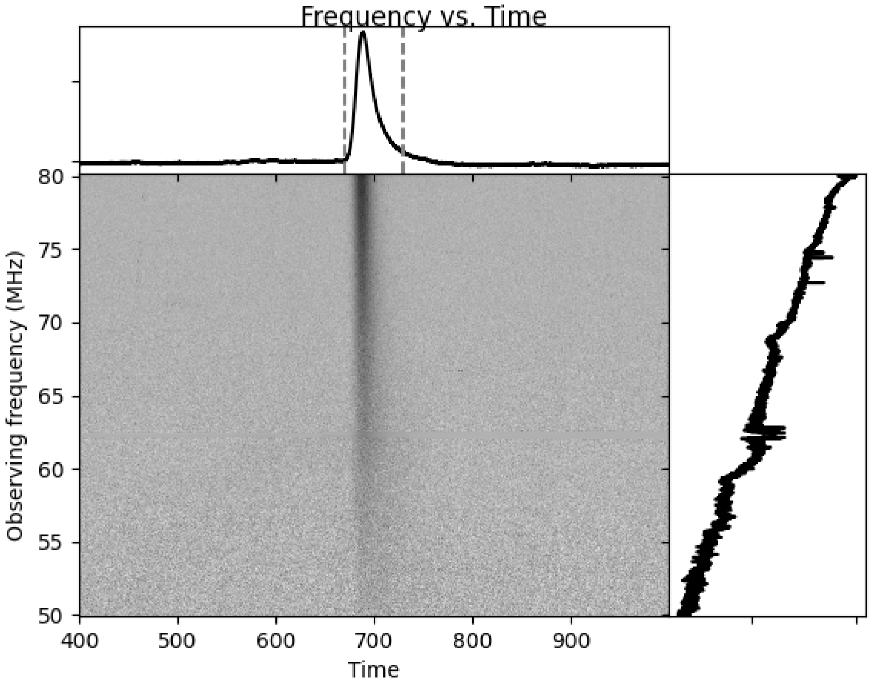

Figure 5.6: Injected pulse detected by single pulse search pipeline. The waterfall plot is obtained by dedispersing the spectrum with $DM = 56.7\, pc/cm^3$.

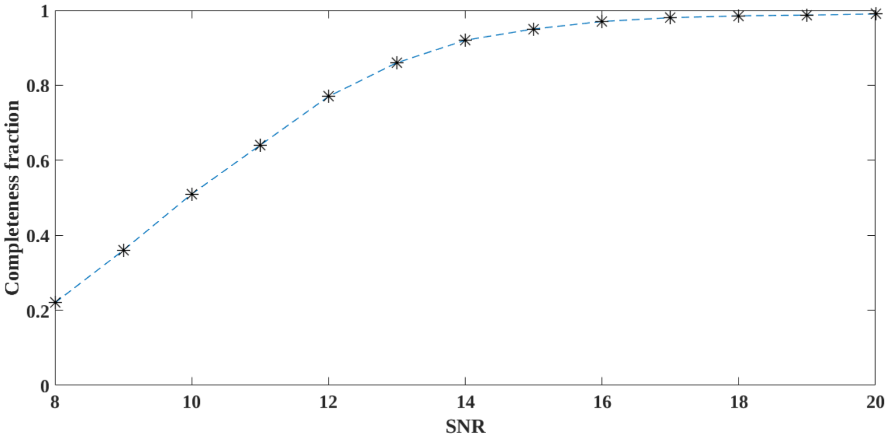

Figure 5.7: Completeness analysis of the single pulse search pipeline using synthetic pulses

However, Crab Giant pulse flux values are known to vary considerably, especially at the tail end of the distribution (Deshpande, 2009). In a 10 hr observation by Ellingson *et. al.*, the brightest pulse at 60 MHz had a flux density of about 1000 Jy (Ellingson *et al.*, 2013), whereas in a 73 hr observation by Eftekhari *et. al.*, the brightest pulse detected at 60 MHz had a peak flux density of about 585 Jy (Eftekhari *et al.*, 2016). This might explain why, in our 30 hr observation, no strong Giant pulses were detected. Longer observations in the future might be helpful in the detection of such giant pulses. Also, there is a plan to expand the system with more antennas that will increase the collection area and subsequently increase the sensitivity. The use of coherent de-dispersion with increased collecting area will increase the chances of giant pulse detection.

5.5 Summary

Though no giant gulses were detected in the trial run with GAPS, the efforts have led to the development of a Single pulse search pipeline that can be used to detect transients. The pipeline was tested by injecting synthetic dispersed pulses in the data, and the limits of detection and different caveats in the pipeline were understood. The single pulse search pipeline was used to detect strong transients from the Sun, and it was optimized to detect highly dispersed and scattered single pulses. Further refinement of the search strategy with longer observations might help detect some giant pulses from pulsars. Archival data from GAPS is processed regularly with different parameters to check for the presence of transient signatures. This study was helpful in understanding the system, requirements for single pulse detections, and future improvements and developments.

Chapter 6

Conclusion

6.1 Summary

6.1.1 Chapter 1

In Chapter 1, we saw the observational properties of pulsars and the effects of interstellar medium on the radio signals from pulsars. We saw the importance of low-frequency pulsar observations. It was understood that pulsar observations at frequencies <100 MHz are necessary to get more insights into the pulsar emission mechanism, which is still not quite understood yet. There is a need for a dedicated low-frequency radio telescope to monitor pulsars continuously and also search for transients. We saw what are the challenges and requirements for such a low-frequency telescope, and based on that, a new observing facility was set up at the Gauribidanur Observatory.

6.1.2 Chapter 2

In Chapter 2, we presented the details of the newly developed Gauribidanur Pulsar System (GAPS). We presented the initial tests and observation results. We successfully detected the 4 targeted pulsars (PSRS B1919+21, B0834+06, B0950+08, and B1133+16) with the prototype system in the frequency range 50 - 80 MHz. Regular observations of pulsars with this instrument can help in getting more insights into the pulsar emission mechanism. The system, with its large bandwidth (≈ 30 MHz), wide sky coverage ($\approx 110^\circ \times 80^\circ$), high spectral and temporal resolutions, geographical location ($\approx 14^\circ$ N), and the fact that the array is dedicated to time domain astronomy is a good tool to monitor for transients at low-radio frequencies.

6.1.3 Chapter 3

GAPS was upgraded to have a digital beamforming capability. A digital beamformer allows multiple simultaneous beams to form in the sky. The digital beamformer setup and the initial observations with this setup were described in Chapter 3. We successfully observed a pulsar and a solar radio burst simultaneously with the upgraded system and demonstrated how one can be used to calibrate the other. Such a wide-field multi-beam system, where multiple beams are formed digitally covering a wide area in the sky, is of huge interest in the radio astronomy community now, especially in the context of the upcoming Square Kilometer Array (SKA). Such a system can be used to survey transients. We also successfully demonstrated the single search pipeline developed by detecting the solar burst. It shows that our system is capable of detecting bright, dispersed, short-duration bursts. So, there is a scope for detecting a bright FRB or other astrophysical transients like the bright bursts from the Galactic magnetar SGR J1935+2154 (Bochenek *et al.*, 2020a).

6.1.4 Chapter 4

In Chapter 4, we present the successful demonstration of a 1-bit raw voltage recording system for observations of pulsars at low radio frequencies. Individual antennas from the GAPS system were digitized, and beamforming was performed in post-processing, forming multiple beams simultaneously. Six pulsars were detected using this system, and it was shown that apart from loss in sensitivity, 1-bit quantization doesn't affect other pulsar parameters. Such a binary system reduces the tremendous data rates/volumes and processing complexities associated with high-speed voltage recording systems. A 1-bit voltage recording system offers flexibility and is better suited where the goal is to cover the maximum area of the sky with high temporal and spectral resolutions for blind-search transient surveys with lower computing costs and data storage requirements.

6.1.5 Chapter 5

Searching for fast astrophysical transients is of great interest in the radio astronomy community. In Chapter 5, we saw the importance of searching for FRBs below 100 MHz, which is more exciting now considering the recent low-frequency detections (Pleunis *et al.*, 2021; Pastor-Marazuela *et al.*, 2021). In this light, it was necessary to have a single pulse search strategy for our system. A single pulse search pipeline was developed and used to detect solar radio bursts. It was tested using test Pulsar data with giant pulses and integrating simulated single pulsed in the filterbank data. Crab pulsar was also observed to search for Giant pulses. No giant pulses were detected during the 30 hr observation, but further longer observation and future developments will help in detecting Giant pulses and possible FRBs.

During the course of the thesis, three papers were published in refereed journals (Bane *et al.*, 2022, 2023, 2024). Some information and work not included in these articles is presented in the appendices.

6.2 Future Work

With the prototype system, the receiver system and data processing techniques required for time domain astronomy at low radio frequencies were understood and demonstrated. As the present prototype system is limited by sensitivity due to less collecting area, only the strongest pulsars were observed and detected by their integrated pulse profiles. Large bandwidth and large integration time were utilized to compensate for the lack of collecting area. In order to detect fainter pulsars and transients like FRB, if they should occur, the collecting area must be increased. We can increase the collecting area by using all the 16 antennas with the digital beamformer by modifying the backed.

The Gauribidanur observatory has Gauribidanur RAdioheliograPH (GRAPH), which is used to image the Solar corona in the frequency range of 40-150 MHz. It has 384 Log-Periodic Dipole Antennas arranged in a “ T ” configuration. The effective collecting area is $\sim 4000\, m^2$ at 50 MHz frequency, which is about 50 times the effective area of GAPS in the present case. In addition, the GRAPH array is also being augmented with orthogonal antennas in its N-S arm, which will facilitate polarimetric observations as well. The back-end receiver system of GRAPH, which is presently a 4096-channel correlator, needs to be modified to a phased array mode or a raw voltage recording system. To process the huge amount of data, searching for dispersed pulses will require additional infrastructure like GPU cards to accelerate the search. Coherent dedispersion can also be implemented to increase the search sensitivity.

With GAPS acting as the path-finder for non-solar transient observations at the Gauribidanur observatory, it has the potential to be an important tool in time-domain astronomy at low radio frequencies. Regular monitoring of pulsars and searches for transients like FRB below 100 MHz frequencies can help fill the “gaps” in our understanding of these phenomena.

Bibliography

Ansoldi, S., Antonelli, L.A., Antoranz, P., Babic, A., Bangale, P., Barres de Almeida, U., Barrio, J.A., Becerra González, J., Bednarek, W., Bernardini, E., Biasuzzi, B., Biland, A., Blanch, O., Bonnefoy, S., Bonnoli, G., Borracci, F., Bretz, T., Carmona, E., Carosi, A., Colin, P., Colombo, E., Contreras, J.L., Cortina, J., Covino, S., Da Vela, P., Dazzi, F., De Angelis, A., De Caneva, G., De Lotto, B., de Oña Wilhelmi, E., Delgado Mendez, C., Di Pierro, F., Dominis Prester, D., Dorner, D., Doro, M., Einecke, S., Eisenacher Glawion, D., Elsaesser, D., Fernández-Barral, A., Fidalgo, D., Fonseca, M.V., Font, L., Frantzen, K., Fruck, C., Galindo, D., García López, R.J., Garczarczyk, M., Garrido Terrats, D., Gaug, M., Godinović, N., González Muñoz, A., Gozzini, S.R., Hanabata, Y., Hayashida, M., Herrera, J., Hirotani, K., Hose, J., Hrupec, D., Hughes, G., Idec, W., Kellermann, H., Knoetig, M.L., Kodani, K., Konno, Y., Krause, J., Kubo, H., Kushida, J., La Barbera, A., Lelas, D., Lewandowska, N., Lindfors, E., Lombardi, S., Longo, F., López, M., López-Coto, R., López-Oramas, A., Lorenz, E., Makariev, M., Mallot, K., Maneva, G., Mannheim, K., Maraschi, L., Marcote, B., Mariotti, M., Martínez, M., Mazin, D., Menzel, U., Miranda, J.M., Mirzoyan, R., Moralejo, A., Munar-Adrover, P., Nakajima, D., Neustroev, V., Niedzwiecki, A., Nevas Rosillo, M., Nilsson, K., Nishijima, K., Noda, K., Orito, R., Overkemping, A., Paiano, S., Palatiello, M., Paneque, D., Paoletti, R., Paredes, J.M., Paredes-Fortuny, X., Persic, M., Poutanen, J., Prada Moroni, P.G., Prandini, E., Puljak, I., Reinthal, R., Rhode, W., Ribó, M., Rico, J., Rodriguez Garcia, J., Saito, T., Saito, K., Satalecka, K., Scalzotto, V., Scapin, V., Schultz, C., Schweizer, T., Shore, S.N., Sillanpää, A., Sitarek, J., Snidaric, I., Sobczynska, D., Stamerra, A., Steinbring, T., Strzys, M., Takalo, L., Takami, H., Tavecchio, F., Temnikov, P., Terzić, T., Tescaro, D., Teshima, M., Thaele, J., Torres, D.F., Toyama, T., Treves, A., Ward, J., Will, M., Zanin, R.: 2016, Teraelectronvolt pulsed emission from the Crab Pulsar detected by MAGIC. *Astron. Astrophys.* **585**, A133. DOI. ADS.

Argyle, E., Gower, J.F.R.: 1972, The Pulse-Height Distribution for NP 0532. *Astrophys. J. Lett.* **175**, L89. DOI. ADS.

Backer, D.C.: 1970, Pulsar Nulling Phenomena. *Nature* **228**(5266), 42. DOI. ADS.

Bane, K.S., Barve, I.V., Gireesh, G.V.S., Kathiravan, C., Ramesh, R.: 2022, Prototype for pulsar observations at low radio frequencies using log-periodic dipole antennas. *Journal of Astronomical Telescopes, Instruments, and Systems* **8**(1), 017001. DOI. ADS.

Bane, K.S., Barve, I.V., Gireesh, G.V.S., Kathiravan, C., Ramesh, R.: 2023, Initial results from multi-beam observations of pulsars and solar transient with the digital beamformer for the Gauribidanur pulsar system. *Journal of Astronomical Telescopes, Instruments, and Systems* **10**(1), 014001. DOI. ADS.

Bane, K.S., Barve, I.V., Gireesh, G.V.S., Kathiravan, C., Ramesh, R.: 2024, A 1 bit Raw Voltage-recording System for Dedicated Observations of Transients at Low Radio Frequencies. *Astrophys. J.S* **272**(2), 27. DOI. ADS.

Bates, S.D., Lorimer, D.R., Verbiest, J.P.W.: 2013, The pulsar spectral index distribution. *Mon. Not. Roy. Astron. Soc.* **431**(2), 1352. DOI. ADS.

Benz, A.O., Monstein, C., Meyer, H., Manoharan, P.K., Ramesh, R., Altyntsev, A., Lara, A., Paez, J., Cho, K.-S.: 2009, A World-Wide Net of Solar Radio Spectrometers: e-CALLISTO. *Earth, Moon and Planets* **104**, 277. DOI. ADS.

Bhat, N.D.R.: 2011, Searches for radio transients. *Bulletin of the Astronomical Society of India* **39**(3), 353. DOI. ADS.

Bhat, N.D.R., Rao, A.P., Gupta, Y.: 1999, Long-Term Scintillation Studies of Pulsars. I. Observations and Basic Results. *Astrophys. J.S* **121**(2), 483. DOI. ADS.

Bhat, N.D.R., Cordes, J.M., Camilo, F., Nice, D.J., Lorimer, D.R.: 2004, Multifrequency Observations of Radio Pulse Broadening and Constraints on Interstellar Electron Density Microstructure. *Astrophys. J.* **605**, 759.

Bhat, N.D.R., Wayth, R.B., Knight, H.S., *et al.*: 2007, Detection of Crab Giant Pulses Using the Mileura Widefield Array Low Frequency Demonstrator Field Prototype System. *Astrophys. J.* **665**, 618.

Bhat, N.D.R., Tremblay, S.E., Kirsten, F., *et al.*: 2018, Observations of Low-frequency Radio Emission from Millisecond Pulsars and Multipath Propagation in the Interstellar Medium. *Astrophys. J. Suppl. Ser.* **238**, 1.

Bilous, A.V., Kondratiev, V.I., Kramer, M., *et al.*: 2016, A LOFAR census of non-recycled pulsars: average profiles, dispersion measures, flux densities, and spectra. *Astron. Astrophys.* **591**, A134.

Bilous, A.V., Bondonneau, L., Kondratiev, V.I., Grießmeier, J.-M., Theureau, G., Hessels, J.W.T.: 2020, A LOFAR census of non-recycled pulsars: extending to frequencies below 80 MHz. *Astron. Astrophys.* **635**, A75. DOI. ADS.

Bochenek, C.D., Ravi, V., Belov, K.V., *et al.*: 2020a, A fast radio burst associated with a Galactic magnetar. *Nature* **587**, 59.

Bochenek, C.D., McKenna, D.L., Belov, K.V., *et al.*: 2020b, STARE2: Detecting Fast Radio Bursts in the Milky Way. *Publ. Astron. Soc. Pacific* **132**, 034202.

Bondonneau, L., Grießmeier, J.-M., Theureau, G., Bilous, A.V., Kondratiev, V.I., Serylak, M., Keith, M.J., Lyne, A.J.: 2020, A census of the pulsar population observed with the international LOFAR station FR606 at low frequencies (25-80 MHz). *Astron. Astrophys.* **635**, A76. DOI. ADS.

Bondonneau, L., Grießmeier, J.-M., Theureau, G., Cognard, I., Brionne, M., Kondratiev, V., Bilous, A., McKee, J.W., Zarka, P., Viou, C., Guillemot, L., Chen, S., Main, R., Pilia, M., Possenti, A., Serylak, M., Shaifullah, G., Tiburzi, C., Verbiest, J.P.W., Wu, Z., Wucknitz, O., Yerin, S., Briand, C., Cecconi, B., Corbel, S., Dallier, R., Girard, J.N., Loh, A., Martin, L., Tagger, M., Tasse, C.: 2021, Pulsars with NenuFAR: Backend and pipelines. *Astron. Astrophys.* **652**, A34. DOI. ADS.

Buch, K.D.: 2019, Rfi excision in radiometers: A radio astronomy perspective. In: *IGARSS 2019 - 2019 IEEE International Geoscience and Remote Sensing Symposium*, 4535. DOI.

Burns, W.R., Yao, S.S.: 1969, Clipping loss in the one-bit autocorrelation spectral line receiver. *Radio Sci.* **4**, 431. DOI. ADS.

Carrell, R.L.: 1961, The Design of Log-periodic Dipole Antennas. *IRE Nat. Conven. Record* **1**, 61.

Champion, D.J., Petroff, E., Kramer, M., *et al.*: 2016, Five new fast radio bursts from the HTRU high-latitude survey at Parkes: first evidence for two-component bursts. *Mon. Not. Roy. Astron. Soc.* **460**, L30.

Chawla, P., Andersen, B.C., Bhardwaj, M., Fonseca, E., Josephy, A., Kaspi, V.M., Michilli, D., Pleunis, Z., Bandura, K.M., Bassa, C.G., Boyle, P.J., Brar, C., Cassanelli, T., Cubranic, D., Dobbs, M., Dong, F.Q., Gaensler, B.M., Good, D.C., Hessels, J.W.T., Landecker, T.L., Leung, C., Li, D.Z., Lin, H.-.H., Masui, K., Mckinven, R., Mena-Parra, J., Merryfield, M., Meyers, B.W., Naidu, A., Ng, C., Patel, C., Rafiei-Ravandi, M., Rahman, M., Sanghavi, P., Scholz, P., Shin, K., Smith, K.M., Stairs, I.H., Tendulkar, S.P., Vanderlinde, K.: 2020, Detection of Repeating FRB 180916.J0158+65 Down to Frequencies of 300 MHz. *Astrophys. J. Lett.* **896**(2), L41. DOI. ADS.

Chhabra, S., Gary, D.E., Hallinan, G., *et al.*: 2021, Imaging Spectroscopy of CME-associated Solar Radio Bursts using OVRO-LWA. *Astrophys. J.* **906**, 132.

CHIME/FRB Collaboration, Andersen, B.C., Bandura, K., Bhardwaj, M., Boubel, P., Boyce, M.M., Boyle, P.J., Brar, C., Cassanelli, T., Chawla, P., Cubranic, D., Deng, M., Dobbs, M., Fandino, M., Fonseca, E., Gaensler, B.M., Gilbert, A.J., Giri, U., Good, D.C., Halpern, M., Hill, A.S., Hinshaw, G., Höfer, C., Josephy, A., Kaspi, V.M., Kothes, R., Landecker, T.L., Lang, D.A., Li, D.Z., Lin, H.-H., Masui, K.W., Mena-Parra, J., Merryfield, M., Mckinven, R., Michilli, D., Milutinovic, N., Naidu, A., Newburgh, L.B., Ng, C., Patel, C., Pen, U., Pinsonneault-Marotte, T., Pleunis, Z., Rafiei-Ravandi, M., Rahman, M., Ransom, S.M., Renard, A., Scholz, P., Siegel, S.R., Singh, S., Smith, K.M., Stairs, I.H., Tendulkar, S.P., Tretyakov, I., Vanderlinde, K., Yadav, P., Zwaniga, A.V.: 2019a, CHIME/FRB Discovery of Eight New Repeating Fast Radio Burst Sources. *Astrophys. J. Lett.* **885**(1), L24. DOI. ADS.

CHIME/FRB Collaboration, Amiri, M., Bandura, K., Bhardwaj, M., Boubel, P., Boyce, M.M., Boyle, P.J., Brar, C., Burhanpurkar, M., Chawla, P., Cliche, J.F., Cubranic, D., Deng, M., Denman, N., Dobbs, M., Fandino, M., Fonseca, E., Gaensler, B.M., Gilbert, A.J., Giri, U., Good, D.C., Halpern, M., Hanna, D., Hill, A.S., Hinshaw, G., Höfer, C., Josephy, A., Kaspi, V.M., Landecker, T.L., Lang, D.A., Masui, K.W., Mckinven, R., Mena-Parra, J., Merryfield, M., Milutinovic, N., Moatti, C., Naidu, A., Newburgh, L.B., Ng, C., Patel, C., Pen, U., Pinsonneault-Marotte, T., Pleunis, Z., Rafiei-Ravandi, M., Ransom, S.M., Renard, A., Scholz, P., Shaw, J.R., Siegel, S.R., Smith, K.M., Stairs, I.H., Tendulkar, S.P., Tretyakov, I., Vanderlinde, K., Yadav, P.: 2019b, Observations of fast radio bursts at frequencies down to 400 megahertz. *Nature* **566**(7743), 230. DOI. ADS.

CHIME/FRB Collaboration, Amiri, M., Andersen, B.C., Bandura, K.M., Bhardwaj, M., Boyle, P.J., Brar, C., Chawla, P., Chen, T., Cliche, J.F., Cubranic, D., Deng, M., Denman, N.T., Dobbs, M., Dong, F.Q., Fandino, M., Fonseca, E., Gaensler, B.M., Giri, U., Good, D.C., Halpern, M., Hessels, J.W.T., Hill, A.S., Höfer, C., Josephy, A., Kania, J.W., Karuppusamy, R., Kaspi, V.M., Keimpema, A., Kirsten, F., Landecker, T.L., Lang, D.A., Leung, C., Li, D.Z., Lin, H.-H., Marcote, B., Masui, K.W., McKinven, R., Mena-Parra, J., Merryfield, M., Michilli, D., Milutinovic, N., Mirhosseini, A., Naidu, A., Newburgh, L.B., Ng, C., Nimmo, K., Paragi, Z., Patel, C., Pen, U.-L., Pinsonneault-Marotte, T., Pleunis, Z., Rafiei-Ravandi, M., Rahman, M., Ransom, S.M., Renard, A., Sanghavi, P., Scholz, P., Shaw, J.R., Shin, K., Siegel, S.R., Singh, S., Smegal, R.J., Smith, K.M., Stairs, I.H., Tendulkar, S.P., Tretyakov, I., Vanderlinde, K., Wang, H., Wang, X., Wulf, D., Yadav, P., Zwaniga, A.V.: 2020, Periodic activity from a fast radio burst source. *Nature* **582**(7812), 351. DOI. ADS.

CHIME/FRB Collaboration, Andersen, B.C., Bandura, K., Bhardwaj, M., Boyle, P.J., Brar, C., Cassanelli, T., Chatterjee, S., Chawla, P., Cook, A.M., Curtin, A.P., Dobbs, M., Dong, F.A., Faber, J.T., Fandino, M., Fonseca, E., Gaensler, B.M., Giri, U., Herrera-Martin, A., Hill, A.S., Ibik, A., Josephy, A., Kaczmarek, J.F., Kader, Z., Kaspi, V., Landecker, T.L., Lanman, A.E., Lazda, M., Leung, C., Lin, H.-H., Masui, K.W., McKinven, R., Mena-Parra, J., Meyers, B.W., Michilli, D., Ng, C., Pandhi, A., Pearlman, A.B., Pen, U.-L., Petroff, E., Pleunis, Z., Rafiei-Ravandi, M., Rahman, M., Ransom, S.M., Renard, A., Sand, K.R., Sanghavi, P., Scholz, P., Shah, V., Shin, K., Siegel, S., Smith, K., Stairs, I., Su, J., Tendulkar, S.P., Vanderlinde, K., Wang, H., Wulf, D., Zwaniga, A.: 2023, CHIME/FRB Discovery of 25 Repeating Fast Radio Burst Sources. *Astrophys. J.* **947**(2), 83. DOI. ADS.

Cognard, I., Shrauner, J.A., Taylor, J.H., Thorsett, S.E.: 1996, Giant Radio Pulses from a Millisecond Pulsar. *Astrophys. J. Lett.* **457**, L81. DOI. ADS.

Cole, T.W.: 1969, Pulsar slowdown rates for cp 0328 and hp 1506. *Nature (London), 223: 487(Aug. 2, 1969).* DOI. `https://www.osti.gov/biblio/4781486`.

Cooley, J.W., Tukey, J.W.: 1965, An algorithm for the machine calculation of complex fourier series. *Mathematics of Computation* **19**(90), 297. http://www.jstor.org/stable/2003354.

Cordes, J.M.: 1978, Observational limits on the location of pulsar emission regions. *Astrophys. J.* **222**, 1006.

Cordes, J.M., Chatterjee, S.: 2019, Fast Radio Bursts: An Extragalactic Enigma. *Annurev.aa.* **57**, 417. DOI. ADS.

Cordes, J.M., Lazio, T.J.W.: 2002, NE2001.I. A New Model for the Galactic Distribution of Free Electrons and its Fluctuations. *arXiv e-prints*, astro. DOI. ADS.

Cordes, J.M., McLaughlin, M.A.: 2003, Searches for fast radio transients. *The Astrophysical Journal* **596**(2), 1142. DOI. https://dx.doi.org/10.1086/378231.

Deshpande, A.A.: 1989, Pulsar Instrumentation for GMRT. *Technical report, Raman Research Institute.*

Deshpande, A.A., Radhakrishnan, V.: 1992, Pulsar observations at 34.5 MHz using the Gauribidanur Telescope. I. *Journal of Astrophysics and Astronomy* **13**, 151. DOI. ADS.

Deshpande, A.A., Shevgaonkar, R.K., Sastry, C.V.: 1989, The Decameterwave radio telescope at Gauribidanur: Antenna arrays and control system. *Journal of the Institution of Electronics and Telecommunications Engineering* **35**, 342.

Deshpande, K.B.: 2009, Dedicated Search for Low Frequency Radio Transient Astrophysical Events using ETA. Masters thesis, Virginia Polytechnic Institute and State University.

DuHamel, R., Isbell, D.: 1957, Broadband logarithmically periodic antenna structures. In: *1958 IRE International Convention Record* **5**, 119. DOI.

Dwarakanath, K.S., UdayaShankar, N.: 1990, A synthesis map of the sky at 34.5 MHz. *J. Astrophys. Astron.* **11**, 323.

Ebenezer, E., Ramesh, R., Subramanian, K.R., Sundara Rajan, M.S., Sastry, C.V.: 2001, A new digital spectrograph for observations of radio burst emission from the Sun. *Astron. Astrophys.* **367**, 1112. DOI. ADS.

Eftekhari, T., Stovall, K., Dowell, J., Schinzel, F.K., Taylor, G.B.: 2016, A Low frequency Survey of Giant Pulses from the Crab Pulsar. *Astrophys. J.* **829**, 62.

Ellingson, S.W., Clarke, T.E., Cohen, A., Craig, J., Kassim, N.E., Pihlstrom, Y., Rickard, L.J., Taylor, G.B.: 2009, The Long Wavelength Array. *IEEE Proceedings* **97**(8), 1421. DOI. ADS.

Ellingson, S.W., Clarke, T.E., Craig, J., Hicks, B.C., Lazio, T.J.W., Taylor, G.B., Wilson, T.L., Wolfe, C.N.: 2013, Observations of Crab Giant Pulses in 20-84 MHz using LWA1. *Astrophys. J.* **768**(2), 136. DOI. ADS.

Ershov, A.A., Kuzmin, A.D.: 2003, Detection of Giant Pulses from the Pulsar PSR B1112+50. *Astronomy Letters* **29**, 91. DOI. ADS.

Fedorova, V.A., Rodin, A.E.: 2019, Detection of Fast Radio Bursts on the Large Scanning Antenna of the Lebedev Physical Institute. *Astron. Rep.* **63**, 39.

Ford, J.M., Buch, K.D.: 2014, Rfi mitigation techniques in radio astronomy. In: *2014 IEEE Geoscience and Remote Sensing Symposium*, 231. DOI.

Gajjar, V., Siemion, A.P.V., Price, D.C., Law, C.J., Michilli, D., Hessels, J.W.T., Chatterjee, S., Archibald, A.M., Bower, G.C., Brinkman, C., Burke-Spolaor, S., Cordes, J.M., Croft, S., Enriquez, J.E., Foster, G., Gizani, N., Hellbourg, G., Isaacson, H., Kaspi, V.M., Lazio, T.J.W., Lebofsky, M., Lynch, R.S., MacMahon, D., McLaughlin, M.A., Ransom, S.M., Scholz, P., Seymour, A., Spitler, L.G., Tendulkar, S.P., Werthimer, D., Zhang, Y.G.: 2018, Highest Frequency Detection of FRB 121102 at 4-8 GHz Using the Breakthrough Listen Digital Backend at the Green Bank Telescope. *Astrophys. J.* **863**(1), 2. DOI. ADS.

Geyer, M., Karastergiou, A.: 2016, The frequency dependence of scattering imprints on pulsar observations. *Mon. Not. Roy. Astron. Soc.* **462**(3), 2587. DOI. ADS.

Geyer, M., Karastergiou, A., Kondratiev, V.I., *et al.*: 2017, Scattering analysis of LOFAR pulsar observations. *Mon. Not. Roy. Astron. Soc.* **470**, 2659.

Girish, B.S., Reddy, S.H., Sethi, S., Srivani, K.S., Abhishek, R., Ajithkumar, B.: 2023, Progression of digital-receiver architecture: From MWA to SKA1-Low, and beyond. *J. Astrophys. Astron.* **44**, 1641011. DOI. ADS.

Gower, J.F.R., Argyle, E.: 1972, Detection of Strong Interpulses from NP 0532. *Astrophys. J. Lett.* **171**, L23. DOI. ADS.

Gupta, Y., Rickett, B.J., Coles, W.A.: 1993, Refractive Interstellar Scintillation of Pulsar Intensities at 74 MHz. *Astrophys. J.* **403**, 183. DOI. ADS.

Gupta, Y., Chandra, P., Bagchi, M., Ramanujam, N.M., Maan, Y., Deshpande, A.A., Bhattacharyya, S.: 2016, Fast Transients with the Square Kilometre Array and its Pathfinders: An Indian Perspective. *J. Astrophys. Astron.* **37**, 37.

Hankins, T.H., Eilek, J.A.: 2007, Radio Emission Signatures in the Crab Pulsar. *Astrophys. J.* **670**(1), 693. DOI. ADS.

Hankins, T.H., Rickett, B.J.: 1975, Pulsar signal processing. *Methods in Computational Physics* **14**, 55. DOI. ADS.

Hankins, T.H., Rickett, B.J.: 1986, Frequency Dependence of Pulsar Profiles. *Astrophys. J.* **311**, 684. DOI. ADS.

Hariharan, K., Ramesh, R., Kathiravan, C., Wang, T.J.: 2016, Simultaneous Near-Sun Observations of a Moving Type IV Radio Burst and the Associated White-Light Coronal Mass Ejection. *Solar Phys.* **291**, 1405.

Hariharan, K., Ramesh, R., Kathiravan, C., Abhilash, H.N., Rajalingam, M.: 2016b, High Dynamic Range Observations of Solar Coronal Transients at Low Radio Frequencies with a Spectro-correlator. *Astrophys. J.S* **222**, 21. DOI. ADS.

Harris, C., Haines, K.: 2011, A Mathematical Review of Polyphase Filterbank Implementations for Radio Astronomy. **28**(4), 317. DOI. ADS.

Haslam, C.G.T., Salter, C.J., Stoffel, H., Wilson, W.E.: 1982, A 408-MHZ All-Sky Continuum Survey. II. The Atlas of Contour Maps. *Astron. Astrophys. Suppl.* **47**, 1.

Hassall, T.E., Stappers, B.W., Hessels, J.W.T., Kramer, M., Alexov, A., Anderson, K.: 2012, Wide-band simultaneous observations of pulsars: disentangling dispersion measure and profile variations. *Astron. Astrophys.* **543**, A66. DOI. ADS.

Hessels, J.W.T., Ransom, S.M., Stairs, I.H., Freire, P.C.C., Kaspi, V.M., Camilo, F.: 2006, A Radio Pulsar Spinning at 716 Hz. *Science* **311**(5769), 1901. DOI. ADS.

Hessels, J.W.T., Bilous, A., Coenen, T., Cooper, S., Kondratiev, V.I., van Leeuwen, J., Stappers, B.W., Verbiest, J.P.W., Zagkouris, K., Lofar Pulsar Working Group: 2014, A renaissance in low-frequency pulsar studies with LOFAR. In: *Astronomical Society of India Conference Series*, *Astronomical Society of India Conference Series* **13**, 43. ADS.

Hessels, J.W.T., Spitler, L.G., Seymour, A.D., Cordes, J.M., Michilli, D., Lynch, R.S., Gourdji, K., Archibald, A.M., Bassa, C.G., Bower, G.C., Chatterjee, S., Connor, L., Crawford, F., Deneva, J.S., Gajjar, V., Kaspi, V.M., Keimpema, A., Law, C.J., Marcote, B., McLaughlin, M.A., Paragi, Z., Petroff, E., Ransom, S.M., Scholz, P., Stappers, B.W., Tendulkar, S.P.: 2019, FRB 121102 Bursts Show Complex Time-Frequency Structure. *Astrophys. J. Lett.* **876**(2), L23. DOI. ADS.

Hewish, A., Bell, S.J., Pilkington, J.D.H., Scott, P.F., Collins, R.A.: 1968, Observation of a rapidly pulsating radio source. *Nature* **217**, 709.

Hickish, J., Abdurashidova, Z., Ali, Z., Buch, K.D., Chaudhari, S.C., Chen, H., Dexter, M., Domagalski, R.S., Ford, J., Foster, G., George, D., Greenberg, J., Greenhill, L., Isaacson, A., Jiang, H., Jones, G., Kapp, F., Kriel, H., Lacasse, R., Lutomirski, A., MacMahon, D., Manley, J., Martens, A., McCullough, R., Muley, M.V., New, W., Parsons, A., Price, D.C., Primiani, R.A., Ray, J., Siemion, A., Van Tonder, V., Vertatschitsch, L., Wagner, M., Weintroub, J., Werthimer, D.a.: 2016, A decade of developing radio-astronomy instrumentation using casper open-source technology. *Journal of Astronomical Instrumentation* **05**(04), 1641001. DOI. https://doi.org/10.1142/S2251171716410014.

Issur, N.H.: 2002, The Pulsar Observing System and Data Analysis Procedure Used at MRT. *Astrophys. Space Sci.* **282**, 77.

Izvekova, V.A., Malofeev, V.M., Shitov, Y.P.: 1989, The shapes of mean pulse profiles of pulsars'radio emission at the frequency 102,5 MHz. **66**, 345. ADS.

Johnston, S., Romani, R.W.: 2003, Giant Pulses from PSR B0540-69 in the Large Magellanic Cloud. *Astrophys. J. Lett.* **590**(2), L95. DOI. ADS.

Johnston, S., Karastergiou, A., Mitra, D., Gupta, Y.: 2008, Multifrequency integrated profiles of pulsars. *Monthly Notices of the Royal Astronomical Society* **388**(1), 261. DOI. https://doi.org/10.1111/j.1365-2966.2008.13379.x.

Joshi, B.C., Kramer, M., Lyne, A.G., McLaughlin, M.A., Stairs, I.H.: 2004, Giant Pulses in Millisecond Pulsars. In: Camilo, F., Gaensler, B.M. (eds.) *Young Neutron Stars and Their Environments* **218**, 319. DOI. ADS.

Kansabanik, D., Mondal, S., Oberoi, D.: 2023, Deciphering Faint Gyrosynchrotron Emission from a Coronal Mass Ejection using Spectro-polarimetric Radio Imaging. *Astrophys. J.* **950**, 164.

Karastergiou, A., Chennamangalam, J., Armour, W., *et al.*: 2015, Limits on fast radio bursts at 145 MHz with ARTEMIS, a real-time software backend. *Mon. Not. Roy. Astron. Soc.* **452**, 1254.

Karuppusamy, R., Stappers, B.W., Lee, K.J.: 2012, Crab giant pulses at low frequencies. *Astron. Astrophys.* **538**, A7. DOI. ADS.

Karuppusamy, R., Stappers, B.W., Serylak, M.: 2011, A low frequency study of PSRs B1133+16, B1112+50, and B0031-07. *Astron. Astrophys.* **525**, A55. DOI. ADS.

Karuppusamy, R., Stappers, B.W., van Straten, W.: 2010, Giant pulses from the Crab pulsar. A wide-band study. *Astron. Astrophys.* **515**, A36. DOI. ADS.

Kazantsev, A.N., Potapov, V.A.: 2017, Observations of giant pulses from B1237+25 (J1239+2453) at 111 MHz. Detection and classification. *Astronomy Reports* **61**(9), 747. DOI. ADS.

Keane, E.F., Johnston, S., Bhandari, S., Barr, E., Bhat, N.D.R.: 2016, The host galaxy of a fast radio burst. *Nature* **530**, 453.

Kishore, P.: 2016, Development of a broadband radio spectropolarimeter for solar observations. Doctoral dissertation, Indian Institute of Astrophysics.

Kishore, P., Kathiravan, C., Ramesh, R., Rajalingam, M., Indrajit, V.B.: 2014, Gauribidanur Low-Frequency Solar Spectrograph. *Solar Phys.* **289**, 3995. DOI. ADS.

Kishore, P., Ramesh, R., Kathiravan, C., Rajalingam, M.: 2015, A Low-Frequency Radio Spectropolarimeter for Observations of the Solar Corona. *Solar Phys.* **290**, 2409. DOI. ADS.

Knight, H.S.: 2007, A Parkes radio telescope study of giant pulses from PSR J1823-3021A. *Mon. Not. Roy. Astron. Soc.* **378**(2), 723. DOI. ADS.

Kondratiev, V.I., Verbiest, J.P.W., Hessels, J.W.T., Bilous, A.V., Stappers, B.W., Kramer, M., Keane, E.F., Noutsos, A., Osłowski, S., Breton, R.P., Hassall, T.E., Alexov, A., Cooper, S., Falcke, H., Grießmeier, J.-M., Karastergiou, A., Kuniyoshi, M., Pilia, M., Sobey, C., ter Veen, S., van Leeuwen, J., Weltevrede, P., Bell, M.E., Broderick, J.W., Corbel, S., Eislöffel, J., Markoff, S., Rowlinson, A., Swinbank, J.D., Wijers, R.A.M.J., Wijnands, R., Zarka, P.: 2016, A LOFAR census of millisecond pulsars. *Astron. Astrophys.* **585**, A128. DOI. ADS.

Kramer, M.: 1994, Geometrical analysis of average pulsar profiles using multi-component Gaussian FITS at several frequencies. II. Individual results. *Astron. Astrophys. Suppl.* **107**, 527. ADS.

Kraus, J.D.: 1966, *Radio Astronomy*, McGraw-Hill, New York.

Krishnakumar, M.A., Mitra, D., Naidu, A., Joshi, B.C., Manoharan, P.K.: 2015, Scatter Broadening Measurements of 124 Pulsars At 327 Mhz. *Astrophys. J.* **804**(1), 23. DOI. ADS.

Kumari, A., Ramesh, R., Kathiravan, C., Wang, T.J.: 2017, Strength of the Solar Coronal Magnetic Field - A Comparison of Independent Estimates Using Contemporaneous Radio and White-Light Observations. *Solar Phys.* **292**, 161.

Kuzmin, A.D., Ershov, A.A., Losovsky, B.Y.: 2004, Detection of Giant Pulses from the Pulsar PSR B0031-07. *Astronomy Letters* **30**, 247. DOI. ADS.

Kuzmin, A.D., Kondrat'ev, V.I., Kostyuk, S.V., Losovsky, B.Y., Popov, M.V., Soglasnov, V.A., D'Amico, N., Montebugnoli, S.: 2002, Frequency Dependence of the Scattering Pulse Broadening for the Crab Pulsar. *Astronomy Letters* **28**(4), 251. DOI. ADS.

Landecker, T.L.: 1984, A coaxial cable delay system for a synthesis radio telescope. *IEEE Trans. Instr. Meas.*, 78. DOI. ADS.

Lawson, K.D., Mayer, C.J., Osborne, J.L., Parkinson, M.L.: 1987, Variations in the spectral index of the galactic radio continuum emission in the northern hemisphere. *Mon. Not. Roy. Astron. Soc.* **205**, 307.

Liu, H., Zucca, P., Cho, K.-S., *et al.*: 2022, Interferometric Imaging, and Beam-Formed Study of a Moving Type-IV Radio Burst with LOFAR. *Solar Phys.* **297**, 115.

Lorimer, D.R., Kramer, M.: 2004, *Handbook of Pulsar Astronomy,* Vol.4, Cambridge University Press, Cambridge, UK.

Lorimer, D.R., Bailes, M., McLaughlin, M.A., *et al.*: 2007, A Bright Millisecond Radio Burst of Extragalactic Origin. *Science* **318**, 777.

Lundgren, S.C., Cordes, J.M., Ulmer, M., Matz, S.M., Lomatch, S., Foster, R.S., Hankins, T.: 1995, Giant Pulses from the Crab Pulsar: A Joint Radio and Gamma-Ray Study. *Astrophys. J.* **453**, 433. DOI. ADS.

Lyne, A., Graham-Smith, F.: 2012, *Pulsar astronomy*, 4th edn., *Cambridge Astrophysics*, Cambridge University Press, ???.

Lyne, A.G., Rickett, B.J.: 1968, Radio Observations of Five Pulsars. *Nature* **219**(5161), 1339. DOI. ADS.

Lyne, A.G., Smith, F.G.: 1968, Linear Polarization in Pulsating Radio Sources. *Nature* **218**(5137), 124. DOI. ADS.

Lyne, A.G., Smith, F.G., Graham, D.A.: 1971, Characteristics of the radio pulses from the pulsars. *Mon. Not. Roy. Astron. Soc.* **153**, 337. DOI. ADS.

Maan, Y.: 2015, Discovery of Low DM Fast Radio Transients: Geminga Pulsar Caught in the Act. *Astrophys. J.* **815**, 126.

Maan, Y., van Leeuwen, J., Vohl, D.: 2021, Fourier domain excision of periodic radio frequency interference. *Astron. Astrophys.* **650**, A80. DOI. ADS.

Malofeev, V.M., Gil, J.A., Jessner, A., *et al.*: 1994, Spectra of 45 pulsars. *Astron. Astrophys.* **285**, 201.

Malov, O.I., Malofeev, V.M.: 2010, Average pulse profiles of radio pulsars at 102 and 111 MHz. *Astron. Rep.* **54**, 210. DOI. ADS.

Manchester, R.N.: 2017, Pulsar timing and its applications. *Journal of Physics: Conference Series* **932**(1), 012002. DOI. https://dx.doi.org/10.1088/1742-6596/932/1/012002.

Manchester, R.N., Hobbs, G.B., Teoh, A., Hobbs, M.: 2005, The Australia Telescope National Facility Pulsar Catalogue. *Astron. J.* **129**(4), 1993. DOI. ADS.

Marcote, B., Nimmo, K., Hessels, J.W.T., Tendulkar, S.P., Bassa, C.G., Paragi, Z., Keimpema, A., Bhardwaj, M., Karuppusamy, R., Kaspi, V.M., Law, C.J., Michilli, D., Aggarwal, K., Andersen, B., Archibald, A.M., Bandura, K., Bower, G.C., Boyle, P.J., Brar, C., Burke-Spolaor, S., Butler, B.J., Cassanelli, T., Chawla, P., Demorest, P., Dobbs, M., Fonseca, E., Giri, U., Good, D.C., Gourdji, K., Josephy, A., Kirichenko, A.Y., Kirsten, F., Landecker, T.L., Lang, D., Lazio, T.J.W., Li, D.Z., Lin, H.-H., Linford, J.D., Masui, K., Mena-Parra, J., Naidu, A., Ng, C., Patel, C., Pen, U.-L., Pleunis, Z., Rafiei-Ravandi, M., Rahman, M., Renard, A., Scholz, P., Siegel, S.R., Smith, K.M., Stairs, I.H., Vanderlinde, K., Zwaniga, A.V.: 2020, A repeating fast radio burst source localized to a nearby spiral galaxy. *Nature* **577**(7789), 190. DOI. ADS.

Marsh, J.C.D.: 1992, Temperature contours of the radio sky at a wavelength of 2 metres. *J. British Astronomical Association* **102**, 31.

McLean, D.J., Labrum, N.R.: 1985, *Solar Radiophysics - Studies of emission from the Sun at metre wavelengths*, Cambridge University Press, Cambridge, UK.

Meyers, B.W., Tremblay, S.E., Ramesh Bhat, N.D., Shannon, R.M.: 2018, Spectral Flattening of Crab Giant Pulses at Low Frequencies. In: Weltevrede, P., Perera, B.B.P., Preston, L.L., Sanidas, S. (eds.) *Pulsar Astrophysics the Next Fifty Years* **337**, 378. DOI. ADS.

Mol, J.D., Romein, J.W.: 2011, The LOFAR Beam Former: Implementation and Performance Analysis. *arXiv:1105.0661*, 1.

Monstein, C., Ramesh, R., Kathiravan, C.: 2007, Radio spectrum measurements at the Gauribidanur observatory. *Bull. Astron. Soc. India* **35**, 473. ADS.

Morosan, D.E., Zucca, P., Bloomfield, D.S., Gallagher, P.T.: 2016, Conditions for electron-cyclotron maser emission in the solar corona. *Astron. Astrophys.* **589**, L8.

Morris, D., Kramer, M., Thum, C., Wielebinski, R., Grewing, M., Penalver, J., Jessner, A., Butin, G., Brunswig, W.: 1997, Pulsar detection at 87GHz. *Astron. Astrophys.* **322**, L17. ADS.

Mugundhan, V., Hariharan, K., Ramesh, R.: 2017, Solar Type IIIb Radio Bursts as Tracers for Electron Density Fluctuations in the Corona. *Solar Phys.* **292**, 155.

Mugundhan, V., Ramesh, R., Kathiravan, C., Gireesh, G.V.S., Hegde, A.: 2018, Spectropolarimetric Observations of Solar Noise Storms at Low Frequencies. *Solar Phys.* **293**, 41.

Murphy, T., Kaplan, D., Bell, M., Callingham, J., Croft, S., Johnston, S., Dobie, D., Zic, A., Hughes, J., Lynch, C., Hancock, P., Hurley-Walker, N., Lenc, E., Dwarakanath, K., For, B., Gaensler, B., Hindson, L., Johnston-Hollitt, M., Kapinska, A., Mckinley, B., Morgan, J., Offringa, A.R., Procopio, P., Staveley-Smith, L., Wayth, R., Wu, C., Zheng, Q.: 2017, Low-frequency spectral energy distributions of radio pulsars detected with the murchison widefield array. *Publications of the Astronomical Society of Australia* **34**. DOI.

Nakajima, H., Nishio, M., Enome, S., Shibasaki, K., Takano, T., Torii, C.: 1994, The Nobeyama radioheliograph. *Proc. IEEE.* **82**, 705. ADS.

Narayan, R.: 1992, The Physics of Pulsar Scintillation. *Philosophical Transactions of the Royal Society of London Series A* **341**(1660), 151. DOI. ADS.

Ng, C., Vanderlinde, K., Paradise, A., Mol, e.D.: 2017, CHIME FRB: An application of FFT beamforming for a radio telescope. *arXiv:1702.04728*, 1.

Noutsos, A., Sobey, C., Kondratiev, V.I., *et al.*: 2015, Pulsar polarisation below 200 MHz: Average profiles and propagation effects. *Astron. Astrophys.* **576**, A62.

Oppenheim, A.V., Schafer, R.W.: 2010, *Discrete-time signal processing / alan v. oppenheim, ronald w. schafer.*, Third edition. edn., *Prentice Hall signal processing series*, Pearson, Upper Saddle River [N.J. ISBN 9780131988422.

Parent, E., Chawla, P., Kaspi, V.M., Agazie, G.Y., Blumer, H., DeCesar, M., Fiore, W., Fonseca, E., Hessels, J.W.T., Kaplan, D.L., Kondratiev, V.I., LaRose, M., Levin, L., Lewis, E.F., Lynch, R.S., McEwen, A.E., McLaughlin, M.A., Mingyar, M., Al Noori, H., Ransom, S.M., Roberts, M.S.E., Schmiedekamp, A., Schmiedekamp, C., Siemens, X., Spiewak, R., Stairs, I.H., Surnis, M., Swiggum, J., van Leeuwen, J.: 2020, First Discovery of a Fast Radio Burst at 350 MHz by the GBNCC Survey. *Astrophys. J.* **904**(2), 92. DOI. ADS.

Pastor-Marazuela, I., Connor, L., van Leeuwen, J., Maan, Y., ter Veen, S., Bilous, A., Oostrum, L., Petroff, E., Straal, S., Vohl, D., Attema, J., Boersma, O.M., Kooistra, E., van der Schuur, D., Sclocco, A., Smits, R., Adams, E.A.K., Adebahr, B., de Blok, W.J.G., Coolen, A.H.W.M., Damstra, S., Dénes, H., Hess, K.M., van der Hulst, T., Hut, B., Ivashina, V.M., Kutkin, A., Loose, G.M., Lucero, D.M., Mika, Á., Moss, V.A., Mulder, H., Norden, M.J., Oosterloo, T., Orrú, E., Ruiter, M., Wijnholds, S.J.: 2021, Chromatic periodic activity down to 120 megahertz in a fast radio burst. *Nature* **596**(7873), 505. DOI. ADS.

Pastor-Marazuela, I., Connor, L., van Leeuwen, J., *et al.*: 2021, Chromatic periodic activity down to 120 MHz in a fast radio burst. *Nature* **596**, 505.

Petroff, E., Hessels, J.W.T., Lorimer, D.R.: 2022, Fast radio bursts at the dawn of the 2020s. *Astron. Astrophys. Rev.* **30**(1), 2. DOI. ADS.

Phillips, J.A., Wolszczan, A.: 1992, Precision Measurements of Pulsar Dispersion. *Astrophys. J.* **385**, 273. DOI. ADS.

Pilia, M., Hessels, J.W.T., Stappers, B.W., Kondratiev, V.I., Kramer, M., van Leeuwen, J.: 2016, Wide-band, low-frequency pulse profiles of 100 radio pulsars with LOFAR. *Astron. Astrophys.* **586**, A92. DOI. ADS.

Pilia, M., Burgay, M., Possenti, A., Ridolfi, A., Gajjar, V., Corongiu, A., Perrodin, D., Bernardi, G., Naldi, G., Pupillo, G., Ambrosino, F., Bianchi, G., Burtovoi, A., Casella, P., Casentini, C., Cecconi, M., Ferrigno, C., Fiori, M., Gendreau, K.C., Ghedina, A., Naletto, G., Nicastro, L., Ochner, P., Palazzi, E., Panessa, F., Papitto, A., Pittori, C., Rea, N., Castillo, G.A.R., Savchenko, V., Setti, G., Tavani, M., Trois, A., Trudu, M., Turatto, M., Ursi, A., Verrecchia, F., Zampieri, L.: 2020, The Lowest-frequency Fast Radio Bursts: Sardinia Radio Telescope Detection of the Periodic FRB 180916 at 328 MHz. *Astrophys. J. Lett.* **896**(2), L40. DOI. ADS.

Platts, E., Weltman, A., Walters, A., Tendulkar, S.P., Gordin, J.E.B., Kandhai, S.: 2019, A living theory catalogue for fast radio bursts. **821**, 1. DOI. ADS.

Pleunis, Z., Michilli, D., Bassa, C.G., *et al.*: 2021, LOFAR Detection of 110-188 MHz Emission and Frequency-dependent Activity from FRB 20180916B. *Astrophys J. Lett.* **911**, L3.

Popov, M.V., Kuz'min, A.D., Ul'yanov, O.M., Deshpande, A.A., Ershov, A.A., Zakharenko, V.V., Kondrat'ev, V.I., Kostyuk, S.V., Losovskiä, B.Y., Soglasnov, V.A.: 2006, Instantaneous radio spectra of giant pulses from the crab pulsar from decimeter to decameter wavelengths. *Astronomy Reports* **50**(7), 562. DOI. ADS.

Prabu, T., Srivani, K.S., Roshi, A.D., Kamini, P.A., Madhavi, S., Emrich, D.: 2015, A digital-receiver for the Murchisond Widefield Array. *Exp. Astron.* **39**, 73. DOI. ADS.

Price, D.C.: 2018, Spectrometers and Polyphase Filterbanks in Radio Astronomy. *arXiv:1607.03579v2 [astro-ph.IM]*, 1.

Ramesh, R.: 2011, Low frequency solar radio astronomy at the Indian Institute of Astrophysics. In: Choudhuri, A.R., Banerjee, D. (eds.) *1st Asia-Pacific Sol. Phys. Meeting*, *Astron. Soc. India Conf. Ser. 2*, 55. ADS.

Ramesh, R., Ebenezer, E.: 2001, Decameter Wavelength Observations of an Absorption Burst from the Sun and Its Association with an X2.0/3B Flare and the Onset of a "Halo" Coronal Mass Ejection. *Astrophys. J. Lett.* **558**, L141. DOI. ADS.

Ramesh, R., Sundara Rajan, M.S., Sastry, C.V.: 2006b, The 1024 channel digital correlator receiver of the Gauribidanur radioheliograph. *Exp. Astron.* **21**, 31. DOI. ADS.

Ramesh, R., Subramanian, K.R., Sundara Rajan, M.S., Sastry, C.V.: 1998, The gauribidanur radioheliograph. *Solar Phys.* **181**(2), 439.

Ramesh, R., Kathiravan, C., SatyaNarayanan, A., Ebenezer, E.: 2003, Metric observations of transient, quasi-periodic radio emission from the solar corona in association with a 'halo' CME and an 'EIT wave' event. *Astron. Astrophys.* **400**, 753.

Ramesh, R., SatyaNarayanan, A., Kathiravan, C., Sastry, C.V., UdayaShankar, N.: 2005, An estimation of the plasma parameters in the solar corona using quasi-periodic metric type III radio burst emission. *Astron. Astrophys.* **431**, 353.

Ramesh, R., Nataraj, H.S., Kathiravan, C., Sastry, C.V.: 2006, The Equatorial Background Solar Corona during Solar Minimum. *Astrophys. J.* **648**, 707.

Ramesh, R., Kathiravan, C., Sundara Rajan, M.S., Indrajit, V.B., Sastry, C.V.: 2008, A Low-Frequency (30 - 110 MHz) Antenna System for Observations of Polarized Radio Emission from the Solar Corona. *Solar Phys.* **253**, 319. ADS.

Ramesh, R., Kishore, P., Mulay, S.M., *et al.*: 2013, Low-frequency Observations of Drifting, Non-thermal Continuum Radio Emission Associated with the Solar Coronal Mass Ejections. *Astrophys. J.* **778**, 30.

Ramesh, R., Kathiravan, C., Sundara Rajan, M.S., Indrajit, V.B., Rajalingam, M.: 2014, Solar observations at low frequencies with the Gauribidanur radioheliograph. In: Chengalur, J.N., Gupta, Y. (eds.) *The Metrewavelength Sky*, *Astron. Soc. India Conf. Ser. 13*, 19. ADS.

Ramesh, R., Kumari, A., Kathiravan, C., *et al.*: 2020, Low-Frequency Radio Observations of the 'Quiet' Corona During the Descending Phase of Sunspot Cycle 24. *Geophys. Res. Lett.* **47**, e90426.

Ramkumar, P.S., Prabu, M. T.and Girimaji, Markendeyalu, G.: 1994, A Digital Signal Pre-Processor for Pulsar Search. *J. Astrophys. Astron.* **15**, 343. ADS.

Rankin, J.M.: 1993, Toward an Empirical Theory of Pulsar Emission. VI. The Geometry of the Conal Emission Region. *Astrophys. J.* **405**, 285. DOI. ADS.

Rankin, J.M., Comella, J.M., Craft, J. H. D., Richards, D.W., Campbell, D.B., Counselman, I. C. C.: 1970, Radio Pulse Shapes, Flux Densities, and Dispersion of Pulsar NP 0532. *Astrophys. J.* **162**, 707. DOI. ADS.

Ransom, S.: 2011, PRESTO: PulsaR Exploration and Search TOolkit. *Astrophysics Source Code Library, record ascl:1107.017*. ADS.

Ravi, V., Catha, M., D'Addario, L., Djorgovski, S.G., Hallinan, G., Hobbs, R., Kocz, J., Kulkarni, S.R., Shi, J., Vedantham, H.K., Weinreb, S., Woody, D.P.: 2019, A fast radio burst localized to a massive galaxy. *Nature* **572**(7769), 352. DOI. ADS.

Reddy, S.H., Kudale, S., Gokhale, U., Halagalli, I., Raskar, N., Kishalay de: 2017, A Wide-band Digital Back-End for the Upgraded GMRT. *J. Astron. Instr.* **6**, 1641011. DOI. ADS.

Rickett, B.J., Seiradakis, J.H.: 1982, The flux of the Crab pulsar at 74 MHz from 1971 to 1981. *Astrophys. J.* **256**, 612. DOI. ADS.

Rickett, B., Johnston, S., Tomlinson, T., Reynolds, J.: 2009, The inner scale of the plasma turbulence towards PSR J16444559. *Monthly Notices of the Royal Astronomical Society* **395**(3), 1391. DOI. https://doi.org/10.1111/j.1365-2966.2009.14471.x.

Romani, R.W., Johnston, S.: 2001, Giant pulses from the millisecond pulsar b1821–24. *The Astrophysical Journal* **557**(2), L93. DOI. https://dx.doi.org/10.1086/323415.

Rumsey, V.H.: 1957, Frequency Independent Antennas. *IRE Nat. Conven. Record* **5**, 114.

Ryabov, V.B., Vavriv, D.M., Zarka, P., Ryabov, B.P., Kozhin, R., Vinogradov, V.V., Denis, L.: 2010, A low-noise, high-dynamic-range, digital receiver for radio astronomy applications: an efficient solution for observing radio-bursts from Jupiter, the Sun, pulsars, and other astrophysical plasmas below 30 MHz. *Astron. Astrophys.* **510**, A16. DOI. ADS.

Saint-Hilaire, P., Benz, A.O., Monstein, C.: 2014, Short-duration Radio Bursts with Apparent Extragalactic Dispersion. *Astrophys. J.* **795**, 19.

Sasikumar Raja, K., Kathiravan, C., Ramesh, R., Rajalingam, M., Barve, I.V.: 2013, Design and Performance of a Low-frequency Cross-polarized Log-periodic Dipole Antenna. *Astrophys. J. Suppl. Ser.* **207**, 2.

Sastry, C.V.: 1995, The decameter and meterwave radiotelescopes in India and Mauritius. *Space Sci. Rev.* **72**, 629.

Scheuer, P.A.G.: 1968, Amplitude Variations in Pulsed Radio Sources. *Nature* **218**(5145), 920. DOI. ADS.

Seiradakis, J.H., Wielebinski, R.: 2004, Morphology and characteristics of radio pulsars. *The Astronomy and Astrophysics Review* **12**, 239. https://api.semanticscholar.org/CorpusID:13905437.

Sharma, R., Oberoi, D., Battaglia, M., Krucker, S.: 2022, Detection of Ubiquitous Weak and Impulsive Nonthermal Emissions from the Solar Corona. *Astrophys. J.* **937**, 99.

Sieber, W.: 1973, Pulsar Spectra. *Astron. Astrophys.* **28**, 237. ADS.

Smirnova, T.V.: 2012, Giant pulses from the pulsar PSR B0950+08. *Astronomy Reports* **56**(6), 430. DOI. ADS.

Sokolowski, M., Wayth, R., Bhat, N.D.R., *et al.*: 2021, A Southern-Hemisphere all-sky radio transient monitor for SKA-Low prototype stations. *Publ. Astron. Soc. Aust.* **38**, e023.

Spitler, L.G., Scholz, P., Hessels, J.W.T., Bogdanov, S., Brazier, A., Camilo, F., Chatterjee, S., Cordes, J.M., Crawford, F., Deneva, J., Ferdman, R.D., Freire, P.C.C., Kaspi, V.M., Lazarus, P., Lynch, R., Madsen, E.C., McLaughlin, M.A., Patel, C., Ransom, S.M., Seymour, A., Stairs, I.H., Stappers, B.W., van Leeuwen, J., Zhu, W.W.: 2016, A repeating fast radio burst. *Nature* **531**(7593), 202. DOI. ADS.

Staelin, D.H., Reifenstein, E.C. III: 1968, Pulsating radio sources near the crab nebula. *Science, 162: 1481-3(Dec. 27, 1968).* DOI. `https://www.osti.gov/biblio/4807226`.

Stappers, B.W., Hessels, J.W.T., Alexov, A., Anderson, K., Coenen, T., Hassall, T., Karastergiou, A., Kondratiev, V.I., Kramer, M., van Leeuwen, J., Mol, J.D., Noutsos, A., Romein, J.W., Weltevrede, P., Fender, R., Wijers, R.A.M.J., Bähren, L., Bell, M.E., Broderick, J., Daw, E.J., Dhillon, V.S., Eislöffel, J., Falcke, H., Griessmeier, J., Law, C., Markoff, S., Miller-Jones, J.C.A., Scheers, B., Spreeuw, H., Swinbank, J., Ter Veen, S., Wise, M.W., Wucknitz, O., Zarka, P., Anderson, J., Asgekar, A., Avruch, I.M., Beck, R., Bennema, P., Bentum, M.J., Best, P., Bregman, J., Brentjens, M., van de Brink, R.H., Broekema, P.C., Brouw, W.N., Brüggen, M., de Bruyn, A.G., Butcher, H.R., Ciardi, B., Conway, J., Dettmar, R.-J., van Duin, A., van Enst, J., Garrett, M., Gerbers, M., Grit, T., Gunst, A., van Haarlem, M.P., Hamaker, J.P., Heald, G., Hoeft, M., Holties, H., Horneffer, A., Koopmans, L.V.E., Kuper, G., Loose, M., Maat, P., McKay-Bukowski, D., McKean, J.P., Miley, G., Morganti, R., Nijboer, R., Noordam, J.E., Norden, M., Olofsson, H., Pandey-Pommier, M., Polatidis, A., Reich, W., Röttgering, H., Schoenmakers, A., Sluman, J., Smirnov, O., Steinmetz, M., Sterks, C.G.M., Tagger, M., Tang, Y., Vermeulen, R., Vermaas, N., Vogt, C., de Vos, M., Wijnholds, S.J., Yatawatta, S., Zensus, A.: 2011, Observing pulsars and fast transients with LOFAR. *Astron. Astrophys.* **530**, A80. DOI. ADS.

Stein, M.S.: 2019, Glancing Through Massive Binary Radio Lenses: Hardware-Aware Interferometry With 1-Bit Sensors. DOI. ADS.

Steinberg, J.L., Aubier-Giraud, M., Leblanc, Y., Boischot, A.: 1971, Coronal Scattering, Absorption and Refraction of Solar Radiobursts. *Astron. Astrophys.* **10**, 362. ADS.

Stovall, K., Ray, P.S., Blythe, J., Dowell, J., Eftekhari, T., Garcia, A.: 2015, Pulsar Observations Using the First Station of the Long Wavelength Array and the LWA Pulsar Data Archive. *Astrophys. J.* **808**, 156. DOI. ADS.

Tan, C.M., Bassa, C.G., Cooper, S., Dijkema, T.J., Esposito, P., Hessels, J.W.T., Kondratiev, V.I., Kramer, M., Michilli, D., Sanidas, S., Shimwell, T.W., Stappers, B.W., van Leeuwen, J., Cognard, I., Grießmeier, J.-M., Karastergiou, A., Keane, E.F., Sobey, C., Weltevrede, P.: 2018, LOFAR Discovery of a 23.5 s Radio Pulsar. *Astrophys. J.* **866**(1), 54. DOI. ADS.

Taylor, G.B., Ellingson, S.W., Kassim, N.E., Craig, J., Dowell, J., Wolfe, C.N.: 2012, First Light for the First Station of the Long Wavelength Array. *J. Astron. Instr.* **1**, 1250004. DOI. ADS.

Taylor, J.H., Cordes, J.M.: 1993, Pulsar Distances and the Galactic Distribution of Free Electrons. *Astrophys. J.* **411**, 674. DOI. ADS.

Taylor, J.H., Huguenin, G.R.: 1969, Two new pulsating radio sources. *Nature* **221**, 816. https://api.semanticscholar.org/CorpusID:11307295.

Taylor, J.H., Manchester, R.N.: 1977, Recent observations of pulsars. *Annurev.aa.* **15**, 19. DOI. ADS.

Taylor, J.H., Stinebring, D.R.: 1986, Recent progress in the understanding of pulsars. *Annurev.aa.* **24**, 285. DOI. ADS.

Teng, H.F., Zhang, U.H., Chiueh, T.H., Wong, S.K., Li, H.H., Chen, Y.L.: 2015, Ultrawideband 1-b Digital Spectrometer. *IEEE Trans. Instr. Meas.* **64**, 299. ADS.

The CHIME/FRB Collaboration: 2020, A bright millisecond-duration radio burst from a Galactic magnetar. *Nature* **587**, 54.

Thompson, A.R., Moran, J.M., Swenson, J. George W.: 2017, *Interferometry and Synthesis in Radio Astronomy, 3rd Edition*. DOI. ADS.

Thornton, D., Stappers, B., Bailes, M., *et al.*: 2013, A Population of Fast Radio Bursts at Cosmological Distances. *Science* **341**, 53.

Thorsett, S.E.: 1991, Frequency Dependence of Pulsar Integrated Profiles. *Astrophys. J.* **377**, 263.

Thorsett, S.E.: 1992, Radius-to-frequency mapping in the radio pulsar emission mechanism. *International Astronomical Union Colloquium* **128**, 143–146. DOI.

Tingay, S.J., Goeke, R., Bowman, J.D., *et al.*: 2013, The Murchison Widefield Array: The Square Kilometre Array Precursor at Low Radio Frequencies. *Publ. Astron. Soc. Aust.* **30**, e007.

Tremblay, S.E., Ord, S.M., Bhat, N.D.R., Tingay, S.J., Crosse, B., Pallot, D.: 2015, The High Time and Frequency Resolution Capabilities of the Murchison Widefield Array. *Pub. Astron. Soc. Pac.* **32**, e005. DOI. ADS.

Udaya Shankar, N., Ravi Shankar, T.S.: 1990, A digital correlation receiver for the GEETEE radio telescope. *J. Astrophys. Astron.* **11**, 297. DOI. ADS.

van Haarlem, M.P., Wise, M.W., Gunst, A.W., Heald, G., McKean, J.P., Hessels, J.W.T.: 2013, LOFAR: The LOw-Frequency ARray. *Astron. Astrophys.* **556**, A2. DOI. ADS.

Van Vleck, J.H., Middleton, D.: 1966, The Spectrum of Clipped Noise. *Proc. IEEE* **54**, 2. DOI. ADS.

Vasanth, V., Chen, Y., Lv, M., *et al.*: 2019, Source Imaging of a Moving Type IV Solar Radio Burst and Its Role in Tracking Coronal Mass Ejection from the Inner to the Outer Corona. *Astrophys. J.* **870**, 30.

Vivekanand, M., Narayan, R., Radhakrishnan, V.: 1982, On selection effects in pulsar searches. *Journal of Astrophysics and Astronomy* **3**, 237. DOI. ADS.

Wayth, R., Sokolowski, M., Booler, T., *et al.*: 2017, The Engineering Development Array: A Low Frequency Radio Telescope Utilising SKA Precursor Technology. *Publ. Astron. Soc. Aust.* **34**, e034.

Weinreb, S.: 1963, Clipping loss in the one-bit autocorrelation spectral line receiver. *Ph.D Thesis, MIT Tech. Rep. 412*. ADS.

Xue, M., Bhat, N.D.R., Tremblay, S.E., Ord, S.M., Sobey, C., Swainston, N.A., Kaplan, D.L., Johnston, S., Meyers, B.W., McSweeney, S.J.: 2017, A census of southern pulsars at 185 mhz. *Publications of the Astronomical Society of Australia* **34**, e070. DOI.

Zakharenko, V.V., Vasylieva, I.Y., Konovalenko, A.A., Ulyanov, O.M., Serylak, M., Zarka, P.: 2013, Detection of decametre-wavelength pulsed radio emission of 40 known pulsars. *Mon. Not. Roy. Astron. Soc.* **431**, 3624. DOI. ADS.

Zakharenko, V., Konavalenko, A.A., Zarka, P., Ulyanov, O., Sidorchuk, M., Stepkin, S.: 2016, Digital Receivers for Low-Frequency Radio Telescopes UTR-2, URAN, GURT. *J. Astron. Instr.* **5**, 1641010. DOI. ADS.

Zarka, P., Denis, L., Tagger, M., Girard, J.N., Coffre, A., Dumez-Viou, C.: 2020, The low-frequency radio telescope NenuFAR. In: *URSI GASS 2020, Session J01 New Telescopes on the Frontier*, *https://tinyurl.com/ycocd5ly*.

Appendices

Chapter A

Log Periodic Dipole Antenna

The basic component of any trans-receiver system is the Antenna. The antenna is a device used to transmit and receive electromagnetic (EM) radiation. It converts electrical energy to EM energy in the case of transmission and vice versa during reception. Depending upon the structure, there are many types of antennas: Wired (e.g., dipole antenna), Aperture (e.g., Horn antenna), Microstrip antenna, etc. The antenna used in this instrument is the *Log Periodic Dipole Antenna (LPDA)*.

LPDA is an array of dipole antennas stacked into a common axis in a systematic pattern. The geometry of the structure varies in such a way that its response characteristics, such as input impedance, Voltage standing wave ratio (VSWR), and Radiation pattern are a periodic function of the logarithm of frequency (DuHamel and Isbell, 1957). The advantage of using LPDA is that it's a broadband, highly directional antenna whose characteristics remain almost constant over a wide range of frequencies. LPDAs are typically used as receiving elements in low-frequency radio astronomy (<1GHz), particularly where observations over a wide range of frequencies are required (see e.g. Ebenezer *et al.*, 2001; Ramesh *et al.*, 2008).

A.1 Design of LPDA

The design of LPDA is based on the formulation given in Carrell (1961). Figure A.1 shows a basic schematic of the LPDA. A series of dipoles are stacked together on a transmission line symmetrically such that

$$\frac{L_n}{L_{n+1}} = \frac{S_n}{S_{n+1}} = \tau \tag{A.1}$$

where τ is the design constant, L_n, L_{n+1} are he length of the adjacent dipole elements, and S_n, S_{n+1} are the successive spacing between the elements. And,

$$tan(\alpha) = \frac{L_{n+1} - L_n}{4\sigma} \tag{A.2}$$

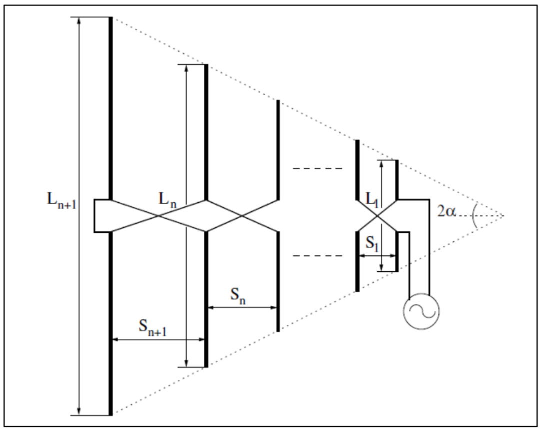

Figure A.1: Schematic of the Log Periodic Dipole Antenna. Courtesy: Kishore (2016)

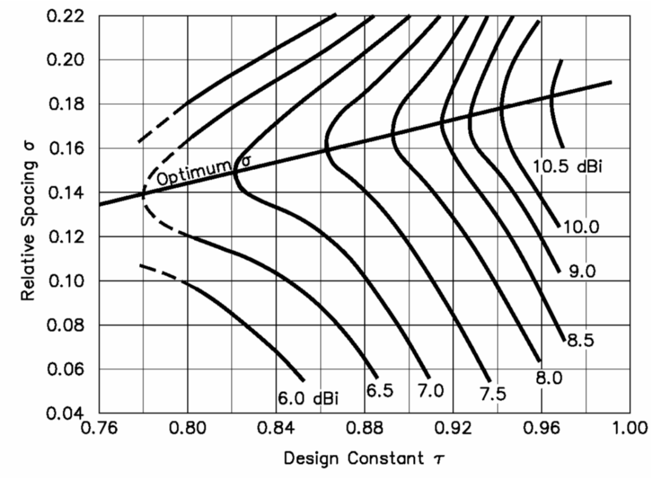

Figure A.2: Relation between τ, σ and gain. Figure taken from Carrell (1961)

where σ is the spacing factor and α is the half apex angle. Figure A.2 shows various combinations of τ and σ plotted against gain values. The optimum design corresponds to the one that has a minimum number of dipoles to cover the maximum bandwidth. Such a design is obtained by choosing the parameters from the straight line shown in the figure.

The LPDA design for this new array is as developed for GLOSS (Gauribidanur low-frequency solar spectrograph) by Kishore *et al.* (2014) with $\tau = 0.88$ and $\sigma = 0.077$. For the frequency range of 40-440 MHz, the number of elements is 19, with an extra 4 elements as reflectors and directors to take care of lower and higher frequency cut-offs, and $\alpha = 22°$ (Kishore, 2016). Figure A.3 shows one of the LPDAs installed in the Gauribidanur Pulsar System (GAPS) array. The dipoles are oriented in the North-South direction.

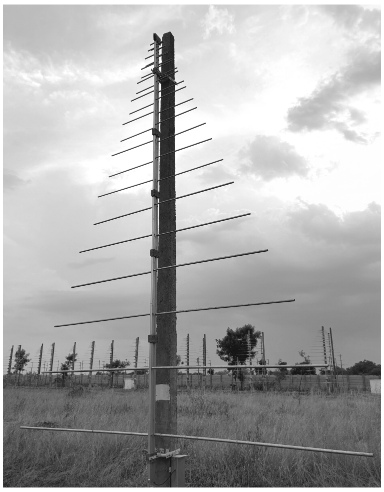

Figure A.3: The LPDA used for GAPS

A.1.1 LPDA characterization

A.1.1.1 VSWR

Due to the mismatch of impedance between the transmission line and antenna, the transmitted power will be reflected back into the transmission line, causing a standing wave. *Voltage standing wave ratio (VSWR)* is the ratio of maximum amplitude to the minimum amplitude of the standing wave. VSWR is a function of the reflection coefficient, Γ.

$$VSWR = \frac{1 + |\Gamma|}{1 - |\Gamma|} \tag{A.3}$$

where, $\Gamma = V_{reflected}/V_{incident} = (Z_L - Z_\circ)/(Z_L + Z_\circ)$. Here, Z_L is load impedance, and $Z_\circ$ is the characteristic impedance of the transmission line. If both are equal, then the line is matched, and all power is transferred to the load. If there is a mismatch between these two, then there will be a reflected wave traveling in the backward direction. This will create standing waves in the transmission line, which will lead to the loss of transmitted power. The smaller the VSWR is, the better the antenna is matched to the transmission line, and the more power is delivered. In general, if VSWR is < 2, the antenna impedance is said to be matched well with that of the load with transmission efficiency $\eta = 1 - \Gamma^2 > 90\%$. The LPDA is designed with the characteristic impedance of 50Ω.

VSWR was measured using an RF Vector Network Analyzer (N9923A)* Figure A.4 shows the VSWR, reflection coefficient, and transmission efficiency of one of the LPDAs used in the array. VSWR is < 2 throughout its entire operating band.

---

*https://www.keysight.com/in/en/product/N9923A/fieldfox-a-handheld-rf-vector-network-analyzer-4-gl
html

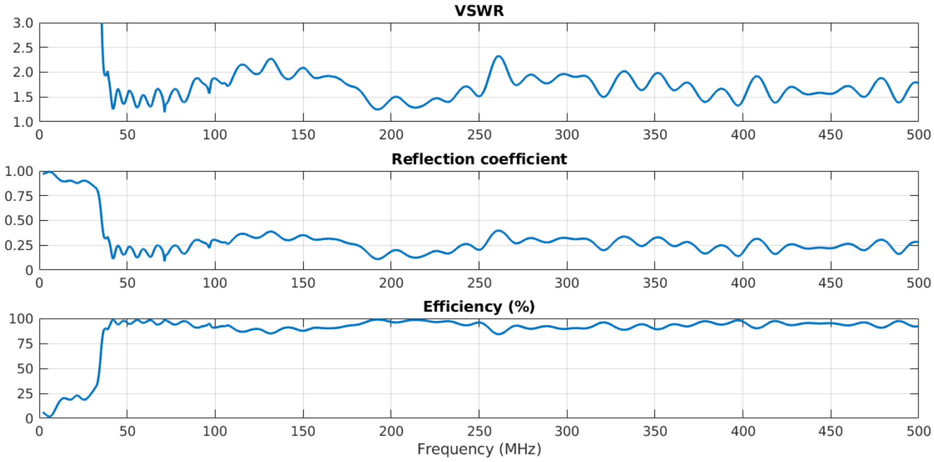

Figure A.4: LPDA characteristics

A.1.1.2 Radiation pattern

The antenna radiation pattern is a graphical representation of the radiation properties of the antenna as a function of direction. The field surrounding the antenna is divided into three principal regions: Reactive near field, Radiating near (Fresnel) field, and Far-field (Fraunhofer region). The far-field region is the most important as it determines the antenna's radiation pattern. In this region, the radiation pattern doesn't change the shape, although the Electric field falls as $1/R$ and power falls as $1/R^2$, where R is the distance from the antenna to the test point. If D is the maximum dimension of the antenna, then the following 3 conditions must be satisfied to be in the far field region: $R > 2D^2/\lambda, R >> D, and R >> \lambda$, where λ is the wavelength. For the designed LPDA, R is about 4.6 m for 50 MHz frequency.

The far-field radiation pattern of the LPDA was measured in the two principal planes, i.e., the E-plane and the H-plane. The E-plane is the plane in which dipoles of the LPDA are oriented, and the H-plane is the plane orthogonal to it. We kept transmitter and receiver antennas at a distance of 25 m. Both antennas were oriented along the same plane, and then the receiver antenna was rotated by 360° (azimuthal plane) from the reference position, and the received power levels were noted for every 10°. In order to measure the E-plane, both antennas were oriented horizontally, and for the H-plane, they were oriented vertically. Figure A.5 shows the schematic of the setup, and figure A.6 shows the on-field measurement. Figure A.7 shows the E-plane and H-plane radiation patterns of the LPDA at different frequencies. We see that E-plane Half power beam width (HPBW) is $\sim 80°$ and H-plane HPBW is about $\sim 110°$, which are almost constant for different frequencies.

Figure A.5: Setup for radiation pattern measurement

Figure A.6: Radiation pattern measurement for E-plane (Left) and H-plane (Right)

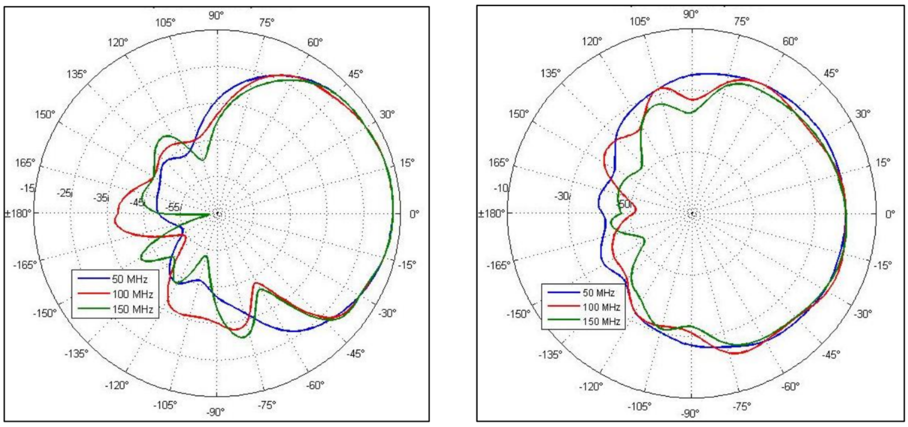

Figure A.7: Radiation pattern of LPDA: E-plane (Left) and H-plane (Right)

A.1.1.3 Gain and aperture

The directive gain is the ratio of radiation intensity in a given direction of the antenna to that of an isotropic radiator. The Directivity, i.e., the maximum directive gain, is related to HPBWs along the E and H-planes as

$$Directivity(D) = \frac{4\pi}{\Omega_A}. \tag{A.4}$$

Here, Ω_A is the beam solid angle given as $\Omega_A = HPBW_E \times HPBW_H$. Putting HPBW in the E and H plane as 80° and 110°, we get the directivity or the gain $\sim 6.5dBi$.

Table A.1: Parameters of the LPDA.

Parameter	**Value**
Operating frequency	40-440 MHz
Number of elements	23
Length	460 cm
Shortest arm length	9.9 cm
Longest arm length	187.5 cm
Half apex angle	22°
HPBW E-plane	80°
HPBW H-plane	110°
Gain	6.5 dBi
Effective area	$0.36\lambda^2$
VSWR	< 2

The effective aperture or the effective collecting area describes how effectively the antenna receives radiation.

$$A_e = \frac{D\lambda^2}{4\pi} \approx 0.36\lambda^2. \tag{A.5}$$

Table A.1 summarizes the parameters of the LPDA used in this work.

Chapter B
Antenna array beam

Array Theory

Consider two isotropic point element sources separated by distance d as shown in figure B.1. Taking the reference point for phase halfway between the sources, the far field pattern in the direction θ is given as

$$E(\theta) = E_1 e^{j\psi/2} + E_2 e^{-j\psi/2} \tag{B.1}$$

where, $\psi = kdsin(\theta) + \delta$

$k = 2\pi/\lambda$ is the wavenumber, and δ is the intrinsic phase difference between the two sources. E_1 and E_2 are the amplitudes of the electric field due to the two sources at the distant point under consideration. If the two sources have equal strength, $E_1 = E_2 = E_0$ we get

$$E(\theta) = 2E_0 cos(\psi/2) \tag{B.2}$$

By the reciprocity theorem, $E(\theta)$ also represents the voltage reception pattern obtained when the signals from the two antenna elements are added after introducing the phase shift δ between them. If the individual elements are considered to have identical beam patterns $E_i(\theta)$, then equation B.2 is modified as

$$E(\theta) = 2E_i(\theta) cos(\psi/2). \tag{B.3}$$

$E_i(\theta)$ is called the *primary pattern* and the *cos* factor is called the *array pattern.*

For n isotropic sources of equal amplitude and spacing, the far field pattern considering the first element as phase reference is

$$E(\theta) = E_0(1 + e^{j\psi} + e^{j2\psi} + e^{j3\psi} + . \quad . \quad . \quad + e^{j(n-1)\psi}) \tag{B.4}$$

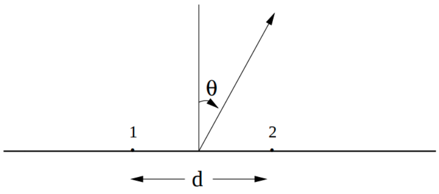

Figure B.1: Array of 2 isotropic point sources (Credit: NCRA)

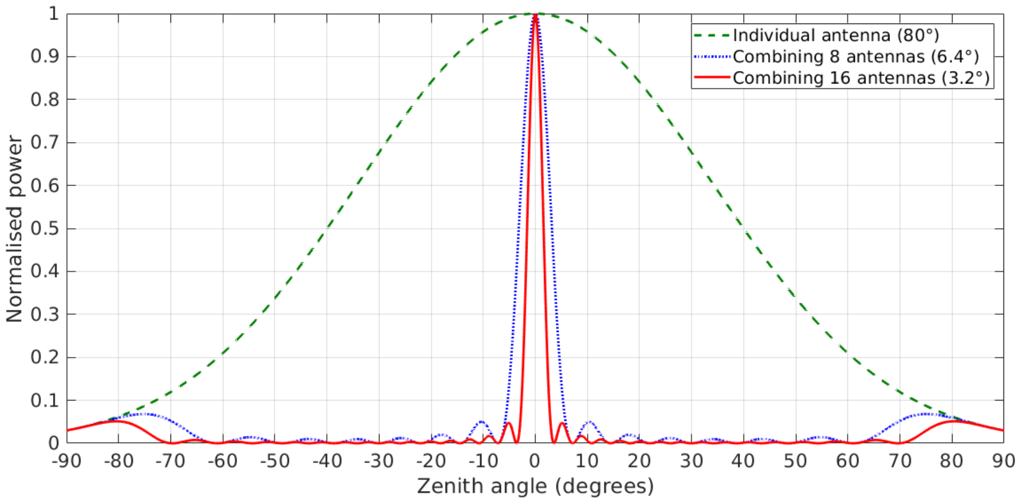

Figure B.2: Simulation of GAPS array beam at 60 MHz. The half-power beam widths (HPBW) are shown in the brackets.

Which can be reduced to

$$E(\theta) = E_0 \frac{sin(n\psi/2)}{sin(\psi/2} e^{j(n-1)\psi/2} \tag{B.5}$$

If the center of the array is chosen as the reference for the phase, the exponential term in the above equation is eliminated. Then, the field pattern will have maximum value nE_0 when $\psi = 0, 2\pi, 3\pi, ...$. The maxima at $\psi = 0$ is called the *main lobe*, and the maxima at other values of ψ are called *grating lobes*. By suitable choice of the value of δ, this maxima can be "steered" to different values of θ, using the relation $kdsin\theta = -\delta$.

For GAPS, 16 LPDAs are arranged with 5 m spacing between them. The array is oriented North-South with their E-planes in that direction. The HPBW of the LPDAs in their E-planes is $\sim 80°$. Using the above equations, the array beam can be simulated, which is shown in figure B.2 as a function of the zenith angle. At a frequency of 60 MHz, the HPBW of the array beam reduces to $\sim 6.4°$ when 8 antennas are combined and to $\sim 3.2°$ for 16 antennas.

Chapter C
Signal chain components

Here, we list the different components that have been used in the signal chain of GAPS.

C.1 Analog components

C.1.1 Amplifier

Low noise amplifier (LNA) MAN 1-LN* is used to provide a gain of ∼30 dB to the RF signal. Its operating frequency is 0.5-500 MHz, with a low noise figure of ∼3dB. The amplifier IC is integrated along with a High pass filter (PHP-50)† that has a cut-off of 35 MHz on the same PCB enclosed in a metal casing, as shown in the figure C.1. The high pass filter is used to reject any low-frequency artifacts that may enter the amplifier and saturate it. The S parameters of the amplifier + filter circuit are measured using an RF Vector network analyzer and are shown in figure C.1. S11 and S22 are the VSWR of the input and output ports, respectively. S21 is the forward gain, and S12 is the reverse gain or the isolation.

C.1.2 Filters

Low pass filter 85 MHz:

A 5-stage constant-K low pass filter with a cut-off frequency of 85 MHz is used to block the high-frequency signals, including the strong FM band(88-108 MHz). Constant-K filters are made using a combination of series inductors and shunt capacitors. One "T" section of the filter has inductors of 93 nH and a capacitor of 75 pF, which gives the desired cutoff at ∼85 MHz. Adding multiple stages gives a sharper roll-off, ∼20 dB/10 MHz. It offers ∼80 dB isolation in its stopband. Its circuit and characteristics are shown in figure C.2.

---

*https://www.minicircuits.com/pdfs/MAN-1LN.pdf

†https://www.minicircuits.com/pdfs/PHP-50+.pdf

Band pass filter 50-70 MHz:

A two-stage filter using Bandpass filter PBP-60[‡] is used to limit the RF band to 50-70 MHz before it enters the ADC in the digital beamforming system, as discussed in Chapter 3 and 4. The insertion loss in the passband is ∼2 dB while that in the stopband is ∼60 dB. Figure C.3 shows the circuit and its S parameters.

Band pass filter 50-80 MHz:

In the prototype system (see Chapter 2), two bandpass filters with a 50-80 MHz pass band were used before feeding the RF signals to the ADC to attenuate any spurious pick-up outside the band. The filter from Spectrum Microwave (has ∼1 dB insertion loss and a sharp roll off of ∼70 dB/10 MHz. The characteristics of the filter are shown in figure C.4.

C.1.3 Power combiner

A power combiner is used to combine two signals coherently. Four two-way power splitter/combiners (PSC2-1)[§] are used to make an eight-way power combiner used to combine signals from 8 antennas in the prototype system, as seen in Chapter 2. A two-way power combiner and its characteristics are shown in the figure C.5.

C.2 Digital Components

C.2.1 Analog to Digital converter

An ADC4x250-8 [¶] card is used to convert analog RF signals to digital. It has four AD9480[‖] ICs. It supports 8-bit sampling up to 250 MSPS for the four channels. It is clocked using an Agilent E4423B signal generator.

C.2.2 ROACH board

ROACH (Reconfigurable Open Architecture Computing Hardware) is a standalone FPGA processing board [**] from CASPER (The Collaboration for Astronomy Signal Processing and Electronics Research)[††] (Hickish *et al.*, 2016). It has Xilinx Virtex-5 FPGA. The onboard FPGA can be programmed, and interfacing can be done between the FPGA software registers, BRAMs, FIFOs and external devices using 1 Gb Ethernet. The data is acquired using 10 Gb Ethernet. Communication with the ROACH board is done using a Python interface.

[‡] `https://www.minicircuits.com/pdfs/PBP-60+.pdf`

[§] `https://www.minicircuits.com/pdfs/PSC-2-1.pdf`

[¶] `https://casper.astro.berkeley.edu/wiki/ADC4x250-8`

[‖] `https://www.analog.com/en/products/ad9480.html`

[**] `https://casper.astro.berkeley.edu/wiki/ROACH`

[††] `https://casper.berkeley.edu/`

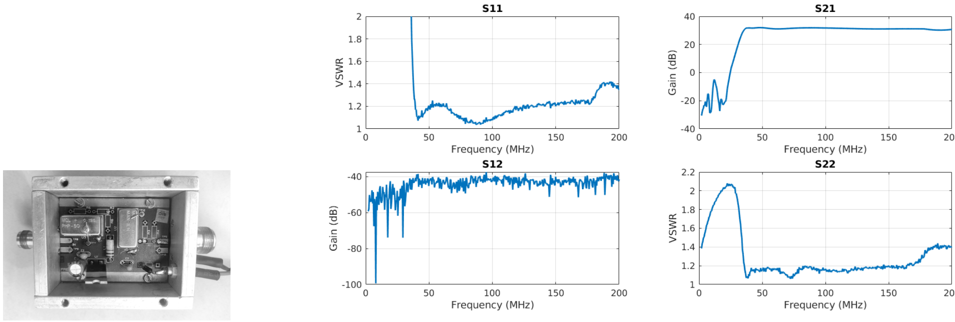

(a) Circuit **(b)** Characteristics

Figure C.1: Low noise amplifier

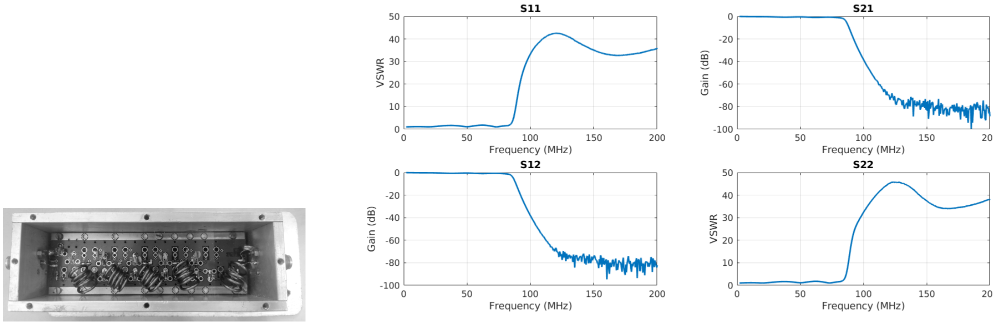

(a) Circuit **(b)** Characteristics

Figure C.2: Low pass filter 85 MHz

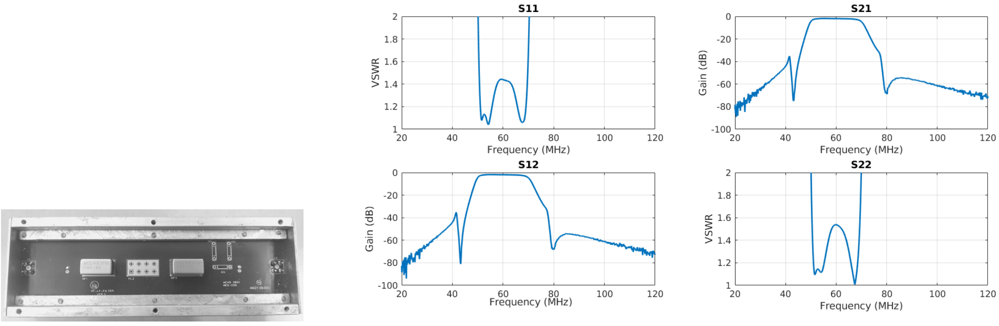

(a) Circuit **(b)** Characteristics

Figure C.3: Band pass filter 50-70 MHz

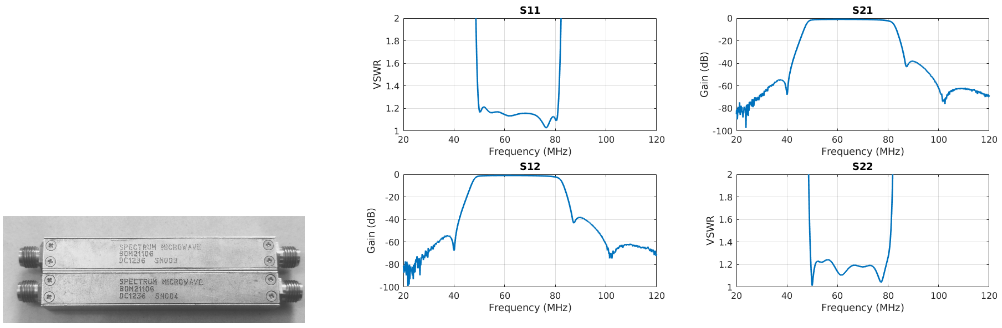

(a) Filters **(b)** Characteristics

Figure C.4: Band pass filter 50-80 MHz

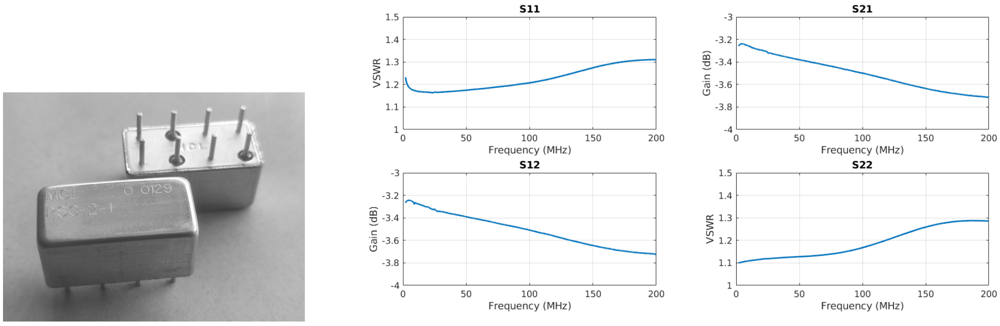

(a) PSC2-1 IC **(b)** PSC2-1 Characteristics

Figure C.5: Power combiner

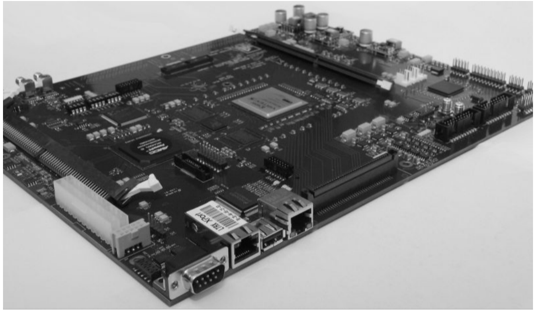

Figure C.6: ROACH board

Chapter D

Polyphase filterbank

In digital spectrometers, signals from the time domain are converted to the frequency domain. This can done using the Discrete Fourier Transform (DFT). The N-point DFT of a discrete sequence $x(n)$ is given as

$$X(k) = \sum_{n=0}^{N-1} x(n) e^{-j2\pi \frac{kn}{N}} \qquad k = 0, 1, 2 \ldots, N-1 \tag{D.1}$$

Fast Fourier Transform (FFT) is an efficient algorithm for computation of the DFT (Cooley and Tukey, 1965). The DFT is computed over a finite number of samples, i.e., the window length. As the window length is not infinite, the response of DFT is not perfect. This can be thought of in this way- the ideal Fourier transform is computed over infinite points. However, we have a limited number of points as the signal is time-limited, which is an infinite signal multiplied by a rectangular function. So, its Fourier transform is the ideal Fourier transform convolved with a sine function. This means each channel has a non-zero response over all frequencies. This results in unwanted responses to adjacent channels or 'spectral leakage.' This is undesirable since strong spectral features in other channels can suppress faint spectral features.

The effects of spectral leakage can be reduced by altering the signal prior to the DFT. Windowing functions reduce the sidelobes of DFT. They are applied by multiplying the signal by a weighting function $w(n)$. So,

$$X_w(k) = \sum_{n=0}^{N-1} w(n) x(n) e^{-j2\pi \frac{kn}{N}} = W(k) * X(k) \tag{D.2}$$

There is a wide range of windowing functions like Bartlett, Hanning, Hamming, Blackman, and Kaiser (Oppenheim and Schafer, 2010). However, such functions reduce the size of the sidelobes at the expense of a wider main lobe.

The effects of spectral leakage can be further reduced while achieving a well-defined main lobe if additional samples of the original signal are available (Harris and Haines,

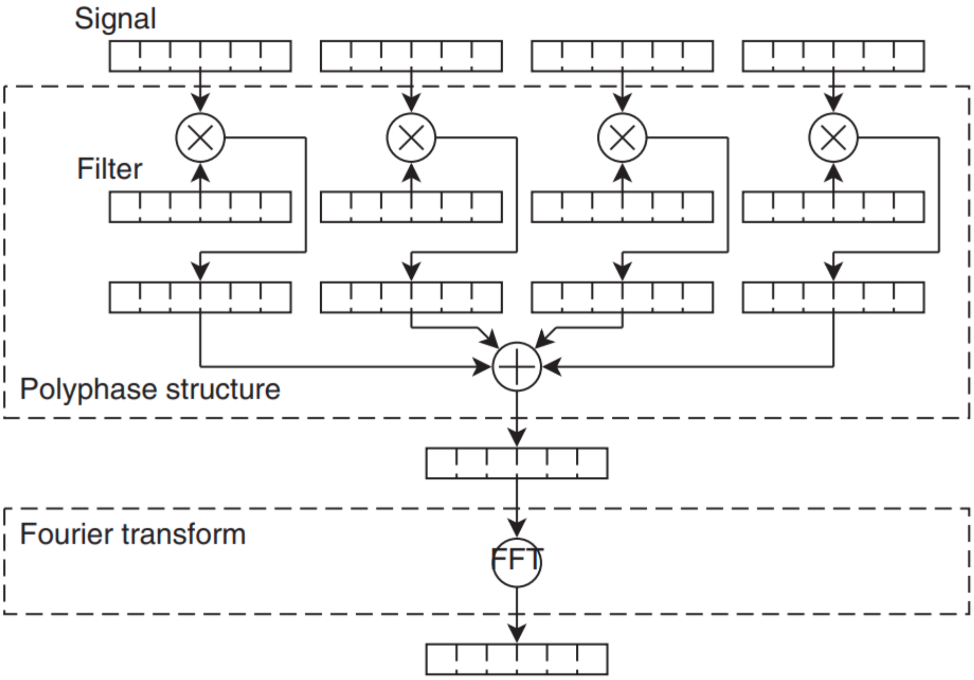

Figure D.1: Graphical representation of polyphase filterbank with 4 taps. Figure taken from Harris and Haines (2011).

2011). This is achieved using the Polyphase filterbank technique (Price, 2018). In this technique, instead of taking an N-point transform directly, $N \times P = M$ size data block is taken. It is first multiplied by the window function or the filter coefficients, i.e., the data is weighted. Then, the block of data is split into P sub-blocks, each of size N. Then the P sub-blocks are added together, point-by-point. Then, the added N-point block is passed through DFT to get the N-point transform. The resulting transform has reduced sidelobes while the main lobe is not broadened. Here, P is referred to as ”taps,” the number of phases used in the polyphase structure. Figure D.1 shows the polyphase filterbank operation with $P = 4$ taps.

Figure D.2 shows the comparison between DFT (FFT), Hann-windowed FFT, and a 4-tap polyphase filterbank response. It shows how effectively the Polyphase filterbank approach reduces spectral leakage while keeping the channel response finer.

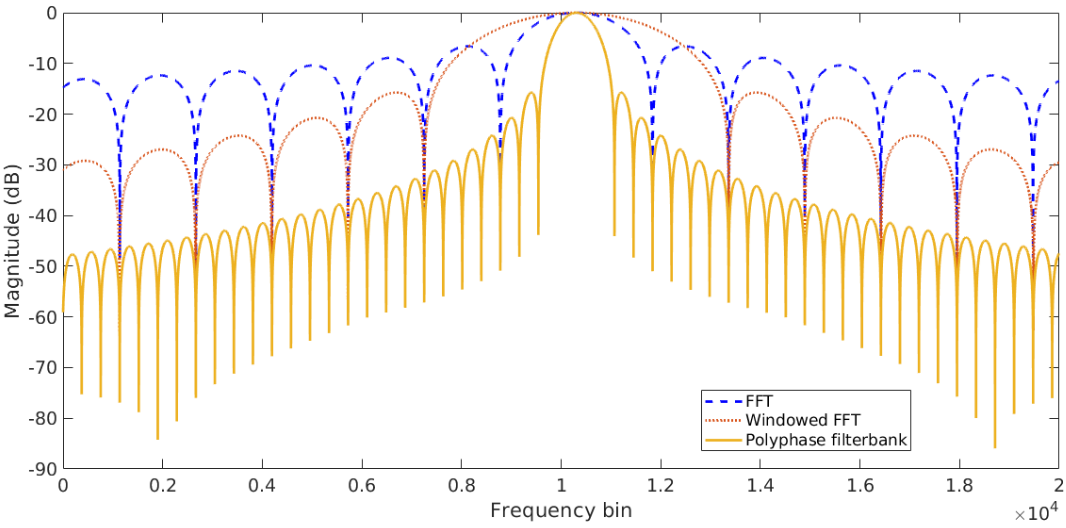

Figure D.2: Comparison of channel response of only FFT, Hann-windowed FFT, and 4-tap Polyphase filterbank

Chapter E

Pulsar detection plots

Here, some pulsar detection plots obtained using GAPS are shown.

Prototype system:

Pulsar B0834+06 and B0950+08 detected using the system described in Chapter 2 are shown in Figures E.1 and E.2. They were detected in the same data of the observation, pointing the array beam to N 6° declination. The observation duration was ~5 hr with 4 ms integration time. The plots are obtained using PRESTO.

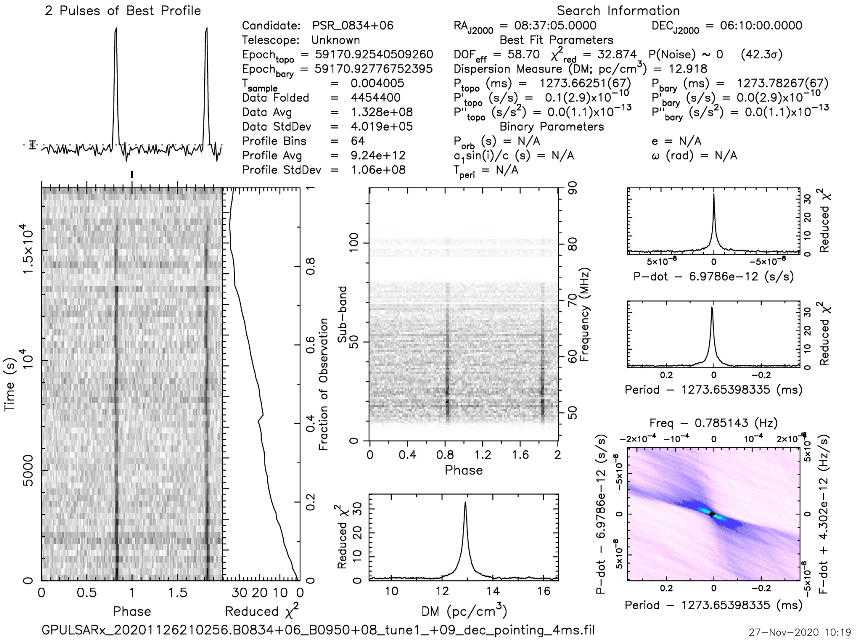

Figure E.1: Pulsar B0834+06 detected using GAPS

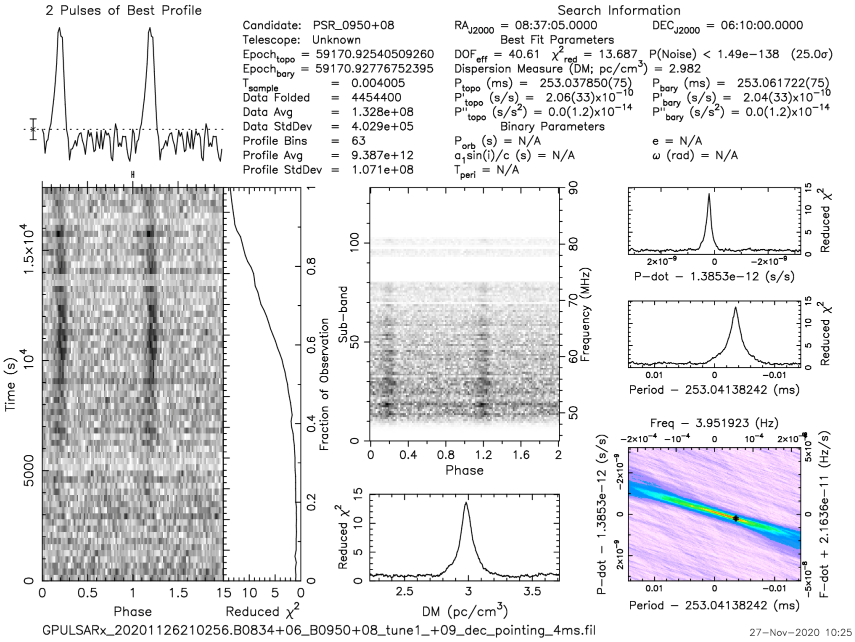

Candidate: PSR_0950+08
Telescope: Unknown
$\mathrm{Epoch_{topo}}$ = 59170.92540509260
$\mathrm{Epoch_{bary}}$ = 59170.92776752395
$\mathrm{T_{sample}}$ = 0.004005
Data Folded = 4454400
Data Avg = 1.328e+08
Data StdDev = 4.029e+05
Profile Bins = 63
Profile Avg = 9.387e+12
Profile StdDev = 1.071e+08

$\mathrm{RA_{J2000}}$ = 08:37:05.0000
$\mathrm{DEC_{J2000}}$ = 06:10:00.0000
$\mathrm{DOF_{eff}}$ = 40.61 χ^2_{red} = 13.687 P(Noise) < 1.49e−138 (25.0σ)
Dispersion Measure (DM; pc/cm^3) = 2.982
$\mathrm{P_{topo}}$ (ms) = 253.037850(75)
$\mathrm{P_{bary}}$ (ms) = 253.061722(75)
$\mathrm{P'_{topo}}$ (s/s) = 2.06(33)x10^{-10}
$\mathrm{P'_{bary}}$ (s/s) = 2.04(33)x10^{-10}
$\mathrm{P''_{topo}}$ (s/s^2) = 0.0(1.2)x10^{-14}
$\mathrm{P''_{bary}}$ (s/s^2) = 0.0(1.2)x10^{-14}
$\mathrm{P_{orb}}$ (s) = N/A
e = N/A
$a_1$sin(i)/c (s) = N/A
ω (rad) = N/A
$\mathrm{T_{peri}}$ = N/A

Figure E.2: Pulsar B0950+08 detected using GAPS

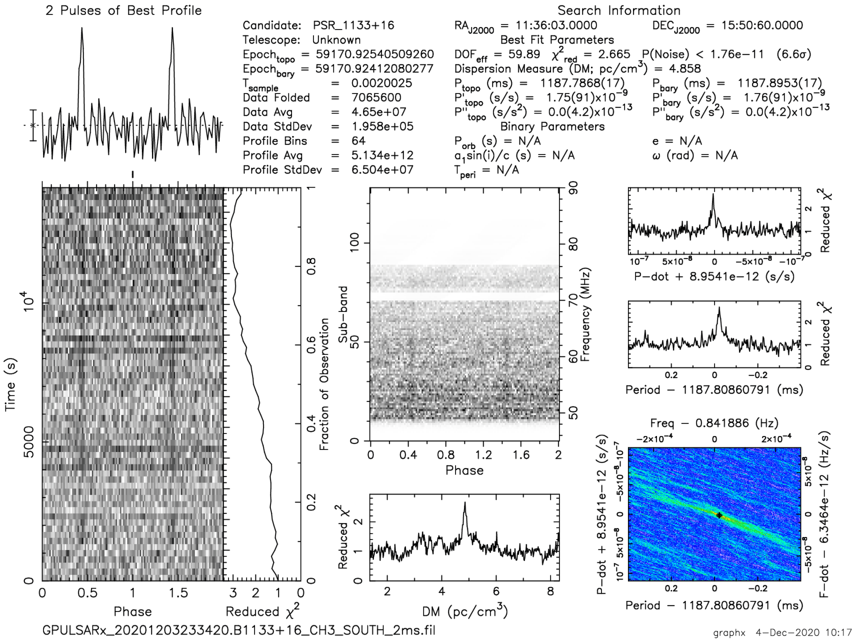

Candidate: PSR_1133+16
Telescope: Unknown
$\mathrm{Epoch_{topo}}$ = 59170.92540509260
$\mathrm{Epoch_{bary}}$ = 59170.92412080277
$\mathrm{T_{sample}}$ = 0.0020025
Data Folded = 7065600
Data Avg = 4.65e+07
Data StdDev = 1.958e+05
Profile Bins = 64
Profile Avg = 5.134e+12
Profile StdDev = 6.504e+07

$\mathrm{RA_{J2000}}$ = 11:36:03.0000
$\mathrm{DEC_{J2000}}$ = 15:50:60.0000
$\mathrm{DOF_{eff}}$ = 59.89 χ^2_{red} = 2.665 P(Noise) < 1.76e−11 (6.6σ)
Dispersion Measure (DM; pc/cm^3) = 4.858
$\mathrm{P_{topo}}$ (ms) = 1187.7868(17)
$\mathrm{P_{bary}}$ (ms) = 1187.8953(17)
$\mathrm{P'_{topo}}$ (s/s) = 1.75(91)x10^{-9}
$\mathrm{P'_{bary}}$ (s/s) = 1.76(91)x10^{-9}
$\mathrm{P''_{topo}}$ (s/s^2) = 0.0(4.2)x10^{-13}
$\mathrm{P''_{bary}}$ (s/s^2) = 0.0(4.2)x10^{-13}
$\mathrm{P_{orb}}$ (s) = N/A
e = N/A
$a_1$sin(i)/c (s) = N/A
ω (rad) = N/A
$\mathrm{T_{peri}}$ = N/A

Figure E.3: Pulsar B1133+16 detected using GAPS

Pulsar B1133+16 detection plot is shown in Figure E.3. It was observed for 4 hr with 2ms integration time,

Raw voltage recording system:

Pulsars detected using the 1-bit raw voltage recording system described in Chapter 4 are shown in the following figures. Pulsars B0834+06 (shown in Figure 4.7), B0950+08, B0919+06, B0943+10, and B1133+16 were detected in the same observation data by forming offline beams in different declinations.

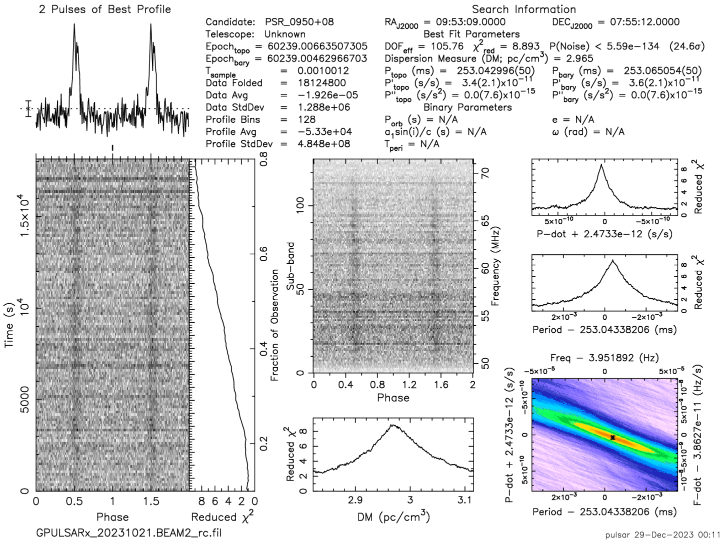

Figure E.4: Pulsar B0950+08 detected using 1-bit raw voltage recording system.

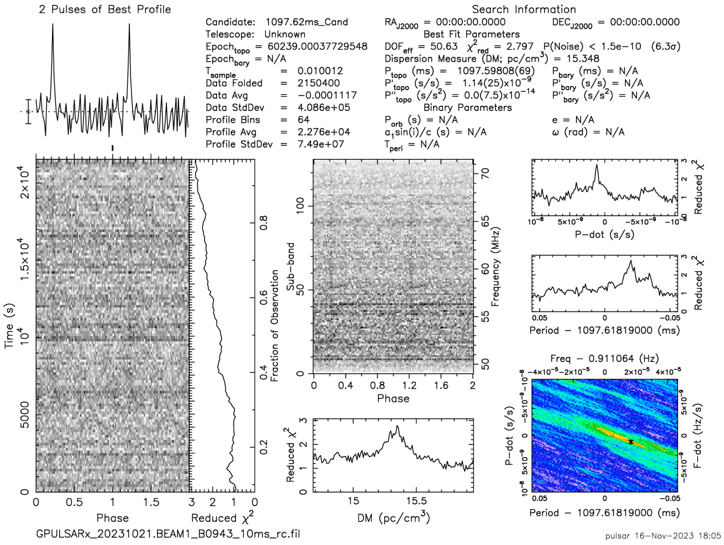

Figure E.5: Pulsar B0943+10 detected using 1-bit raw voltage recording system.

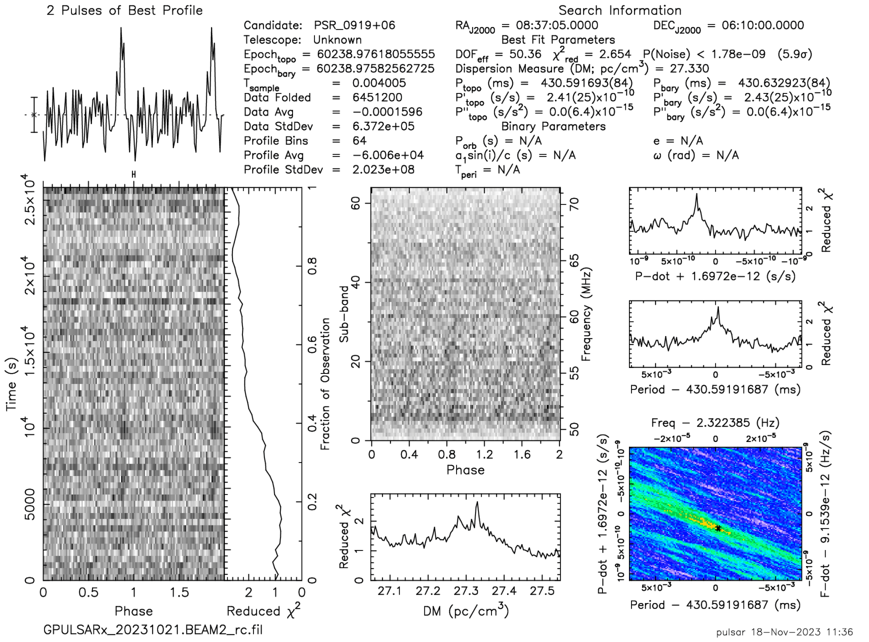

Figure E.6: Pulsar B0919+06 detected using 1-bit raw voltage recording system.

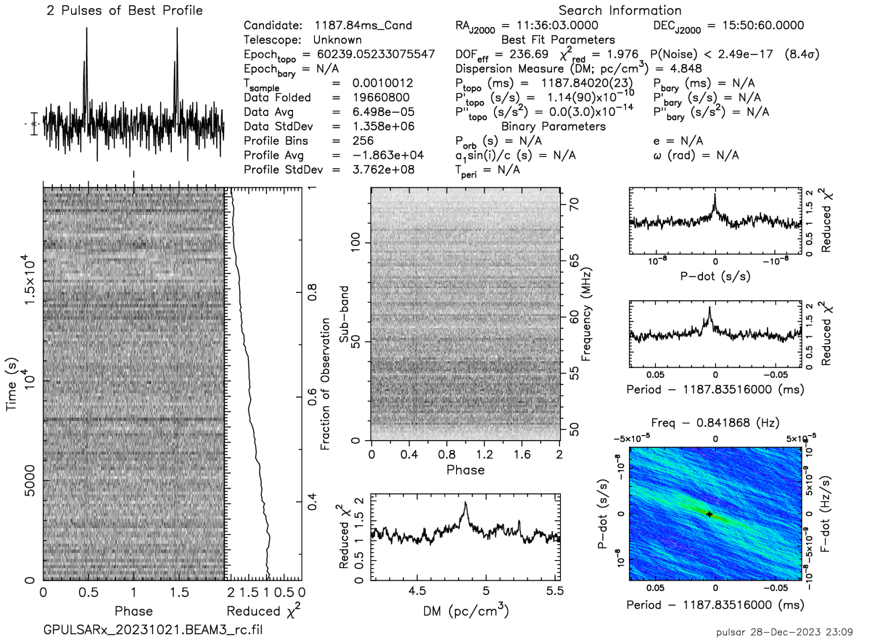

Figure E.7: Pulsar B1133+16 detected using 1-bit raw voltage recording system.

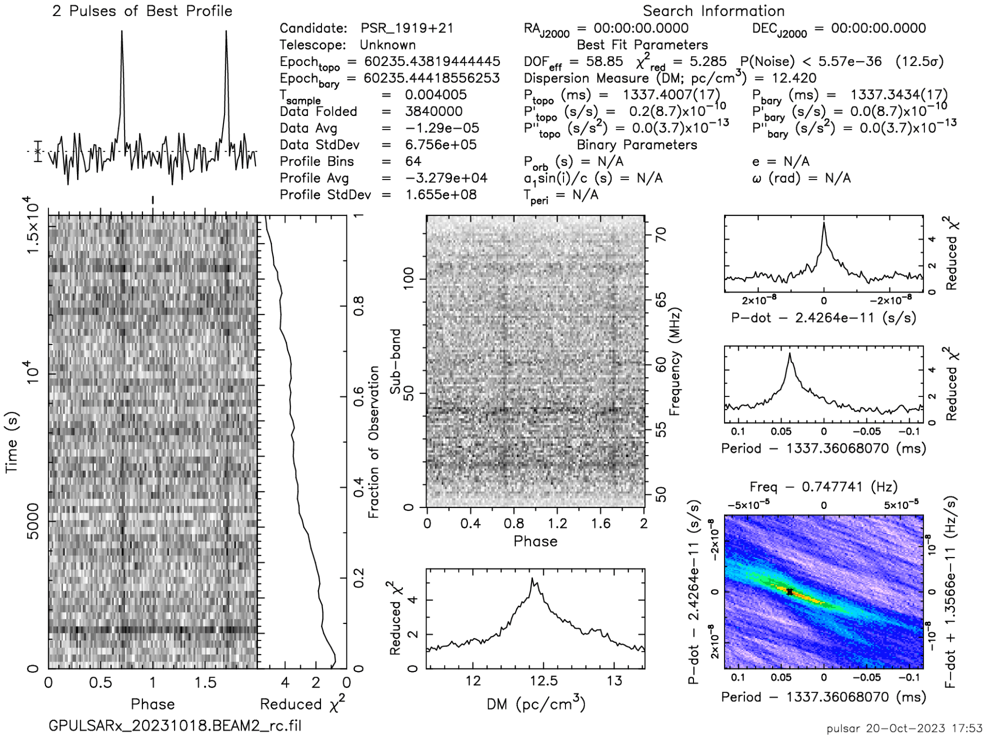

```
Search Information
Candidate:  PSR_1919+21                 RA_J2000 = 00:00:00.0000                DEC_J2000 = 00:00:00.0000
Telescope:  Unknown                               Best Fit Parameters
Epoch_topo = 60235.43819444445          DOF_eff = 58.85  χ2_red = 5.285  P(Noise) < 5.57e-36  (12.5σ)
Epoch_bary = 60235.44418556253          Dispersion Measure (DM; pc/cm3) = 12.420
T_sample        =  0.004005             P_topo (ms) =  1337.4007(17)            P_bary (ms) =  1337.3434(17)
Data Folded     =  3840000              P'_topo (s/s) =  0.2(8.7)x10-10         P'_bary (s/s) = 0.0(8.7)x10-10
Data Avg        =  -1.29e-05            P''_topo (s/s2) = 0.0(3.7)x10-13        P''_bary (s/s2) = 0.0(3.7)x10-13
Data StdDev     =  6.756e+05                      Binary Parameters
Profile Bins    =  64                   P_orb (s) = N/A                         e = N/A
Profile Avg     =  -3.279e+04           a1sin(i)/c (s) = N/A                    ω (rad) = N/A
Profile StdDev  =  1.655e+08            T_peri = N/A
```

Figure E.8: Pulsar B1919+21 detected using 1-bit raw voltage recording system.

Corrections

I thank the examiners for their valuable comments. I have revised the thesis on the suggested lines and addressed the concerns raised by the referees. Following are the list of corrections made in the thesis.
I would like to note that the some page numbers and figure numbers in referee comments are with respect to the old thesis and those in the *Reply* are according to the corrected version of the thesis.

1st examiner's comments and my replies:

List of major corrections to be incorporated

1. General points are: (i) there are several grammatical mistakes (singular and/or plural nouns and verbs are incorrect at several places); (ii) at several place, the sentence construction requires attention; (iii) punctuation marks have not be properly placed at several places; (iv) abbreviation "e.g.," has been used inappropriately at several places (such as "For e..g.," may be avoided); (v) mixing of past and present tenses in the same context has been observed in many places and should be avoided
Reply:"For e.g." is changed to "For example" on page 26, line 7. Sentence formation improved and punctuation marks and grammatical mistakes corrected at places wherever required.

2. Figure 2.7: The peak emission at 18 LST— the source of radiation should be mentioned.
Reply: Source of emission is mentioned as "Galactic plane" in the caption of Figure 2.7 on page 34.

3. Chapter 2: "Due to misalignment of the magnetic and rotation axes of the pulsar, the radio emission comes out in two beams, one from each pole of the magnetosphere." - it is not clear?
Reply: Edited as "The radio emission comes out in two beams, one from each pole of the magnetosphere. The observed emission is coherent, but the mechanism behind the coherence is still being debated. Due to misalignment of the magnetic and rotation axes, these rotating beams of radiation could be noticed whenever they intersect our line of sight to the pulsar, much like a lighthouse on the sea-shore." on page 25.

4. The first part of Chapter 3 and Chapter 4 (Sections 3.2 and 4.2) looks identical, including Figures 3.1 and 4.1. It can be avoided by giving reference of the previously written part.
Reply: As the description and the figure of the antenna array are similar in Sections

3.2 and 4.2, Figure 4.1 and similar parts of the description are removed and reference is given to the previous part on page 52.

5. Section 4.2. The following part is not clear and should rewritten “Note that we used only 8 LPDAs in the GAPS for the present work since our aim is to understand the digital beamformer described in the present work for future use with the Gauribidanur RAdioheliograPH (GRAPH) which has 8 LPDAs per group (Ramesh, 2011; Ramesh et al., 2014), and use GRAPH for dedicated observations of non-solar transients particularly during the local night time.”
Reply: Updated as “We used only eight LPDAs in GAPS for this study because our primary goal was to understand the digital beamformer described here. This understanding will be useful for future applications with the Gauribidanur Radioheliograph (GRAPH), which also employs eight LPDAs per group (Ramesh, 2011; Ramesh et al., 2014). We plan to use GRAPH for dedicated observations of non-solar transients, particularly during local nighttime.” on page 52.

6. Figure 4.6: It would be good mention— how the presented spectrum compare with the regular solar radio spectrometer observation (e.g., Callisto or other instrument).
Reply: For comparison between the spectra from different spectrographs, a table is added on page 56 and Figures 4.4, 4.5 are added on Page 57-58.

7. Figure 4.6: It would be good to discuss the reason for the DM used in this analysis.
Reply: “ The DM used was ≈13.2 pc cm-3” is replaced with “The data was processed using the single pulse search pipeline developed using PRESTO. A range of dispersion measure (DM) values from 0 - 50 pc cm-3 were applied in steps of 0.2 . The maximum SNR was obtained for DM 13.2 pc cm-3.” in Figure 4.3 on page 57.

8. Figure 5.2, page 68: “The size of the circle here is proportional to the peak SNR. In contrast, . .” - the mentioned circle is not clear. Please explain it.
Reply: Modified as ”The sizes of the black circles in the Time- DM plot (the bottom panel) are proportional to the peak SNRs i.e. higher the SNR, bigger the circle. “ on page 657.

9. Section 5.2: Did the observing period of Crab pulsar avoid or exclude the solar approach of Crab pulsar dates?
Reply: The Crab observations were done during the period of May-June 2021. The Crab Pulsar approaches the Sun during mid-June. The idea was to see the Crab Giant pulses away and close to the Sun and compare the difference in the dispersion measure when the signal passes through the solar corona. Unfortunately, no giant pulses were detected in our data. So we couldn’t carry out this study.

Some more minor correction to be incorporated:
1. In Chapter 1, at several places, "pulsar" or "Pulsars" are used in the middle of a sentence. The "pulsar" should not be capitalized unless it is part of a proper noun. The similar type(s) of usage can be checked in the other parts of the text.
Reply: "Pulsars" is changed to "pulsars" wherever necessary.

2. Page 3, Section 1.1.1.2 Integrated pulse profile
Reply: "Integrated pulse" changed to "Integrated pulse profile" on page 3

3. Page 2, line no. 4: brackets for "Pdot" should be removed.
Reply: The brackets for $\dot{P}$ are removed on page 2 line 5

4. Page 7, first line: 'the wave or—" to be removed
Reply: "the wave or" is removed on page 7 line 1.

5. page 16, first bullet- The correct phrase is "larger collecting area"
Reply: "higher collecting area" is changed to "larger collecting area" on page 16

6. page 28, sentence starting with "In order ..." there is a subject-verb agreement error. Correct "signal" to "signals". Attention is also required in the next sentence.
Reply: "Signal" is changed to "signals" and "Output" is changed to "outputs" on page 28 line 10.

7. Page 19, Section 1.4.1.1, first line:" ..which is predominantly high"
Reply: "which is predominantly" corrected to "which is predominantly high" on page 19 line 3.

8. page 21, line no. 4: radius-to-frequency model (RFM)
Reply: "radius-to-frequency (RFM) model" changed to "radius-to-frequency mode(RFM)" on page 21 line 5.

9. page 25, "Due to misalignment of the magnetic and rotation axes of the pulsar, the radio emission comes out in two beams, one from each pole of the magnetosphere." - it is not clear?
Reply: Edited as mentioned above in major comments

10. Page 26, "periodic Fast Radio Bursts (FRBs)" does it mean "repeating FRBs"
Reply: periodic Fast Radio Bursts (FRBs)" changed to "repeating FRBs" on page 26.

11. page 29, "a 8-bit" to "an 8-bit"
Reply: "a 8-bit" changed to "an 8-bit" on page 29

12. page 31, “a 32 bits” ??
Reply: “a 32 bit” changed to “32 bits” on page 31.

13. page 35, fourth line from the bottom, “same time” to “simultaneously”
Reply: “same time” changed to “simultaneously” on page 35.

14. page 37, “Any geometrical delay between the signal incident on the different antennas is digitally compensated . . “
Reply: Modified as “Any geometrical delays between the signals incident on the different antennas are digitally compensated… “ on page 37

15. page 39, “It was initially equipped with an analog beamformer, but it had limitations as mentioned”
Reply: “. But..” changed to “, but” on page 38.

16. page 39, “Both these parameters are significantly large.” (larger is appropriate when stating two quantities).
Reply: “larger” changed to “large” on page 38.

17. Page 40, “. . the signal corresponding to each LPDA is passed . .” (Same mistakes are repeated in Chapter 4, in the first part).
Reply: “are” changed to “is” on page 40.

18. page 42, “Figure 3.3 shows an example of the instantaneous power spectrum in the digitized band of 50 - 70 MHz” (spectra are the plural of spectrum)
Reply: “spectra” changed to “spectrum” on page 42.

19. page 43, ‘this by comparing the sky background temperature in two direction from the low”
Reply: “temperature” changed to “temperatures” on page 43.

20. page 44, “The SNR was =23 in that observations (?).” something is missing here.
Reply: Correct reference added on page 44 line 6.

21. Page 44, “insteps” to “in steps”
Reply: “insteps” changed to “in steps” on page 44.

22. pages 46-47, “The reasonable consistency . . indicates”
Reply: “indicate” changed to “indicates’ on page 46

23. page 47, “heights in the profile—” between them? does it mean heights of different components and the separation

Reply: "heights in the profile" changed to "heights of the components in the profile" on page 46.

24. pages 52, 53, and 54: In this part, Chapter 3 beginning portion (including a figure) is repeated. It may be avoided or rewritten.
Reply: the repetition is removed and reference to the previous chapter added on page 52.

25. Page 56, "Delays are applied to these time series according to the desired declination where the beam needs to be pointed"
Reply: "formed" changed to "pointed" on page 54.

26. page 56, individual spectrum from each antenna is added
Reply: "spectra: changed to "spectrum" on page 55.

27. page 58, A solar event (a similar type III burst event studied by Ramesh and Ebenezer, 2001)
Reply: "A solar event (type III burst, Ramesh and Ebenezer, 2001)" changed to " A solar event (a similar type III burst event studied by Ramesh and Ebenezer, 2001) " on page 56.

28. Page 62, Section 5.1.1 Fast Radio Bursts
Reply: "Fats" corrected to "Fast" on page 63.

29. Chapter 5, in several places, capitalized pronounces are used (e.g., "Pulsars" for "pulsar", "Pulses" for "pulses", etc.); they should be avoided.
Reply: "Pulsars" changed to "pulsars" and "Pulses" changed to "pulses" whenever necessary

30.While referencing a section, it is better to write "Section 1.4.3" (capitalized "Section")
Reply: "section" changed to "Section" whenever referencing to a section

31. page 65, "Crab GPs exhibit peak flux densities ranging from 100 to 1000 Jy at these frequencies."
Reply: "Crab GPs have" changed to "Crab GPs exhibit" on page 65.

32. page 68, "The size of the circle here is proportional to the peak SNR. In contrast, . ." - the mentioned circle is not clear.
Reply: ""The size of the circle here is proportional to the peak SNR" modified as "The sizes of the black circles in the time- DM plot (the bottom panel) are proportional to the peak SNRs i.e. higher the SNR, bigger the circle." on page 68

33. page 69, line no. 1: The data was passed through . . In other places also “put” may be replaced appropriately.
Reply: “put through” changed to “passed through” on page 69 line 2.

34. Figure 5.6: In the caption include unit of DM.
Reply: The unit of DM added as pc/cm^3 on page 72.

2nd examiner’s comments and my replies:

Chapter 2
1. In the Summary of Chapter 2, The candidate may state the strengths and weakness of the LPDA system. How does the phase centre shift in the LPDA as the observing frequency changes?
Reply: The strengths and weaknesses of LPDA are added in the summary on page 36.

The phase centre (PC) of an LPDA shifts with frequency because different dipole elements resonate at different wavelengths. Lower frequencies have PCs farther from the antenna tip. In our case, the PC is 240 cm at 80 MHz and 350 cm at 50 MHz, leading to a maximum of ∼4 ns delay across the observing band. This differential delay can affect the SNR when summing signals across frequency. A correction for this in the voltage domain (similar to coherent de-dispersion, see Section 1.2.2.2) is possible, but it is not currently implemented in our system. Having said so, it must be also noted that the 4 ns delay is smaller than the coherence time of $1/(30MHz) \approx 33.33\,ns$ in the present case.

2. He could also study how the Pulsar profile changes as he moves from 85 to 45 MHz on different pulsars that he has looked at. Scatter broadening of the pulses could be high at low frequencies such as 30-50 MHz even for low DM pulsars (DM ”10) that contributes to low S/N.
Reply: Due to the limited sensitivity, observation over the entire operating frequency band (30 MHz) helps in getting a good signal to noise ratio for the pulsars. However, when the frequency band is divided into smaller bands, the detections in the individual bands are not strong enough to have a solid study of the profile evolution with respect to frequency.

3. What kind of FRBs can be observed. What are the limitations of the array because of small collecting area? What is the S/N of GAP on a strong pulsar like 1919+21 as one goes from high to low frequencies?
Reply: “Due to the limited collecting area leading to low sensitivity, the GAPS can only observe high-fluence (bright) FRBs in the nearby universe. For example, to

detect an FRB of duration 1 ms across 30 MHz bandwidth with SNR of ∼6 with the 16 antenna GAPS at 60 MHz, the flux of the burst has to be ∼5000 Jy. " added in the summary on page 36.
For a particular 6 hr observation of B1919+21 conducted on 31 May 2020 with 16-element GAPS we achieved SNR of ∼62 over the entire frequency band (50-80 MHz). We also processed this data over different frequency bands. For 3 MHz bands centered at 50 MHz, 60 MHz, 70 MHz, and 80 MHz the SNRs were ∼20, 18, 12, and 10 respectively.

Chapter 3.
4. What are the insertion losses of LPF and HPF and do they impact the N/F of the system?
Reply: "The insertion losses of both the high-pass filter (HPF) and low-pass filter (LPF) are ∼0.1 dB each. Since the LPF and HPF are passive components, their contribution to the system's noise figure is equal to their insertion loss, i.e., 0.1 dB each. However, the low-noise amplifier (LNA) in our system has a noise figure of 3 dB, which is significantly larger and dominates the overall noise performance. Thus, while the insertion losses of the filters do have a minor effect on the system noise figure, their contribution is negligible compared to the LNA. The overall system noise figure remains largely dictated by the LNA's characteristics." added on page 40.

5. Sec 3.3 & 3.4: When the input frequency received is from 35 to 85 Mhz, why was it necessary to limit it to only 20 MHz via BP filter from 50 to 70 MHz? Fig 3.4 shows that 50-70 MHz is the range over which the gain is within a small gain range but this fact could be stated in the text as an explanation. If the bandwidth is only 20 MHz, then why is it being sampled at 90 Mhz? This may also be explained. For Fig 3.5 caption, it is preferred that it says 8-element GAPS.
Reply: For the digital beamforming system, we have 8 individual antenna signals that need to be digitized. In the previous prototype system we had used two bandpass filters of 50-80 MHz. We didn't have eight of these filters available, but we did have eight 50-70 MHz Band pass filters available at our observatory which we used for this 8 antenna system. For the consistency with the previous prototype system we used 90 MHz sampling. The required band lies in the second Nyquist zone (45-90 MHz).
"8 element GAPS" is added to the caption of the Figure 3.5 on page 45.

6. Why couldn't the candidate get better counts for Fig 3.4, where he claims power failure. He should repeat this exercise and show that he gets both +26 N and 2 N similar but slightly different. How are the counts related to the spectra (Fig 3.3 shows uniform spectra on sky background for both beam 1 and 2 on some undefined date). Is there any difficulty to show both spectra (on Gal. plane and sky background one after the other) on the same day — so called ON and OFF spectra as well as the

counts thereof?
Reply: Figure 3.3 shows instantaneous power spectra for 4 ms however the Figure 3.4 shows frequency average time series of 1 s integrated signals over 10 hours. The differences in the counts are because two different directions in the sky are probed which have different sky temperatures.

7. The sentence on p 44 needs better clarity. Candidate brings up a previous prototype of GAPS using all 16 LPAs with reduced bandwidth but raises a question mark. This is not clear. Why the previous prototype could not be continued is not explained.
Reply: For the digital beamforming system, each antenna should be individually digitised. We had 2 Quad-ADC cards available (total 8 inputs). So, instead of 16 we used 8 antennas for this setup. Also, as mentioned in Section 4.2 this gives us an opportunity to understand digital beamformers for future work with the Gauribidanur Radio Heliograph (GRAPH) which has 8 antennas per group.

8. Sec 3.5: Summary: On page 49, use a simpler word instead of "commensally' (used more in biology); for example: one can say that "the system could also alternatively detect other bright transient emissions —'.'
Reply: Sentence modified as suggested on page 49 line 11.

9. According to Bondonneau et al., 2020, the flux is 2.2 Jy (ref: Table 1 on page 68) for B0950+08. The pulsar 0834+06 is almost half the flux (1.2 Jy). Yet the Figures 3.8 to 3.10 give S/N ratios that are not aligned with the fluxes. This needs a clarification. It is understood that absolute fluxes are difficult to measure in a 1-bit system even while offering flexibility (p 60).
Reply: This observation was carried out for 4 hours centred at the transit of the Pulsar B0834+06. Pulsar B0950+08 is about 1.5 hr lagging So, B0834+06 was in the beam for the entire duration but B0950+08 was in the beam for only half the duration. Moreover, the beam in declination was pointed to B0834+06 i.e. North 6.17°. B0950+08 is $\sim$2° away from the beam maxima which has resulted in reduced SNR.

Chapter 4:
10.In many places the candidate has stated that the observations are for the frequency range 35 to 85 MHz (Sec. 4.2 for ex.). However, as remarked above, the useful range for GAP appears to be only 50- 70 MHz. That is OK in a prototype instrument but it is important not to overemphasize this aspect in the thesis by verbatim transfer from the paper and repeating what has already been written earlier! Example: Fig 4.1 seems to be the same as Fig. 3.1.
Reply: "35 to 85 MHz" changed to "50 to 80 MHz" on page 52.

11. In Fig. 4.5, the caption does not state how many pulses were averaged in each case (since their fluxes are different). There are no markings on the Y-coordinate, even if it is in arbitrary units. Are the numbers the same for all pulsars; if they are different, that needs to be stated. The candidate may also state within each profile in Fig 4.5, what is the estimated/derived S/N (Table 4.2 is not referred to here although it is referred to as Table 2 on page 59. Correct this to Table 4.2 for consistency).
Reply: "Table 2" corrected as "Table 4.3" on page 60. The number of pulses are available in Table 4.3 and the detection plots for individual pulsars are available in Appendix E. The references are given in Fig. 4.8 caption on page 60. The amplitudes for each profile are different in arbitrary units. This is mentioned in the caption now.

12. On page 59, which GAP is the candidate referring to when he states SNR of 36? Is it the 8 element GAPS or 16 element GAPS? I find this inconsistency throughout the thesis. (half GAPS vs full GAPS). A thesis needs to be precise about such things!
Reply:"GAPS" changed to "8-element GAPS" on page 61 and other places wherever necessary.

13. There is a figure 4. 7 and Table 4.2 on page 61. These are in the wrong place. Transfer them to the pages where they have direct relevance. Fig. 4.6 and 4.7 can be one below the other.
Reply: The figures are moved as suggested. Figure 4.3 and figure 4.4 are together on page 57. Figure 4.5 and figure 4.6 are on PAGE 58. Figure 4.8 is followed by Table 4.3 on page 60 which has the relevant information.

Chapter 5:
14. Sec. 5.1.1: Fats Radio Bursts may be corrected to Fast —.
Reply: "Fats" corrected to "Fast" on page 63.

15. Single pulse search pipeline for transient detection is systematically developed and the reasons for non-detections are outlined. This is a well written chapter.

Chapter 6:
16. Area is $4000^2 50$ MHz frequency — correct typo.
Reply: $4000^2 50$ MHz corrected to "4000 m^2 at 50 MHz" on page 77.

17. As part of the future work, the candidate may suggest increasing the collecting area by firstly using all 16 LPAs and making additions to the backend, and then move on to modifying GRAPH.
Reply: This suggestion has been added in the future work on page 77.